University of Nevada, Reno

Interrogation of Astrophysical Laboratory Photoionized Plasmas with Experiments at the 1MA Zebra and 26MA Z Pulsed-Power Drivers

A dissertation submitted in partial fulfillment
of the requirements for the degree of
Doctor of Philosophy in Physics

by
Kyle J. SWANSON

Dr. Vladimir V. Ivanov/Dissertation Advisor
Dr. Roberto C. Mancini/Dissertation Co-advisor

May, 2022

THE GRADUATE SCHOOL

We recommend that the dissertation
prepared under our supervision by

Kyle James Swanson

entitled

Interrogation of Astrophysical Laboratory Photoionized Plasmas with Experiments at the 1MA Zebra and 26MA Z Pulsed-Power Drivers

be accepted in partial fulfillment of the
requirements for the degree of

DOCTOR OF PHILOSOPHY

Vladimir Ivanov, Ph.D.
Advisor
Roberto Mancini, Ph.D.
Co-advisor
Melodi Rodrigue, Ph.D.
Committee Member
Pat Arnott, Ph.D.
Committee Member
David Bennum, Ph.D.
Committee Member
Swatee Naik, Ph.D.
Graduate School Representative

David W. Zeh, Ph.D., Dean
Graduate School

May 2022

UNIVERSITY OF NEVADA, RENO

Abstract

College of Science

Physics Department

Doctor of Philosophy in Physics

Interrogation of Astrophysical Laboratory Photoionized Plasmas with Experiments at the 1MA Zebra and 26MA Z Pulsed-Power Drivers

by Kyle J. SWANSON

Due to the lack of spaceships with intergalactic capability, now and in the foreseeable future, we must find alternate methods to bring the universe to us. By studying laboratory photoionized plasmas we can further our understanding of highly energetic astrophysical environments, such as the accretion disks around black holes and neutron stars, giving rise to, active-galactic-nuclei and x-ray binary systems. These cosmic engines produce high-intensity broadband x-ray and UV radiation flux, which heats and ionizes the surrounding gas into a photoionized plasma. Laboratory data is a crucial aid in our interpretation of astrophysical observations and ability to test and validate astrophysical codes. We have used the 1MA Zebra and 26MA Z-machine pulsed-power drivers to experimentally study astrophysically relevant photoionized plasmas. On Zebra, the supersonic gas jet platform provides the first method for university-scale drivers to study such plasmas. The gas jet platform leverages the diverse diagnostic capability and robust shot rate of Zebra, providing perspectives inaccessible to that of large-scale drivers. This work has motivated the first broadband spectral characterization of Zebra's radiation drive. Alternatively, on the Z-machine, the photoionized gas cell platform has enabled studies at the highest level of x-ray flux terrestrially possible. For the first time, we have integrated photon Doppler velocimetry into the gas cell, which has been used to answer the critical question of uniformity within the gas cell by observing spatially resolved electron number density time histories. In the broader context of Z diagnostics, this work has also demonstrated the feasibility of high-precision low-noise measurements in close proximity to the overwhelming x-ray flux of the Z-machine. These two laboratory photoionized plasma platforms each provide unique capabilities: Zebra experiments emphasize the role of L-shell atomic physics on heating and ionization of neon plasmas, while Z extends it to plasmas populated with K-shell ions. Hence, both experiments provide complementary astrophysically relevant data of photoionized plasmas.

To my family

Acknowledgements

To Dr. Vladimir Ivanov, I am beyond grateful for the time I had working alongside you in the lab. Of all the techniques that I have learned from you, it was your rigorous and methodical approach of calmly working through challenges that has had the greatest impact. Not once did I notice you allow a frustrating moment to change your demeanor, a skill that benefits all other skills.

To Dr. Roberto Mancini, the other half that formed the Venn-diagram that I found myself in. Thank you for the opportunities and for introducing me to Vladimir. As well, I am grateful for the discussions, I have benefited greatly from these iterative focused pursuits of objectivity.

To Dr. Melodi Rodrigue, you have been my advisor since the beginning. To Dr. David Bennum, how does one begin thanking their very first physics professor, with a fist?... For some maybe, for myself however, I will begin thanking you for not scaring me away. I had not taken a single class in physics until walking into your lecture. To Dr. Pat Arnott, you were the perfect advisor for me in a time I was unsure of myself or my place in physics. Your desire for anything and everything scientifically interesting was nourishing. Thank you for giving me the opportunity to pack the physics department full of snow. To Dr. Swatee Naik, who must have the patience of saint to guide me through the introductory realms of abstract mathematics. While it was brief, my time learning from you not only showed me where the rigor of physics comes from, you as well demonstrated a quality of excellence that is only possible through disciplined practice.

To Dan Mayes, a friend and advisor all rolled into one. Our time working on Zebra and Z together was phenomenal, only second to the epic amount of laughter we seem to continuously generate. I am not sure I could have been any luckier to have someone to adventure with and to follow in their footsteps.

I would like to express thank yous to Nick Wong and Noah Huerta, working with you two alongside Vladimir was a pleasure. As well, I appreciative for the warm and encompassing friendship of the past and current student in Roberto's group, your friendship made it feel as if I was in a single large group. I want to extend thanks to Aidan Klemmer, your help with PDV was essential as well as your company, which made burning the candle at both ends much easier and enjoyable.

I am as well grateful for all of those who made their time available in one way or another to facilitate amazing scientific discussions both here at UNR and at Sandia. Specifically, to the ZAPP group, everyone has been of the highest caliber in terms of the pursuit of science as well as friendship. Our frequent discussions were superb in sharpening my understanding as well as my communication. As well, the discussions with Dan Dolan, Andy Porwitzky, and Kate Bell, were of great importance and on top of that very welcoming.

My sincerest gratitude to the ones that make everything possible behind the scenes. Starting with the Zebra crew, Alexey, Oleg, Wade, and Carl you have been the ones that save day and continue to do so, thank you! To the Z crew thanks for welcoming me with open arms. An important thank you goes to Pat Lake for allowing me to commandeer lab space from time to time. To Chris De La Cruz, without your energy and desire to be awesome, I am not sure I would have been as successful.

To my friends, past and present, your encouragement has always been clear and abundant. I promise I will do my best to be there for all of you in the same you were for me. Art Johnson, how the stars aligned to produce such a supportive and wonderful friendship I haven't the foggiest, but your interest and support in my pursuit of science has been phenomenal. Kelsey the superhero, words are not enough

To my family, Kirk, Kati, and Karmen, without your everlasting support I would not have been able to pursue a life filled with studying the wonderous and fantastical nature of the universe.

This work was sponsored in part by DOE NNSA Grant DE-NA0003875, the Wootton Center for Astrophysical Plasma Properties under U.S. Department of Energy cooperative agreement number DE-NA0003843, and the Z Facility Fundamental Science Program of Sandia National Laboratories.

Contents

List of Tables

List of Figures

"the greatest danger to man in space was man himself."

Robert A. Heinlein, Stranger in a Strange Land

"Life can only be understood backwards, but it must be lived forwards."

Søren Kierkegaard

"Your most important tools are your hands."

V. V. Ivanov

"BnB, Brief 'N' Brilliant"

R. C. Mancini

Chapter 1

Introduction

1.1 Act 1: Cosmic engines

Photoionized plasmas are the most abundant form of matter in the universe. They form in the surrounding environments of high-energy astrophysical phenomena such as: active-galactic-nuclei (AGN),[52, 36] X-ray binary systems,[51] planetary nebulae[35], and more generally accretion powered objects. An artist's representation of an AGN is shown in Fig. 1.1.

X-ray binary systems are prime example, in which a star and black hole or other massive object, orbit each other. As they orbit, the massive gravitational object accretes matter from the surface of the star, the matter orbits the object forming a disk and eventually falling into the object. The disk, known as an accretion disk produces high-intensity broadband UV and x-ray flux. This radiation ionizes the surrounding gases and other matter producing a photoionized plasma.

Observations of these cosmic turbines are primarily done via X-ray absorption spectroscopy. By observing the radiation, we can determine properties about the astrophysical phenomena and the surrounding environment. There is a copious amount of information accessible through x-ray emission and absorption spectroscopic measurements. Spectral analysis can reveal the underlying atomic physics that is taking place,

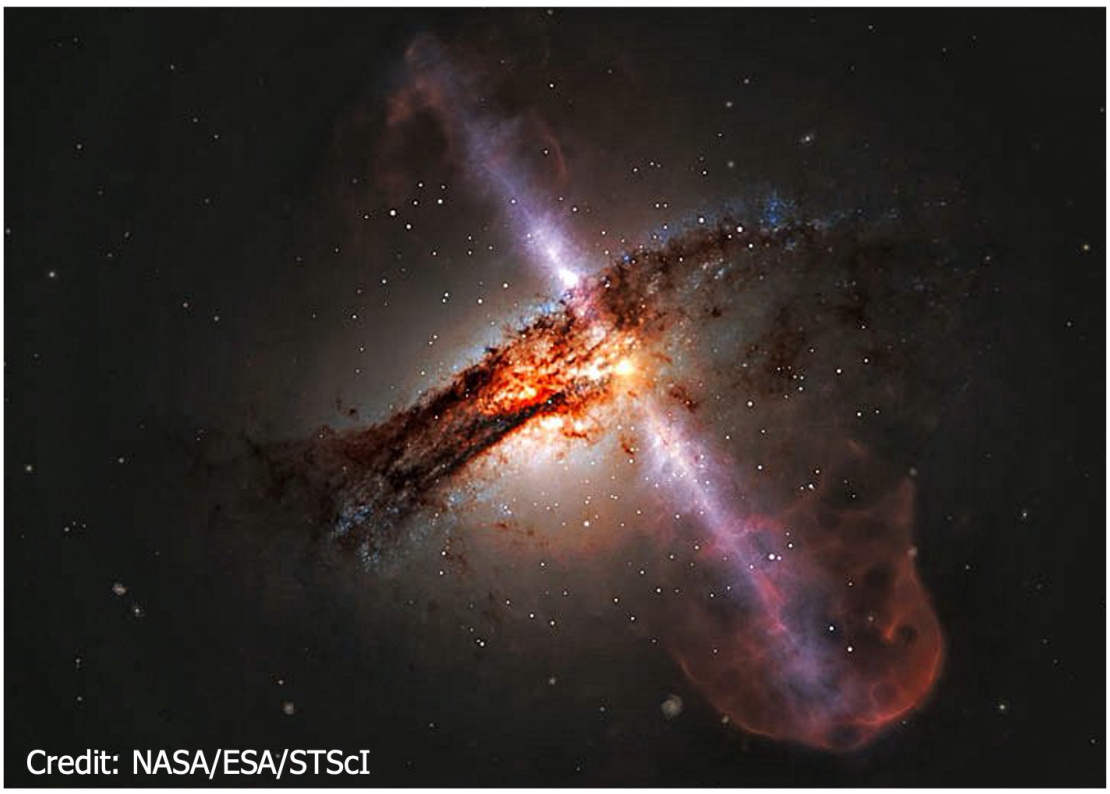

FIGURE 1.1: Artist representation of an active-galactic-nuclei. Credit: NASA

such as and not limited to: the relative ion balance, average charge state, plasma density and temperature. Yet, the possible amount of information does not just end there. Analysis of the thermal continuum from accretion disks of black holes can potentially reveal black hole spin, Lense-Thirring precession, and other aspects of General Relativity. [51]

Accretion disk winds have been observed via photoionization absorption x-ray signatures in the spectra of accretion disks, detailed by Miller et al. [51] The observation taken by Miller et al., show a steady state photoionized equilibrium with absorption features that are characterizable. The analysis performed can infer things such as origin of the disk wind, direction, impact on other processes, etc.

Another example of what can be learned from X-ray spectra of accretion powered objects like active-galactic-nuclei (AGN), is the relative size of the black hole corona with respect

to the accretion disk. By analyzing the coronal spectra with respect to the reprocessed accretion disk spectra, reverberation times of coronal flashes echoing off of the accretion disk allow backward calculation of the corona size. [15]

1.2 Act 2: Are we there yet?

The distances to these objects is astronomical... cough cough so far... there are no practical means of travel in the foreseeable future that will allow close up observation and analysis. Which until that time comes, leaves us with our main method of remote observation, X-ray spectroscopy. These high energy objects reveal their secrets in the UV and X-ray radiation bands, between a fraction of a keV to several keV. By using high precision spectrometers we are able to decode the information of the emitted object. Unfortunately for this range of the spectrum, the instruments must be orbiting in space based observatories to get above the atmosphere which blocks the signal. The X-ray Multi-Mirror Mission (XMN-Newton) and the Chandra X-ray observatory are two examples of high quality instruments used to investigate these objects.

The XMM-Newton has been surveying the x-rays from the cosmos for 22 years. Originally launched December 10th, 1999, the XMM-Newton has studied over half a million x-ray sources. [72] An example of XMM-Newton observations come from Pinto et al. [55] These observations were centered around ultraluminous x-ray sources. The accretion disks in these investigations exceed the Eddington limit, where radiation pressure can expand the disk and drive winds to significant fractions of the speed of light.

The Chandra X-ray observatory was launched July 23rd, 1999. At the time of launch, Chandra was 100 time more sensitive than previous x-ray telescopes. The work conducted by Miller et al. [51] mentioned above, utilized the Chandra X-ray observatory in April 2005 to observe the x-ray binary system GRO J1655-40 using the High Energy Transmission Grating Spectrometer. The cumulative observation time was 12.4 hours, the result is shown in Fig. 1.2. There are two things to quickly notice about this spectrum.

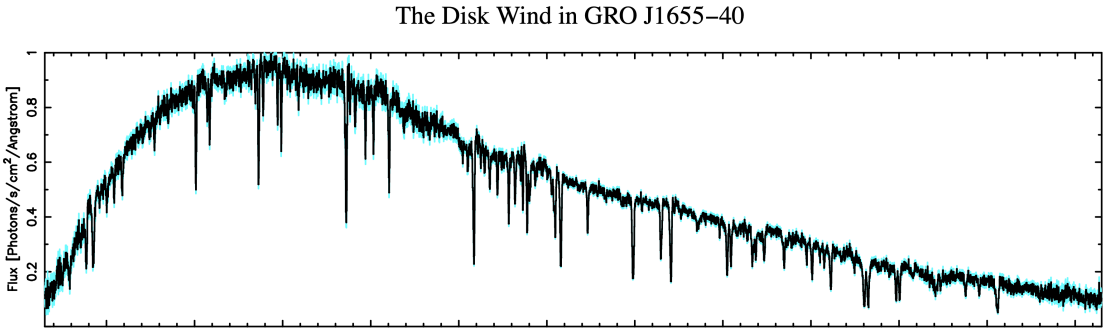

FIGURE 1.2: 1.3-13.3Åspectrum of GRO J1655-40. [51]

The spectrum has a recognizable characteristic shape, that of a black body radiator, a Planckian distribution. Second, is the deep absorption features seen in the spectrum. These features having been recorded over ∼12 hours, which tells us that the absorbing medium, a photoionized plasma, is in steady state. That is to say that the plasma is in a photoionization equilibrium. These are some of the clues that tell us about the environment and object.

Such observations are inherently difficult and have some unavoidable uncertainties. The main and obvious hurdle is to make the observation in space in the first place. It's easy to take the satellite observatory for granted once its in place, but one wrong move and there is no recovering from a launch malfunction. (At the time of this writing, the James Webb has just recently parked into its Lagrangian point and unfurled its radiation shield.) Another factor that makes these observations challenging is whether the signal being observed is transient, which can pose a significant threat to the interpretability of the measurement.

1.3 Act 3: It gets better, wait I mean worse!

If you thought the measurement itself was difficult, take a seat, the interpretation can be just as rough. Astrophysical measurements such as these are challenging to acquire as well as interpret[45, 51]. The light required for such spectral observations travels over vast distances. The journey made by the light emitted from the system under

investigation to the detector can be littered with countless obstacles that may absorb and partially block the path. Further, some obstacles maybe time dependent like a passing cloud of dust... or a star cruiser. The point being... until we have star cruisers of our own, we can only theorize and do our best to account for what may be along the line of sight. This is where interpretation of our measurement and of our analysis start to become crucial. In a perfect world, with some limitations, one may propose to perform systematic observations that iterate over the parameter space in question. This however is not very feasible and very much improbable. Even if such a survey was possible time dependent effects of the system in question and or time dependent phenomena along the line of sight would render such an effort with a high degree of uncertainty.

Let's go one step further... say that we could perform exhaustive astronomical surveys with low uncertainty... The atomic processes that occur within photoionized plasmas driven by these extreme environments are complicated and require much more than pencil and paper to process and analyze. Scientists utilize computer codes and simulations to aid in their interpretation of the data recorded. Atomic kinetics codes such as PrismSPECT[41], XSTAR[16], and CLOUDY[3] are used to model the atomic systems believed to be responsible for the observations made. Yet, atomic kinetic codes have been developed mainly on a best theory effort. For this reason, astrophysical codes employing atomic kinetics models must be bench-marked and validated against known observations. One may wonder, "Isn't this a bit cyclic? If the purpose of the codes is to help our understanding of observations... then how can we use observations to benchmark and validate the codes?" To answer this question we introduce a third avenue of discovery: experiment, specifically laboratory astrophysics.

1.4 Act 4: Laboratory Astrophysics To The Rescue

An alternative method to space travel and remote observation, is to bring the stars to us. Laboratory astrophysics is a realm that allows experimenters here on Earth to investigate

astrophysical phenomena, helping to bridge connections between astrophysical observations and the supporting theory/modeling. By recreating astrophysical phenomena in the laboratory, we can perform systematic experiments that we use to aid in the interpretation of observation and in the validation and testing of codes and models. One of the most important benefits of laboratory astrophysics, and experiments in general, is the ability to reproduce experimental results on demand, unlike astrophysical observations that require luck and/or technology to advance to get achieve a better look. Similarly, another benefit provided by laboratory astrophysics is the ability to be systematically rigorous. Exploring a parameter space in a systematic fashion provides a method to tease out phenomenological nuances that otherwise may have been misunderstood or overlooked all together.

A key aspect of laboratory data is that the experimental recipe is known. This is important because initial parameters like neutral atomic density, volume, radiation drive, etc. are paramount to the interpretation of emergent phenomena in astrophysical observations and comparison to simulations.

Diagnostics are a key component of the experimental recipes, they define the observed parameter space. Typically, there are more than one that allow partial understanding of the processes under investigation. For high-energy-density laboratory astrophysics, spectroscopy and laser diagnostics are relied on heavily. For experiments that have independent diagnostics, checking reproducibility of results is highly valuable (providing peace of mind, allowing one to sleep at night I suppose the inverses is true as well).

Due to these benefits afforded by experiment, the average quality of laboratory produced data will be greater than that of astrophysical observations. And if those benefits weren't enough, laboratory equipment advances as technology advances, unlike the technology we launch into space. Which is why laboratory data can be so helpful in the interpretation of astrophysical observations. While, it is the ability to systematically probe parameters spaces that makes laboratory data an important tool for the testing and validation of

codes and simulations.

The role that laboratory astrophysics plays is paramount and emboldened by discrepancies found between observation and theory. A clear example is the significant overestimation of photoionized plasma electron temperature T_e by astrophysical models such as CLOUDY and XSTAR. [46] The combined effort of performing photoionized plasma experiments on the Z-machine and careful modeling showed that photoexcitation has a great effect on excited-state populations, line emissivity, and radiation cooling; Highlighting the importance x-ray heating and radiation cooling in accurately describing the energy balance of the photoionized plasma in question.

Measurements of iron opacity at stellar conditions is another point of discrepancy that is currently being investigated. [1] Due to advancements in photosphere spectral analysis of the sun, a 30-50 per cent reduction of the inferred carbon, nitrogen, and oxygen solar abundances has been observed. This led to a disagreement between helioseismic observations to calculate stellar interior structure and standard solar models using the reduced abundances. If the stellar plasma opacity was greater than predicted this would account for the reduced elemental abundances. This discrepancy motivated experiments on the Z-machine to measure iron opacity at stellar interior conditions. Iron was chosen to be investigated first as it accounts for a quarter of the total stellar opacity. The results of the experiments showed the measured wavelength-dependent opacity of iron is 30-400 percent higher than predicted; which accounts for about half the required change in mean opacity. The opacity experiments have caused a paradigm shift in thinking and are continuing to produce new results for other elements.

A similar experiment to test the validity of the results found on Z is underway at the National Ignition Facility. Discrepancies such as these and the experiments detailed above provide illuminating results to questions that have been difficult to answer and may not be answerable without laboratory experiments exploring photoionized plasma studies and, more generally, astrophysics as a whole.

1.5 Act 5: The Adventure Plan

We now have the base understanding to conceptualize the adventure that is about to take place. The adventure being: To diagnose laboratory produced photoionized plasmas, by exposing volumes of gas to intense ionizing radiation which will heat and ionize the gas. This journey will have us traverse across great parameters spaces such as current, pressure, atomic density, electron density x-ray flux, temperature etc.

One part of this adventure, will be on safari, utilizing Zebra a 1 MA pulsed-power driver at the Zebra Pulsed-Power Laboratory at the University of Nevada, Reno. The photoionized supersonic gas jet platform was developed for Zebra to study photoionized plasmas. The conception of this platform was in response to the photoionized laboratory data paucity problem. [2] Cylindrical supersonic gas jets are used as an interaction medium for photoionization studies.

The second part of this adventure takes place on the Z-machine, the most powerful x-ray source in the world. The Z-facility, is located at Sandia National Laboratories in Albuquerque, NM, on the Kirkland Air Force base. Here the adventure picks up the gas cell adventure from the previous Z explorer, Dan Mayes. [50] The photoionized gas cell platform on Z, exposes a 2x2x1 cm volume of gas to the overwhelming x-ray flux from implosion of the z-pinch dynamic hohlraum.

While these two experiments are performed under different circumstances, we will see that they are complementary to each other, motivated by the same purpose: Interrogating laboratory produced astrophysically relevant photoionized plasmas driven by intense broadband radiation, by the systematic exploration of the accessible parameters spaces made possible by Zebra and Z. With the ultimate set of goals, shared between the two platforms, being: Improve our understanding of astrophysics, plasmas physics, atomic physics, and basic physics.

1.6 Summary of chapters

The composition of the following work is as follows.

Chapter 2 provides an overview of photoionized plasmas. First, some of the fundamentals of atomic physics relevant to photoionized plasmas are reviewed. Following up with a discussion on what constitutes a photoionized plasma and what does not. From which point metrics for the characterization of photoionzed plasmas will be presented. The chapter will end by reviewing the different methods we have to observe these plasmas and what tools we have to know that we are indeed working with photoionized plasmas.

Chapter 3 revolves around the radiation drives that support photoionized plasmas in these high-energy astrophysical environments and the characteristics of these cosmic engines. From this understanding we move towards what methods we have here on Earth to create radiation drives that are comparable to astrophysical ones. This leads to the introduction of z-pinches and the pulsed-power machines that drive them.

Chapter 4 details the experimental effort to characterize the radiation drive of the 1MA Zebra pulsed-power driver. The chapter starts with specifying the requirements of what measurements are necessary to accurately characterize the spectral distribution of Zebra's radiation drive. With the measurement goals in mind, the x-ray diffraction grating spectrograph is introduced as the instrument of choice, followed by the experimental setup and the characterization plan.

Chapter 5 introduces the photoionized supersonic gas jet experiments. The first important detail discussed is the importance of using gas jets as a photoionization medium, specifically for university scale pulsed-power machines. After which the plethora of diagnostics used to interrogate the photoionized plasmas, which include a variety of laser and x-ray diagnostics. After introducing the diagnostics, specifically the interferometry diagnostics, the Interferometry and Analysis suite is introduced and discussed.

The second half of this chapter focuses on the nozzle designs used, and the gas jets produced from them. A detailed account of the characterization of the neutral gas jets are presented.

Chapter 6 reviews the photoionized gas cell experiments on the Z-machine. The chapter begins with review of the previous generations of the gas cell experiments and how they have evolved over time. Next the diagnostics used for these experiments are presented. The last part of this chapter documents the addition of a new chordal laser interferometry diagnostic that has been integrated into the gas cell platform.

Chapter 7 shows the first set of experimental results for the spectral characterization of Zebra's radiation drive. The initial effort covers the measurements of aluminum Z-pinch spectra in the range of 40-700Å. Initial efforts to identify emission features in the aluminum z-pinch plasma are shown. The corrections necessary to analyze the spectral distribution are presented. The chapter ends with the first temperature estimate calculation by way of Planckian distribution fit.

Chapter 8 presents the inaugural experimental results of the photoionized supersonic gas jet experiments. The chapter starts with showing laser diagnostics methods to initially verify the successful photoionization of gas jets using Zebra. This is followed by an in depth look at electron density maps extracted from laser interferometry measurements. Next, x-ray transmission spectra is presented from a variety of the experimental campaigns conducted thus far. The chapter ends with a comparison of results between laser interferometry and x-ray spectroscopy.

Chapter 9 covers the experimental results from the photoionized gas cell experiments on the Z-machine. Presented first are the initial measurements recorded using photon Doppler velocimetry. To develop confidence in the newly integrated diagnostic, radiation noise characterization in the fiber optic system are shown and results from a null shot with no gas fill are discussed. After confidence has been established in the PDV diagnostic, results are shown for three different shots, two with 15 Torr of neon gas fill

and one with a 50:50 mixture of neon and argon with 60 Torr of gas fill. For the 15 Torr gas fill shots, a comparison between the electron density time histories recorded are made with simulation. The second section in the chapter presents transmission spectra from several shots and presents initial results.

Chapter 10 concludes the dissertation. First, the results of the first ever large spectrum survey of Zebra's radiation drive are reviewed. This is followed by reviewing the experimental achievements of the supersonic photoionized gas jet platform on Zebra. Second, the advancements of the gas cell platform are discussed. The importance of photon Doppler velocimetry are discussed both for the platform and the Z-facility. As well, the importance the x-ray absorption spectroscopy is discussed and the hurtles it faces.

Chapter 2

Photoionized Plasmas

Photoionized plasmas are the most abundant form of matter in the universe, found in highly-energetic astrophysical phenomena such as active-galactic-nuclei and more generally accretion powered objects. These cosmic engines, the most powerful in the universe, produce high-intensity broadband ultraviolet (UV) and x-ray flux, which floods the surrounding volume in ionizing radiation. The surrounding gas is excited and ionized by these celestial radiation drives, producing photoionized plasmas. This highly charged soup of positive nuclei and electrons are intimately related to the astrophysical phenomena that support them, so much so that with the absorption spectra observed from the photoionized plasmas that are encoded with a wealth of information about the driving object. By studying photoionized plasmas we better understand the cosmic wonders of the universe.

The goal of this chapter for us is to establish a fundamental understanding of the underlying atomic framework that provides the structure for complex highly charged ion soups, known as plasmas. With this foundation, it will be clear the central role light plays, the ways it may and may not interact with a plasma. This chapter is laid out in the following way. Section 2.1 we will start with fundamentals of atomic physics, covering such things as ionization and recombination. Section 2.2.2.2 will build on these concepts, from which we will construct working descriptions of more complex systems

aka plasmas. Using the atomic groundwork laid down in the previous section we will introduce fundamentals of plasmas, with emphasis on photoionized plasmas, covering the following: Photoionization equilibrium, ionization parameter, average charge state, etc. Section 2.3 briefly discusses how we validate what we think is occurring. Most importantly validation comes from our observations, a topic that will be revisited as we are introduced to new forms of data as we explore further through these chapters. The second general method of validation comes from our ability to predict observations via computation techniques. Astrophysical codes and computer models are used to aid in our understanding of the atomic physics, plasma physics, and astrophysics. Chapter 2 will conclude with a summary reviewing the crucial concepts necessary to get the most out of this dissertation.

2.1 Atomic physics

Before we dig too deep lets start with the some basics. What is a plasma? Plasma, sometimes colloquially referred to as the fourth state of matter, is nothing more than partially to fully ionized matter, a soupy collection of positive nuclei and negative electrons. Plasmas form when the electrons in matter become excited and ionized. In general there are two types of plasmas: photoionized and collisionally-ionized.

All the fundamental details about a plasma lie in the atomic processes that take place. Careful and methodical observations of plasmas one can reveal properties of a plasma from the atomic physics such as temperature, density, factional ion population, charge state, chemical composition, etc. The analysis of such observations require to computational tools that allow systematic iterative calculations. First, we will go in detail into the main atomic processes that we will encounter.

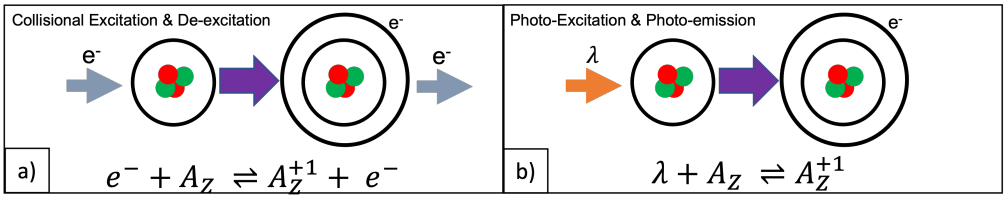

FIGURE 2.1: a) Collisional excitation and de-excitation. b) Photoexcitation and photo-emission.

2.1.1 Excitation/De-excitation

Probably the most well known atomic processes are the excitation and de-excitation of electrons in atoms. The excitation of an electron refers to the quantum mechanical phenomena in which an electron receives an amount of energy that allows it to be promoted to a higher energy level aka an excited state or level. De-excitation refers to the energy loss mechanism of an electron, whereby loosing energy it is demoted to a lower state or orbital. Excitation and de-excitation can happen in one of two ways. One method is by way of colliding electrons, free electrons collide with a bound electron of an atom. This collision can either impart energy to excite the bound electron or absorb enough energy from the bound electron that the electron drops down to a lower energy state. The second method in which electrons can be excited and vice versa is via photon interaction. A photon of a given wavelength, λ, with energy $h\nu$ can be excited to a higher energy level with a difference equal to the energy of the photon. In a reverse process, excited electrons can emit photons with energy equal to the difference between their initial excited state and final lower state, see Fig. 2.1.

2.1.2 Ionization & Recombination

Second in notoriety to excitation and de-excitation comes ionization and the reverse process recombination. Here, an electron is ionized when excited to the point of being liberated from the positive pull of the nucleus. The methods of ionization are very similar to the two methods of excitation. Either, a colliding electron or a photon must have energy equal to or greater than the ionization potential for the bound election.

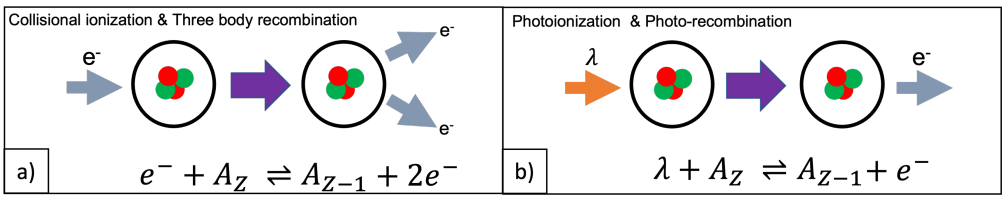

FIGURE 2.2: a) Collisional ionization and three-body recombination. b) Photoionization and photo-recombination.

The reverse process of ionization is recombination, when a cation captures an electron. Similar to the excitation processes, collisional and photoionization have their respective reverse processes. The reverse of collisional ionization is Three-body recombination. The mechanism requires two colliding electrons inbound on the same cation. Instead of a photon being emitted by the captured electron, the second inbound electron receives the kick in energy from the captured electrons initial excited state and its new final lower energy state, see Fig. 2.2.a. The reverse of photoionization is photo-recombination. In photo-recombination, when a free electron passes close to a cation with an electron affinity great enough to capture the passing electron. When the electron re-combines it emits a photon equal in energy to the difference in the electrons energy and the electronic state is has assumed, see Fig. 2.2.b.

2.1.3 Autoionization and Spontaneous radiative emission

Now, with atomic processes such spontaneous radiative emission and autoionization, we find ourselves on paths a little less worn. These two processes involve the spontaneous/random processes that are very much opposite in result. The first, autoionization occurs when an atomic system has an electron excited to a state above the first ionization limit, which happens to be the ground state of the next ion. In this configuration the electron can spontaneously eject, see Fig. 2.3.a. The second process, spontaneous radiative emission, is the process in which an excited atom seemingly at random emits a photon as an excited bound electron drops to a lower energy level, see Fig. 2.3.b.

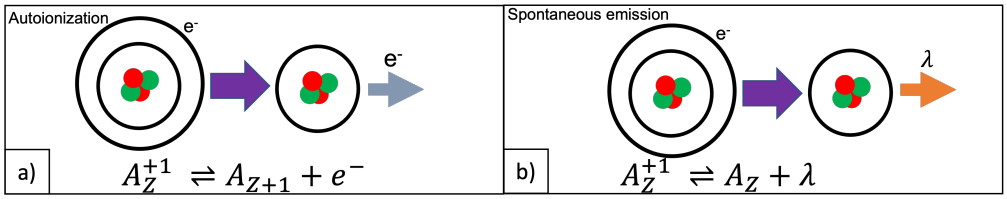

FIGURE 2.3: a) Autoionization b) spontaneous emission

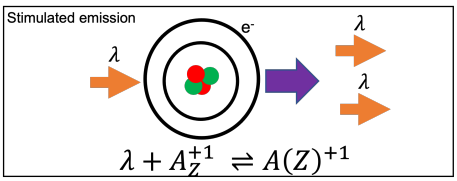

FIGURE 2.4: Atomic process of stimulated emission

2.1.4 Stimulated emission

A photo-atomic only process is stimulated emission, the mechanism for our lasers, Light Amplification by Stimulated Emission of Radiation. Stimulated emission occurs when a photon triggers an atomic system to emit a photon due to the de-excitation of an electron to a lower energy state, see Fig. 2.4.

2.1.5 Dielectronic recombination

There is another recombination processes known as dielectronic recombination. This atomic process is in a sense a two-step process, an inverse process to that of autoionization. First an inbound electron collides with a positive ion. The inbound electron may excite an electron of the ion. If the inbound electron looses all of its kinetic energy to the excitation of the bound electron of the system it will be captured. Once this has occurred the atomic system can simply reverse the process through autoionization. The system may also emit a photon with energy characteristic to the doubly excited state of the system, see Fig. 2.5.

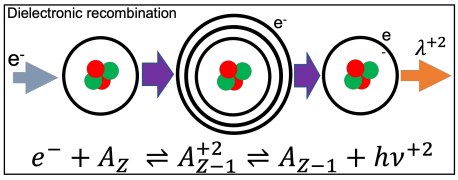

FIGURE 2.5: Atomic process of dielectronic recombination

2.2 Photoionized Plasmas

In reality, both photo-atomic and electro-atomic processes are occurring at the same time, it's just a matter of at what rate. Now that we have the tools to describe the underlying atomic framework that plasma physics relies on, we can now more accurately discuss and define more precisely properties and characteristics of plasmas. Thus, to start we can be more specific, a plasma is considered to be photoionized or collisional when the dominate atomic mechanisms are either photo electron processes or electron-electron. In the following sections we will explore some of the basic properties of plasmas and how we can build on top of them to produce different tools and metrics we can use to differentiate and characterize plasmas.

2.2.1 Plasma properties

Many of the properties of plasmas are similar to common objects. What makes plasma unusual and abnormal is the range in parameters spaces they cover. When headed out to back country ski, it's important to know the conditions aka the properties of the snow. Depending on the temperature and the density of the snow, avalanche conditions could be high or low. For plasmas an example of some fundamental parameters are: temperature, density, and average charged state. Density is pretty straight forward, how much of something is there in a given volume. For plasmas there are a couple of different ways we can slice this quantity. Since plasmas are inherently a combination of positive nuclei and negative free electrons, we can characterize the density of a plasma with respect to the ion density and the electron number density. Similarly, the temperature of

the plasma can be with respect to the ions or to the electrons.

A property that is not quite so basic but fundamental nonetheless is the fractional ion population distribution of a plasma. There are a great number of things one can learn from knowing which ions are active. Each ion has a variety of spectral signatures that give the observer details about what's occurring on the atomic level of the plasma. Based on the radiation flux that is driving the photoionized plasma the plasma will have a distribution of elements with a distribution of ions per element that are directly related to the peak of the radiation distribution of the radiation object. More highly charged plasma will have ion fractional populations weighted more with highly charged ions. Similarly, the averaged charge state, the number of free electrons per atom, reflects the general ionization balance of the plasma

2.2.2 Characterizing photoionized plasmas

2.2.2.1 Ionization parameter

Photoionized plasmas can be characterized by the density of the medium and the ionizing radiation flux driving the system. In astrophysics, the ratio of the incident radiation and the ion density is known as the ionization parameter,

$$\xi = \frac{4\pi L_\nu}{n_e} \tag{2.1}$$

Where, L_ν is the irradiance, the incident radiation on the plasma, with units of Wm^{-2} or more commonly in astrophysics as $erg \cdot cm^2/s$ and n_e is the ion density of the plasma. Therefore, it is the balance of photoionization with respect to recombination in the plasma which is expressed by the ionization parameter, in units of $erg \cdot cm/s$. Astrophysically relevant photoionized plasmas are low density, $n_e < 10^{16}$ and driven by intense radiation sources such as x-ray binary systems like NGC 55 X-1 with $\xi \sim 2000$[55]. Thus, relevant values of $\xi >> 1$ erg $\cdot$ cm/s. Photoionized plasmas are said to be over-ionized when compared to collisional plasmas with the same temperature, because the

charge of the photoionized plasma will much greater than its temperature of collisional counterpart.

2.2.2.2 Photoionization equilibrium

For many astrophysical objects, a balance in ionization is reached between the ionizing radiation flux of the astrophysical object and the plasma resulting in photoionization equilibrium. A decent example from a text, by Osterbrock and Ferland, is given where the approximate conditions of a photoionized plasma using an idealized model a hot star surrounded by hydrogen gas[54]. The approximated form for the photoionization equilibrium is expressed as,

$$n(H^0)\int_{\nu_0}^{\infty}\frac{4\pi J_{nu}}{h\nu}a_\nu(H^0)d\nu = n(H^0)\Gamma(H^0) = n_e n_P \alpha(H^0,T)[cm^{-3}s^{-1}] \tag{2.2}$$

where J_ν is the mean intensity of radiation(energy per area per time per solid angle, per frequency interval), $a_\nu(H^0)$ is the ionization cross-section for Hydrogen from photons with energy ν above threshold $h\nu$ above the threshold $h\nu_0$, $\Gamma(H^0)$ is the number of photoionization per hydrogen atom per unit time, $n(H^0)$, the neutral atom hydrogen density per volume, n_e is the electron density, n_p is the proton density, and $\alpha(H^0,T)$ is the recombination coefficient. Eq 2.2 gives the number of recombinations per volume per time.

Now Eq. 2.2, is neglecting the contribution to electron-electron ionization. For this application out in space where the densities are very low, this factor in negligible. While decent for astrophysics but not exact by any means is the assumption of pure hydrogen. These environments are messy and complex with multiple elemental species. However, what this does for us, is give decent cartoon analogy that can be easily modified and upgraded as we improve in our ability to articulate these phenomena.

2.3 How do we know?

Atomic processes happen at such a small scale, how do we actually know what is happening?

2.3.1 Observation

Photoionized plasmas, and plasma in general, reveal a lot of their secrets through the emission and or absorption of light. Wavelength emitted or absorbed directly corresponds to a particular state defined by the energy of the photon. For the plasmas found around these astrophysical environments x-ray absorption spectroscopy is the predominant method of observation. Such measurements require highly precise spectrometers capable of diffracting light to expose spectral features in the x-ray band. Spectroscopy isn't the only method for investigation of plasmas. For plasmas produced here on Earth in the lab, a variety of diagnostics utilizing lasers and other x-ray sensitive devices can be used.

2.3.2 Simulate and model

The atomic processes when viewed individually don't seem too overwhelming at first, even throw in a couple at a time not so bad. Now, however, let's take a cubic centimeter volume of Hydrogen at room temperature, which approximately has $\sim 5 \times 10^{19}$atoms. This sort of calculation becomes unfathomable for a single human to do let alone an army of mathematicians. This sort of task, however, is perfect for computational devices!

Codes like FAC[19], Cowan's atomic structure code[9], etc., have been developed to handle the quantum mechanical calculations for the atomic wave functions of atomic states of atoms. Such calculations are necessary for more complex problems like the modeling of plasma. Examples of plasma simulation and modeling codes are HELIOS-CR[42], PrismSPECT[41], CRETEN[64], etc. Codes such as these incorporate atomic

structure while also including atomic kinetics, radiation transport, hydrodynamics, and other complex phenomena.

2.4 Summary

This chapter introduced, some of the, fundamental atomic processes that underpin the phenomena that will be explored in the coming chapters. While the individual atomic processes may appear simple, however, when combined into a many atom system is when the complexities start. Plasmas on the other hand, take the challenge to a whole new level.

What was shown is that these energetic systems are sensitive to light and have many different ways in which interaction can happen. This now starts to reveal in more clarity why studying photoionized plasmas can reveal so much about the enormous radiation sources they are found around out in space. Light produced from these objects drives these photoionized plasmas while at the same time encoding rich information about the radiation source into the emergent properties of these photoionized plasmas.

Chapter 3

Radiation Drives

We will first explore in a bit more detail the cosmic engines that radiatively drive the photoionized plasmas found in the surrounding environment. It is important to take this moment, so that we can understand how and why these astrophysical phenomena generate so much energy and power and how we can characterize the radiation produced. Once we have laid out specifics of these magnificent radiators, we will use the parameters as a metric to scrutinize the radiation sources here on Earth.

The second part of this chapter will focus on terrestrial radiation drives. We will first introduce the fundamentals of z-pinches. Building on these fundamentals we will examine their radiative properties. From this survey of z-pinches and the radiation they are capable of producing it will be made clear why z-pinches produce astrophysically relevant x-ray flux for use in laboratory experiments. With this newly developed understanding we will focus our attention on two pulsed-power generators, Zebra and the Z-machine. We will first explore pulsed-power through the lens of Zebra. From Zebra, we will move on to the Z-machine, using our newly developed understanding of Zebra to understand the magnitude of Z.

3.1 High-Energy Astrophysical Phenomena

As discussed, the universe is home to many bizarre and supremely fascinating and highly energetic phenomena. Of these there is a large class of objects that radiate brightly, such as: active-galactic-nuclei and x-ray binary systems. To the naked eye these impressive objects don't exist With a telescope these objects exist in unparalleled artistic fashion. However, it's not until one opens up the spectral hood, revealing encoded information of the object, the radiation source, and the surrounding environment. For now, we will keep our focus to what we can learn about these far off radiation drives and what we can infer about the celestial art pieces that produce them.

3.1.1 Radiation Characteristics

All matter emits radiation known as black-body radiation, which is characteristic to its temperature. More accurately, the spectral distribution of light emitted from matter in thermal equilibrium will have a special functional shape known as a Planckian distribution,

$$B(\nu, T_R) = \frac{2h\nu^3}{c^2} \frac{1}{\frac{h\nu}{e^{k_B T_R}} - 1}, \tag{3.1}$$

where B is the spectral radiance, ν is the frequency of radiation, T is temperature, k_B is the Boltzmann constant, h is the Planck constant, and c is the speed of light. As the temperature increases the spectral distribution tends towards higher energy. The peak of the spectral distribution is characterized by the temperature. This relationship can be derived From Planck's law, known as Wien's displacement law,

$$\nu_{peak} = \frac{\alpha}{h} k_B T_R, \tag{3.2}$$

with α, a constant, $\sim$2.821.

The temperature of the radiator at the surface can be described by the color temperature, T_c. The color temperature, describes the spectral distribution and or "shape" as it relates

to the radiation temperature, T_R.

Now, on the other hand, the brightness temperature, T_B, describes radiation at some distance from the radiator, typically at the location of a detector. As radiation propagates away from the radiating source the flux is reduced, proportionally to $1/r^2$. The spectral distribution is the same with a lower intensity.

3.2 Terrestrial Radiation Drives

We may not have the ability to whip up an active-galactic-nucleus in the lab, we have however ingeniously developed methods that allow us to produce astrophysically relevant conditions. An example of such methods include: pulsed-power generators, lasers, and synchrotrons. While, synchrotrons are used for laboratory astrophysics experiments, the aim of these experiments is much different. The main reason being, that synchrotron light sources produce narrowband radiation; while, the experiments we are focusing on require not only intense light sources but broad-band as well to be relevant to the conditions we are attempting to reproduce.

Of the few laboratory photoionized plasma experiments in existence, they either use pulsed-power generators or lasers. Some of the main machines in use today that can provide astrophysically relevant radiation flux are: Zebra, Z-machine, Omega-EP, NIF, and GECKO. Pulsed-power machines use a current load known as a z-pinch to produce radiation, whereas radiation drives produced from laser use gold (or a high Z) coated hohlraums that when irradiated by intense laser light, produce broadband radiation.

3.2.1 What is a Z-pinch?

A "pinch", in plasma physics, is a phenomenon in which a conducting medium experiences a compressive magnetomotive force as result of a strong current passing through the conductor. One of the earliest documented experiments exploiting the magnetomotive pinch effect[20] was performed by Martinus van Marum in 1790. Marum

constructed a capacitive storage system capable of 1 kJ which he used to explode a wire one meter in length. It was not until 1905 that Polluck and Barraclough theorized that the compression observed in copper tube lightening rods was the result of the Lorentz force, $\vec{J} \times \vec{B}$, causing an implosion, aka a "pinch", of the tube. [34]

There are a variety of pinch schemes, however, the one of most importance and relevance is the Z pinch. A Z pinch derives its name mainly by convention. In plasma physics, the current is described as traveling along the "Z" axis between the two electrodes, thus resulting in compression along the Z axis thus colloquially referred to as a pinch effect, resulting in the terminology Z-pinch.

There are two main styles of Z pinch configurations: gas and wire-array Z pinches, of which there are several versions of each. For gas Z pinches, gas puffs are one of the more common. Gas puff Z pinches work by way of a gas jet that is launched between two electrodes which is subsequently ionized by a current pulse. Wire-array Z pinches as well have a variety of forms and geometry. A wire-array Z pinch can be composed of a single wire up to hundreds of wires. Cylindrical wire-arrays are a common geometry scheme, however, other geometry schemes such as planar, star, and X pinches have been studied. X pinches are interesting in that while the current flow is essentially along the Z axis, the X geometry focuses compression at the central region of the wire-array. The original intent of Z-pinch experiments were to study inertial confinement fusion (ICF). It was found early on that due to two main instabilities, sausage and kink instabilities, z-pinches are not a viable path for ICF.

3.2.2 Z-pinch as a radiation drive

Initially, z-pinches were conceived as a method to realize terrestrial fusion. While, plagued with various instabilities of which compromise confinement integrity, z-pinches are valuable nonetheless. Auxiliary z-pinch studies still support advancements towards fusion. Furthermore, the burst of radiation due to the kinetic energy of the imploding

plasma due to the strong magnetic fields support an array of radiation driven experiments. Most importantly, with regard to the work presented here, the radiation flux possible from Z-pinches is of great value for laboratory astrophysics experiments that require powerful broadband radiation drives.

3.2.3 Pulsed-Power Drivers

The majority of the research presented in this dissertation was conducted with the 1 MA pulsed-power accelerator Zebra at the University of Nevada, Reno. Specifically, the research focused on the photoionization of gas jet targets was performed with Zebra. While, the gas cell photoionization research was conducted at Sandia National Laboratory using the Z-machine.

Pulsed-power generators range from small-scale circuits on the order of amps to large-scale complex machines that can deliver tens of mega amps. While pulsed-power generators range in design they each share a single purpose: produce current pulses that compress energy both in time and space. There are several methods for pulsed-power generators to build and store energy, the two main archetypes are Marx banks and Linear Transformer Drivers (LTDs). However, to date it is the Marxbank generators that have the greatest success in producing large x-ray yields that are necessary for laboratory astrophysics experiments.

The Zebra accelerator and the Z-machine are pulsed-power experimental platforms that use Marx bank architecture for energy generation. A Marx bank is an array of capacitors that can be configured to be in parallel or series based on the state of gas switches. The general operation of a Marx bank starts with charging the capacitors. When charging, the Marx bank, the capacitors are in parallel. Based on standard Marx bank construction, half the capacitors are positively charged while the other half are negatively charged. Standard operation for Zebra and the Z-machine charge the capacitors to 85% of the max voltage rating. Zebra and Z use 1.3 μF capacitors with a max voltage of 100 kV, which results in a standard charge voltage of 85 kV per capacitor. The Marx bank is

stored and operated in an oil tank. The oil serving as a dielectric medium is used to mitigate unintended discharge between the components of the Marx bank. Once the Marx bank has been fully charged gas switches are utilized to change the configuration from parallel to series. When the Marx bank is in series the output voltage is roughly the number of capacitors times the charge voltage of one capacitor. The Marx bank that Zebra utilizes is composed of 32 capacitors. In an idealized approximation, assuming the capacitors that compose the Marx bank are classical parallel plate capacitors, then for one stage with a 1.3 μF capacitor charged to 85 kV the total accumulated charge will be 110.5 mC and a total stored energy of 4.7 kJ. The total capacitance of the Marx bank in series will have capacitance equal to 1/32 of a single capacitor, 40.6 nF. When each capacitor in the Marx bank is charged to 85 kV the total accumulated charge is 3.5 kC and the total stored energy is 146.8 kJ. In this idealized approximation the total resulting possible output voltage is 2.7 MV.

In actuality, the capacitors that compose the Marx bank are not the classical parallel plate design. They are the size of 1-2 car sized batteries with what is essentially a roll of aluminum foil that charge is accumulated on. These capacitors deliver the charge accumulated on the 100s of millisecond scale. In order for a machine like Zebra to achieve MA current pulses the Marx bank is too slow. For this reason, the energy generated in the Marx bank delivered to a humungous capacitor known as the "intermediate storage". The intermediate storage is much closer in design to the classical parallel plate capacitor. Instead of parallel flat plates, the intermediate storage is two concentric cylinders. The purpose of the intermediate storage capacitor is to deliver the energy to the Zebra chamber quickly on the microsecond scale, several orders faster. It is important to note that while the Marx bank is contained within an oil tank, the intermediate storage and the transmission line that leads to the Zebra chamber are contained within a water tank. The water, a dielectric, acts as an insulator for the current transmission line which delivers the pulse from the intermediate storage. Since the water is used as an insulator it is critical that the water is constantly filtered to maintain a resistivity of 1 MΩ or better.

Once the intermediate storage reaches $\sim$1 MV a gas switch known as the rim fire switch breaks down allowing the current to transmit to the water gap. The water gap serves the purpose of reducing the overall jitter of the machine. Interestingly, the water gap is the source of the loud bang produced by firing Zebra and Z. Once the current passes through the water gap it is transmitted through the stack to the magnetically insulated transmission line, colloquially known as the "MITL". The insulator stack and or "stack" is composed of Teflon and stainless steel rings, in a specific shape that promotes the correct flow of current as its being delivered to the "mesa" which in turns delivers the current to the cathode. The shape of the rings within the stack serve to guide electrons to the "mesa". When the current returns through the stack the shape is reversed which allows the natural flow of the return current. The basic operation described here is what allows pulsed-power machines like Zebra and Z to drive loads with large current pulses.

3.2.3.1 Zebra

The Zebra accelerator resides at the University of Nevada, Reno in a satellite laboratory, located in Stead, NV. Originally Zebra came from Los Alamos National Laboratory in 2001. Zebra, is capable of producing 1 MA current pulses with a leading rise time of$\sim$80 ns from 10% to 90%, see figure 3.1. Zebra is capable of larger current pulses of the order 2+ MA when configured with the "load current multiplier" (LCM). [7] From the implosion of wire-array z-pinches Zebra can achieve intense broadband x-ray flux, 0.5-1TW, with integrated photon energy in the range of 12-15kJ with photon energy $\leq$1 keV. An example of an 8-wire cylindrical z-pinch used with Zebra is shown in Fig. 3.2.

3.2.3.2 Z-machine

The Z Facility of Sandia National laboratory in Albuquerque, NM is home to the worlds most powerful pulsed-powered generator, the Z-Machine (Z). Before there was the Z-Machine there was the Particle Beam Fusion Accelerator II.

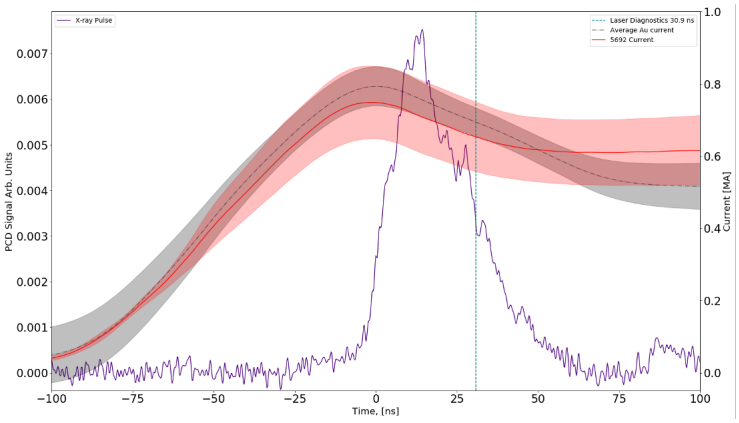

FIGURE 3.1: Zebra diagnostic plot, showing the relative timing between the current pulse profile, x-ray PCD signal, and laser diagnostic timing.

The Z-machine, composed of 36 Marx banks, is capable of electrical power >80 TW and electric current >26 MA. [60] The Z-machine is able to drive Z-pinches with peak emission power >300 TW and total x-ray energy output >2 MJ. Z can be configured to drive a variety of loads: solid liners, gas puffs, and wire arrays. Of these load types, wire-arrays produce the highest power x-ray sources in the photon energy band 0.1-3keV. An example of the wire-arrays used in Z is depicted in Fig. 3.4.

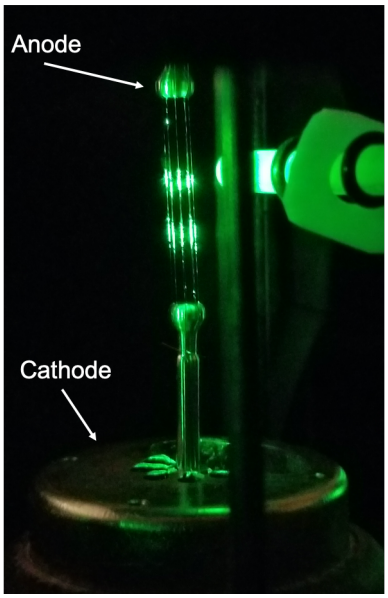

FIGURE 3.2: Example of a cylindrical 8 wire wire-array

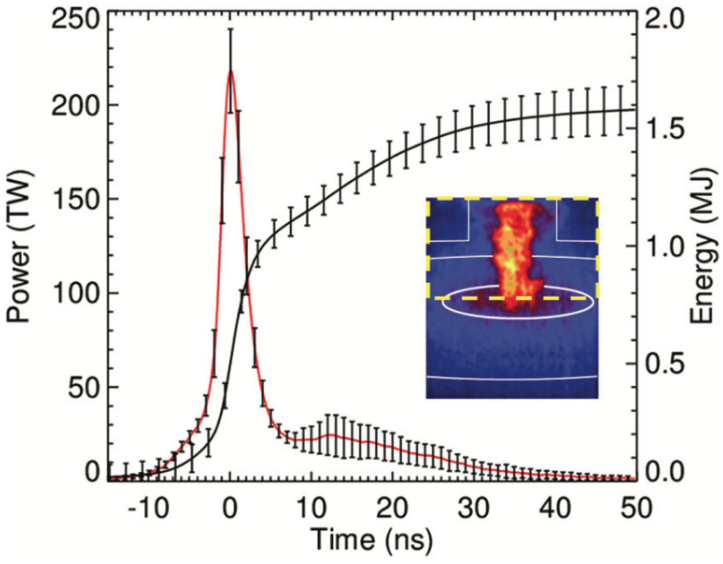

FIGURE 3.3: Power and energy of the x-ray pulse of the ZPDH. [60]

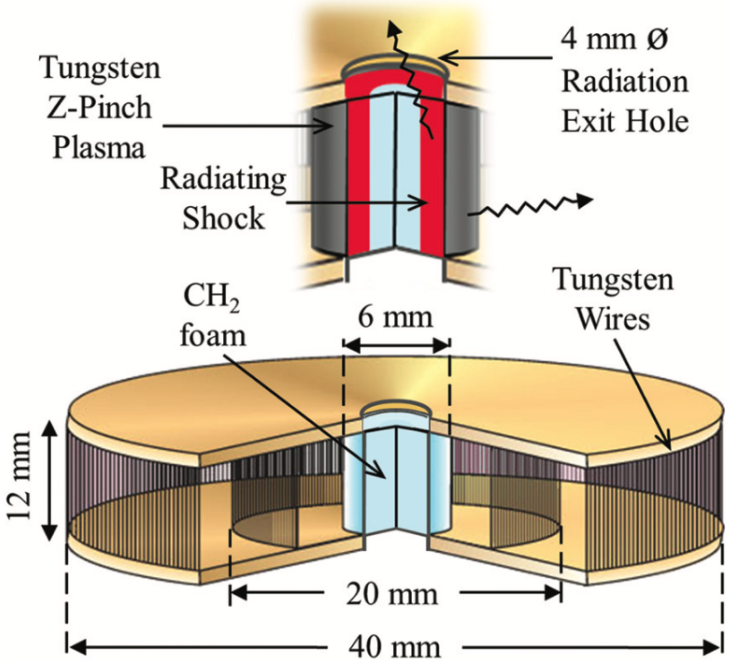

FIGURE 3.4: The z-pinch dynamic hohlraum radiates x-rays either vertically out of the collapsing cylindrical tungsten plasma or radially outward. [60]

3.3 Summary

The purpose of this chapter was two-fold. The first goal was to define the astrophysical context for photoionized plasmas produced by these cosmic engines. The second goal, to define experimental parameters and justify the experimental platforms that we use to bring the cosmos to us. Further, by exploring what is required to perform such experiments, the laboratories used for these experiments were introduced as well as their capabilities.

Chapter 4

Wrangling Zebra's Radiation Drive

As we have seen up until this point, accurately understanding the characteristics of the radiation drives far off in space and the ones here on Earth is of importance. Without understanding the phenomena which sets everything into motion, it is difficult to accurately understand what is occurring. Which brings us to our effort to better understand the radiation drive that Zebra is capable of producing.

4.1 Spectral characterization requirements

For radiation driven experiments, like the ones that will be detailed in the following chapters, it is important to have an in-depth understanding of the spectral distribution of the radiating source. Experimental design benefits greatly from such knowledge, allowing appropriate experiments to move forward and those that require an alternative radiative source to be redesigned. Modeling of radiation driven experiments hinges greatly on precise understanding of the spectral characteristics of the radiation source. With no understanding of the spectral characterization, modeling is a waste of time. With minimal knowledge of the radiation drive very limited approximate understanding of the fundamentals is possible. However, with a robust understanding of the radiation drive, modeling and simulation effort can be a helpful tool that can help expand perspectives and areas of focus for an experiment.

The radiation drive made possible by the ZPDH driven by the Z-machine is a great example. Simulation efforts have gone a long way to help explore what's possible and where to look with these experiments, which in turn improve the understanding of the model. The relevance is made even more dramatic for the case of pulsed-power experiments where shots can be limited, and wise choices can make the difference between success and uninteresting expensive data. For these reasons and more, the spectral wrangling of the radiation drive produced by Zebra is of great importance.

There are a variety of topics and questions that we wanted to answer by studying the spectral distribution of Zebra's radiation drive. Of most importance was, what is the color temperature of the radiation drive produced? Is the radiation drive similar to that of a black body radiator, i.e., is the shape of the distribution similar to that of a Planckian? For the case of the ZPDH spectral distribution from Z it is best characterized by a linear combination of three geometrically diluted Planckians. Of these three Planckians, one represents the main contribution from the pinch while the reradiation from the surrounding hardware is represented by two Planckians. Understanding the radiating behavior of the z-pinch driven by Zebra can help us answer further questions such as, to what degree is the pinch plasma thermalized? Furthermore, in a more general sense, the ability to spectrally characterize z-pinches on Zebra can help answer fundamental z-pinch questions that have been out of reach. An example, what are the early-stage characteristics of low Z z-pinches that have historically been fielded on Zebra. The line emission of z-pinch radiation is rich in information about the dynamics of wire-array z-pinch implosions. Such information is highly valuable as it allows a method to probe the ionization, temperature, and density for all stages of the pinch. Most importantly the spectra has encoded specific information of just how exactly we are driving the photoionized plasmas in the photoionized gas jet experiments. This aids in the experimental development as well as modeling and simulation effort.

There were several criteria that were required for the successful characterization of the spectral distribution of the x-ray flux produced by Zebra for the photoionization

experiments and more generally z-pinch experiments. The first requirement for these measurements was the ability to scan a very large wavelength range. This is a necessary requirement for investigating the spectral behavior of the pinch. The second requirement is that measurements must be quasi-continuous rather than discrete measurements. This is important for several reasons. Mainly, it is unrealistic to scan a large wavelength range with a BUNCH of individual measurements. If the radiation drive was continuous such a scan may be possible. For the case of pulsed-power and specifically Zebra, the x-ray flux pulse is on the order$\sim$25 ns and at most 5 shots can happen in a day (in the before times of lore). Furthermore, due to shot-to-shot variability, discrete individual measurements would be hard to draw real conclusions from. Third, the ultimate goal for such an instrument would be to also use the instrument to perform x-ray absorption measurements like those that are done with the KAP crystal spectrometer in the photoionized gas jet experiments. The very nature of absorption measurements necessitates the need for high resolution continuous measurements. To meet this diagnostic challenge an x-ray grazing incidence diffraction grating spectrograph (XRDGS) was chosen as it meets each of the requirements stated.

4.2 XRDG Spectrograph design

The choice to use a grazing incidence diffraction grating spectrograph was two-fold. Obviously, the diagnostic must meet the requirements stipulated above, which it does in spades. Second, however, there was an available McPherson 1.5-meter Acton ARC GIMS 551 monochromator. Save for the monochromatic, every other aspect of the monochromator was exactly what was needed in terms of instrument construction geometry. Thus, the Acton monochromator was reengineered ... rather rehabilitated to become a 1.5-meter grazing incidence Acton spectrograph utilizing a MCP as the quasi-continuous detector.

4.2.1 Rowland circle geometry

The spectrograph geometry is based on what is known as the Rowland circle. Given a reflective diffraction grating of radius R, a circle with radius r=R/2 can be used to accurately position the illuminating slit, grating, and detector; such that the dispersed light from the 2°grating is in focus along the perimeter of the circle, thus being in focus on the detector. Figure 4.1 shows the Rowland circle geometry for the spectrograph.

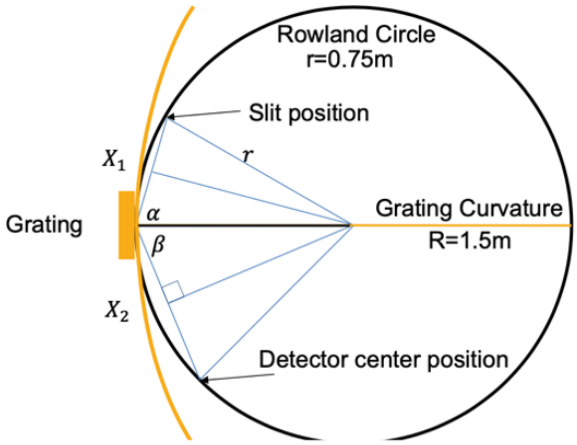

FIGURE 4.1: The Rowland circle geometry for the grazing incidence x-ray reflection diffraction grating spectrograph. The Grating Curvature R=1.5 m, making the Rowland circle radius r=0.75 m. The grazing incidence angle $\alpha = 2^{\circ}$, β is the angle of reflection from the center of the grating. X_1 is the distance of the illuminated slit to the center of the grating, and X_2 is the distance of the central position of the detector to the grating center.

The grating dispersion is simply a function of the grating radius, grating groove density and position from the illuminating slit. The detector placement on the Rowland circle is then defined by the desired central wavelength that falls on the detector. In the spectrograph's former life as a monochromator there is no central wavelength, only a single desired wavelength. Rigorously defined, the grating dispersion relation for a given diffraction order, m, is,

$$m\lambda = d\left[\sqrt{1-\frac{X_1}{2r}} - \sqrt{1-\frac{X_2}{2r}}\right] \tag{4.1}$$

where λ is the desired central wavelength on the detector, X_1 is the distance from slit to grating center, X_2 is the distance between grating center and detector center position. Based on this dispersion equation, the position of the detector, and the length of the detector a specific wavelength range will fall on the detector. Since the dispersion of light from the grating is non-linear the spectral range and spectral density change based on the detector position on the Rowland circle. For the XRDGS, the anamorphic magnification effect is demonstrated in the left plot of Fig. 4.2. As the detector moves from the high energy side of the Rowland circle, near the grating shown in purple (0.0, 0.005), to the low energy side, away from the grating shown in red (-0.4, 0.12), the wavelength range increases and the spectral density increases. This is seen visually in the right plot of Fig. 4.2 by the change in angle of the dispersion plots. This effect can be accentuated if the detector is not perfectly positioned on the Rowland circle.

A secondary effect that is of importance to mention is known as anamorphic magnification. Due to the flat nature of the MCP detector, the spectra that falls on the detector is only in focus in the center, where the detector is positioned directly on the Rowland circle. This means that for spectra recorded on either side of the center, the spectral distribution is deformed. This effect is most noticeable in the high energy regime, when the detector approaches a parallel position with the grating. In the low energy regime, the detector approaches an angle that is perpendicular to the detector. In these positions that effect of anamorphic magnification is less noticeable.

The detector used for in this instrument is a combination of a micro-channel plate (MCP), phosphor screen, and a charged coupled device (CCD). Figure 4.3 shows an areal view of the XRDG spectrograph in its entirety. Figure 4.4 shows a side view of where the MCP, phosphor plate, and CCD are oriented.

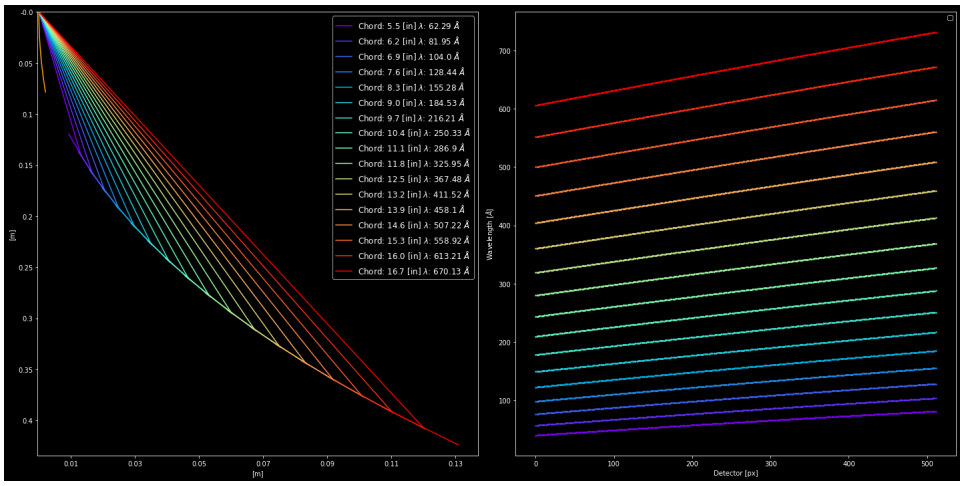

FIGURE 4.2: Demonstration of non-linear dispersion effects and anamorphic magnification. Left: Shows the incremental positions of the central wavelength for positions of the detector along the Rowland circle. Purple traces are of the high energy side of the spectrum and the low energy side of the spectrum denoted by red trace. Right: Wavelength dispersion for each chord position of the detector shown in the right plot. Colors correspond between the plots. As the detector moves from high to low energy the dispersion increases and the spectral density increases.

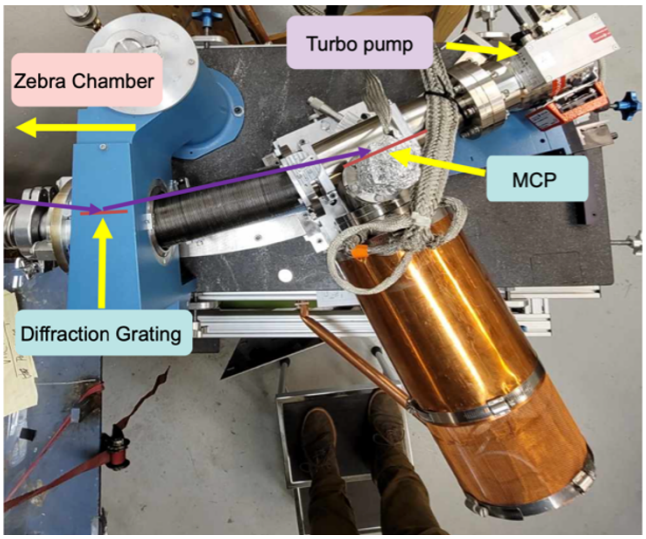

FIGURE 4.3: Areal view of the grazing incidence x-ray reflection diffraction grating spectrograph.

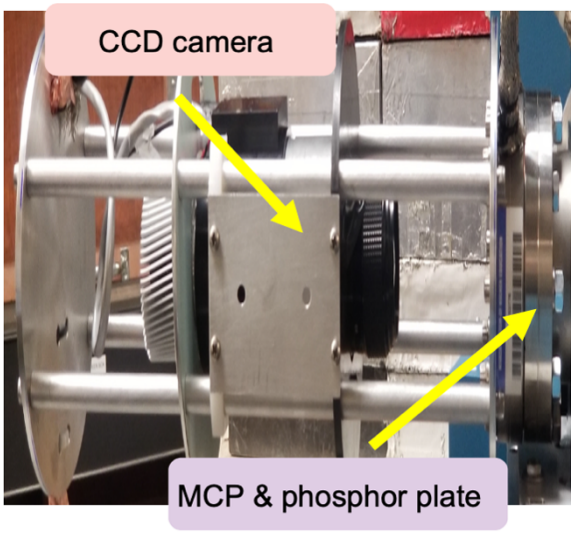

FIGURE 4.4: Detector Assembly for the XRDGS.

4.3 Experimental Setup

For these spectral characterization studies, the setup was straightforward with primary focus on the XRDG spectrograph. Cylindrical wire-arrays constructed with aluminum (Z=13), titanium (Z=22), nickel (Z=28), molybdenum (Z=42), tungsten (Z=74), and gold (Z=79), as well as, wire-arrays of stainless steel(∼88% iron (Z=26), ∼10% chromium (Z=24), ∼1% carbon (Z=6)). The wire-arrays investigated were 4 and 8 wire arrays 2.5 cm tall and 6-8 mm diameter, Fig. 4.5 shows a side-on view of an example wire-array for these studies.

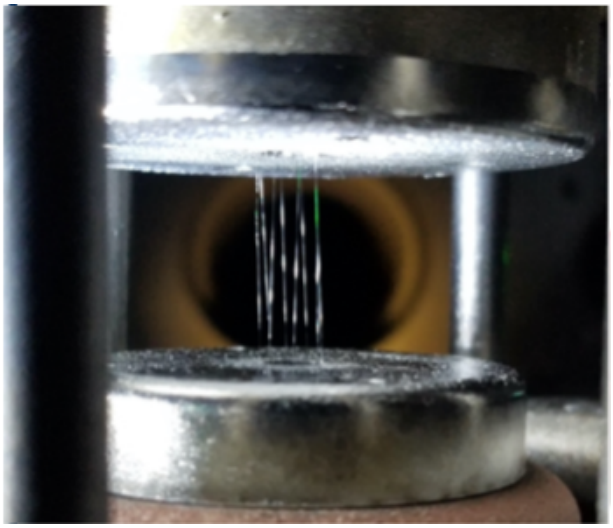

FIGURE 4.5: *Into the VOID*
Photo of an example Al wire-array used for the z-pinch spectral characterization studies.

The supporting diagnostics utilized were a KAP crystal spectrometer, two frame side-on laser shadowgraphy at 532 nm, x-ray pin-hole imaging, photo-conducting diodes, and B-dots. Figure 4.6 shows the Zebra chamber and the diagnostic line of sight set up for these series of experiments. For an interesting perspective insight, the view in Fig. 4.5 is looking through the wire-array down the line of sight of the XRDG spectrograph(blue arrow).

The auxiliary diagnostics played an important role in understanding the machine and

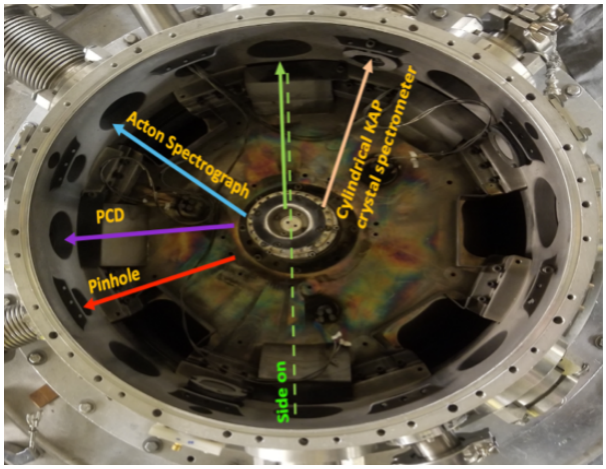

FIGURE 4.6: Zebra chamber diagnostic line of sight set up for the spectral characterization studies.

z-pinch characteristics. Understanding the temporal behavior was important as these diagnostics allowed us to better interpret the data collected with XRDGS. The current profiles, measured with the anode plate b-dots, were analyzed and compared with the X-ray pulse time histories, measured with photoconducting diodes (PCDs), as well as two-frame laser shadowgraphy, at 532 nm. An example of such a comparison is shown in Fig. 4.7. The dashed-dot black line is the average current profile for the aluminum z-pinch wire-array loads used in this series of experiments; while the gray shaded region around the average current profile is the standard deviation. Relative temporality is defined by the peak of the current pulse. The X-ray pulse measured from a PCD is given in purple. The teal dashed line and the orange solid line represent the moments in time that the two-frame laser shadowgraphy took snapshots of the pinch. The delay between the first snapshot and the second is on the order of $\sim$15 ns. While the timing of the laser shadowgraphy looks to be in time with the two later x-ray pulse peaks, this is only a coincidence as the initial snapshot is triggered to be near the peak of the x-ray pulse. As a result of shot-to-shot variability due to inherent machine jitter and the uniqueness of each wire-array the initial snapshot can fluctuate in time around the x-ray pulse peak.

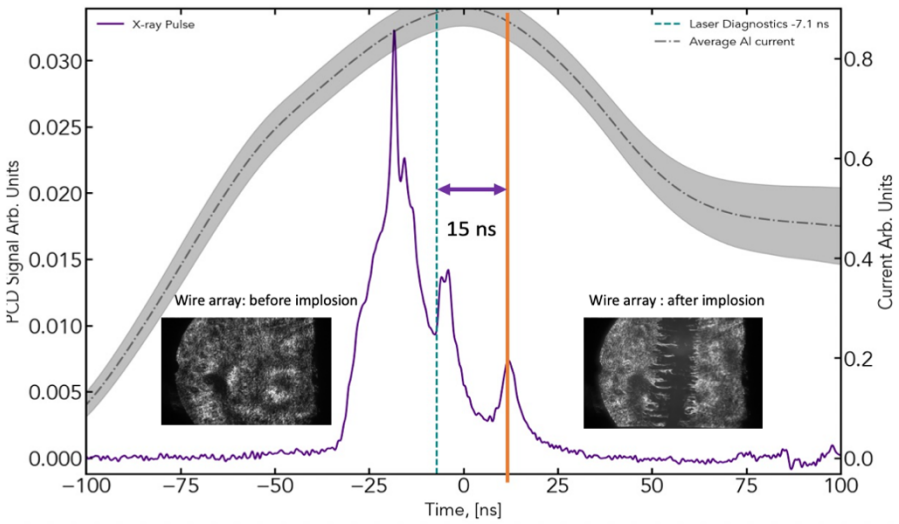

FIGURE 4.7: Plot comparing average Al current (black dash, gray is 1 σ), X-ray pulse (purple), teal dashed, and orange lines are the first and second laser shadowgraphy frames.

4.4 Spectral characterization plan

Due to the breadth of the task at hand it was necessary to develop a focused and disciplined game plan. First and foremost, was to align and focus the spectrograph. In a perfect world, we would have had a variety of calibrated continuous light sources that we could have used to focus and calibrate our wavelength axis with. Instead, however, we found ourselves with the task of using a snapshot like approach with mega amp driver. Saying that this approach was non-ideal would be the understatement of the century. Yet this is what we had, and we made it work! While first light was relieving, it was the first legitimate spectra we recorded that was very exciting, see the left image of Fig. 4.8. At first, however, we were not sure what we had (see the right image of Fig. 4.8) As well we were *cough* looking at the spectrum rotated 90 degrees. Once we had basic alignment and actual intelligible focus it was time for our spectral SAFARI!

While the Rowland circle geometry is of a precise nature, still only a first order approximation, the position of the detector on the circle defines the central wavelength, the rehabilitation of the instrument was fresh! What this meant was that we had a general

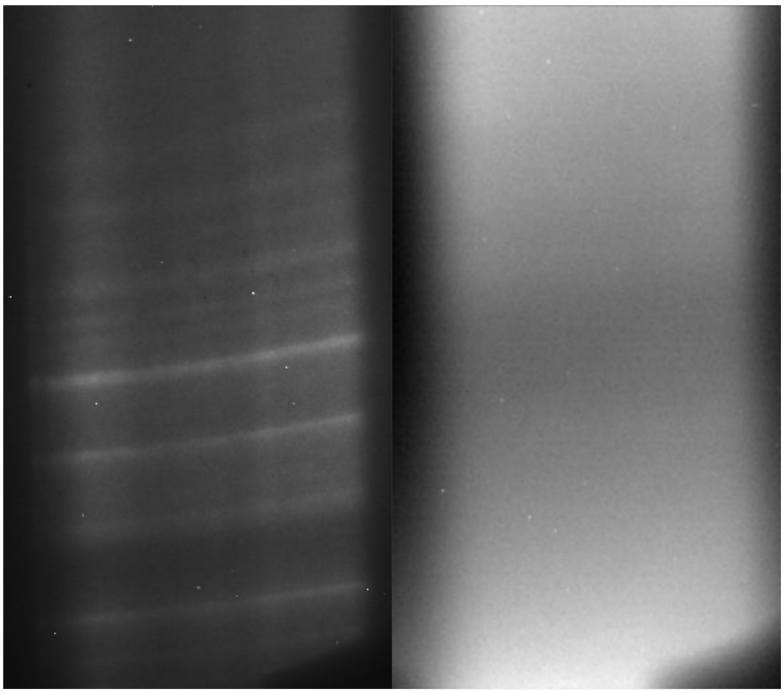

FIGURE 4.8: Examples of initial recorded spectra. High energy (short wavelength) is at the bottom of the images and low energy (long wavelength) is at the top of the images. Left image: First legitimate spectra recorded with the XRDG spectrograph. Right image: Actual first spectra recorded.

idea of where we should be, however, in a realm of bizarre bar codes, finding one's way is not as straightforward and can be confusing. For example, keeping the same chord position on the Rowland circle and changing the offset of the detector from the circle or the angular tilt of the detector can have dramatic effects, making two identical spectra look anything but identical. In other words, the combination of two non-linear effects dispersion and anamorphic magnification was quite the trick! Thus, wavelength calibration of the XRDG spectrograph was challenging and required a disciplined step-by-step approach, rather a bang-by-bang approach! The plan for this was to use a low Z z-pinch that would have copious amounts of emission features useful for finding our place in this excessively gigantic spectral range.

Again, however, back to the far from perfect world scenario. We did not have the luxury to first dial in the wavelength axis; before investigating the radiation drives that were of

importance to the photoionization experiments. Thus, our rather clever plan was for each chord position we investigated we recorded spectra of Al, W, and Au, using the Al emission features as a fingerprint for that chord position. On top of that we made sure to overlap the spectra from shot to shot for the purpose of linking Al emission features together. While, the non-linear effects of dispersion and anamorphic magnification effects were tricky, it provided a rather fun game from shot-to-shot. The game being can you find the line emission group from one shot to the next? As an example, the raw in the lab experience for shots 5680 and 5681 are shown in Fig. 4.9. Before jumping to the next page, see if you can find where the line emission groups match between 5680 and 5681. When you are ready, (no cheating!!), check out Fig. 4.10. The deformation yet consistent relative spacing of the emission features is a classic example, dare I say text book?..., of the non-linear dispersion due to moving further down on the Rowland circle.

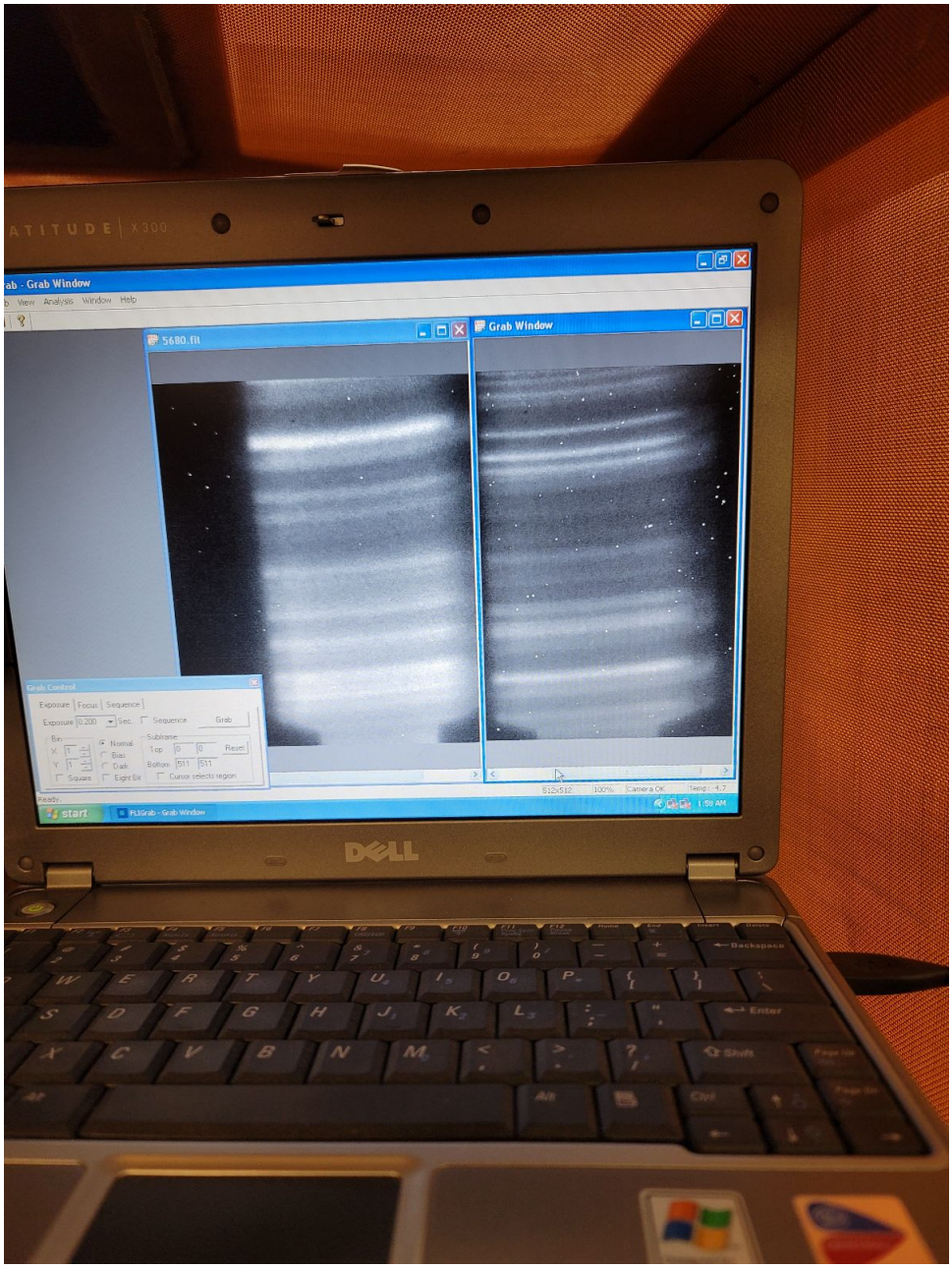

FIGURE 4.9: Image of raw data comparison in the lab for shots 5680 and 5681. Can you see the line emission group that corresponds between the two images? No peaking!

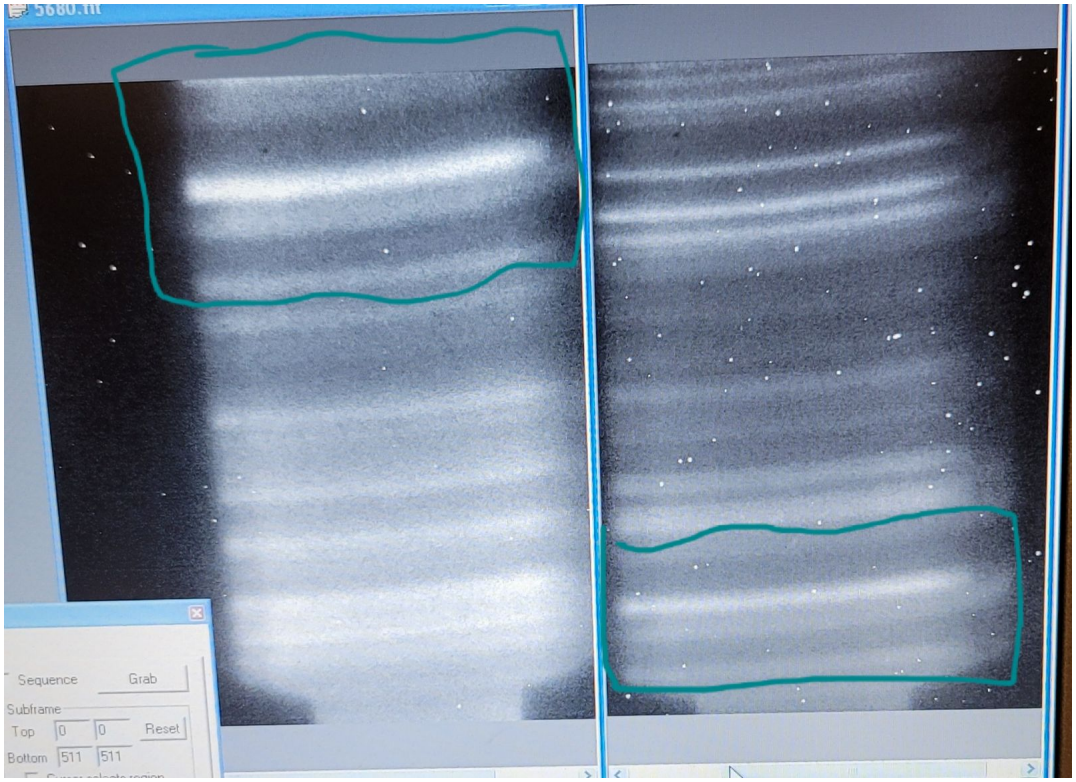

FIGURE 4.10: Image of raw data comparison in the lab for shots 5680 and 5681. The overlapping line emission group is highlighted with the blue box.

4.5 Summary

The rehabilitation and transformation of the McPherson 1.5-meter Acton ARC GIMS 551 monochromator into the grazing incidence X-ray reflection diffraction grating spectrometer represent an important advancement for the diagnostic capabilities of the Zebra accelerator and the Leopard laser at the Zebra Pulsed-Power Laboratory. Spectral characterization of the radiation drive produced by Zebra is an important task. It is crucial for high quality and precision modeling of radiation driven experiments on Zebra. Further, an improved understanding of z-pinch dynamics benefits a multitude of z-pinch experiments on Zebra.

Chapter 5

The Photoionized Supersonic Gas Jet Experiments

The photoionized gas jet experiment was conceived as a solution to the laboratory photoionized plasma data paucity problem. [2] Typically laboratory photoionized plasma experiments have been relegated to large-scale pulsed-power machines initially designed for inertial confinement fusion experiments, such as the Z-machine. Now, by utilizing supersonic gas jets as an interaction medium, photoionized plasmas have been studied with university scale, ∼1MA, pulsed-power drivers.

5.1 The Supersonic Gas Jet Platform

The supersonic gas jet platform developed for the Zebra accelerator, provides the first experimental method for studying astrophysically relevant laboratory produced photoionized plasmas using university scale pulsed-power machines, ∼1MA. X-ray flux from the implosion of a wire-array z-pinch serves two purposes. The first is to excite and ionize the supersonic gas jet, producing a photoionized plasma. The second, is to backlight the photoionized plasma jet for x-ray absorption spectroscopy diagnosis.

To achieve astrophysically relevant x-ray flux, gold (Au) and tungsten (W), 3 mm in diameter cylindrical wire-arrays 25 mm tall were used. Typically, wire-array loads

fielded with Zebra are 8-16 mm in diameter and 20 mm in height. [33] A 3 mm diameter was chosen because it has been shown previously that 3-5 mm diameter cylindrical wire-arrays generate the largest X-ray power on Zebra. [30] In addition to being more powerful, closer placement of the ionization medium to the pinch can be achieved using smaller diameter wire-arrays. With these loads, the Zebra accelerator is capable of generating a ∼25 ns x-ray pulse with 12-15 kJ of integrated photon energy and x-ray photons under 1 keV in energy. Typical power output of these Z-pinches are up to 0.5 TW, and the radiation temperature is ∼40-50 eV, if a blackbody model is applied. Unlike the Z-machine which is capable of a ∼5 ns x-ray pulse with >2 MJ of photon energy in the photon energy band of 0.1-3 keV. Typical x-ray power output of Z is > 300 TW corresponding to a linear combination of three Planckians. Interestingly, Zebra produces much longer duration x-ray pulses, see Fig. 5.3(a). This means Zebra is more likely to achieve photoionization equilibrium (PIE). However, due to the large difference in radiation flux possible between Z and Zebra, it was vital that we utilize as much of the x-ray flux possible to produce astrophysically relevant photoionized plasma.

5.1.1 Why Gas Jets?

Gas jets have proven to be useful for a variety of fields such as ICF[11], x-ray lasers[26], plasma acceleration[24, 68], and more generally laser plasma experiments. [39, 53, 43, 17] Depending on the application, gas jets have a multitude of attributes that can be exploited[44, 65]. Jet geometry can be cylindrical or rectangular[11, 63]. Cross-section density profiles can be tuned, allowing for parabolic and quasi-uniform density gradients. For our application, the goal was to produce a uniform millimeter scale volume of gas to be irradiated. Of the plethora of gas jet choices, supersonic gas jets were the ideal candidate.

A supersonic gas jet has the special characteristic that it is a cylindrical collimated gas flow. Utilizing a millimeter scale nozzle collimated gas, flows, millimeter in scale, can be produced. The gas jets can be produced 5-7 mm away from the Z-pinch within the

return current cage, about an order of magnitude closer than the gas cells in the Z experiments. Further, by utilizing gas jets as targets there is no need for a containment device. A bonus effect of using gas jets is that there is no intermediate regions between the radiation source and the target, for example the windows of the gas cell[50] or the tamping of the foils. [40] The lack of attenuating material between the radiation source and the ionization medium has two main benefits. The first benefit is that the ionization medium, the gas jet, experiences the full power of the Z-pinch. The second benefit is that there are no shocks that result from rapid expansion of said attenuating material that perturb the plasma serve to increase the complexity of the system. Further, the gas jet translates $\sim$17-20 μm during the X-ray pulse. The result being that the cylindrical millimeter-scale volume of gas is effectively "frozen" in space during the X-ray pulse.

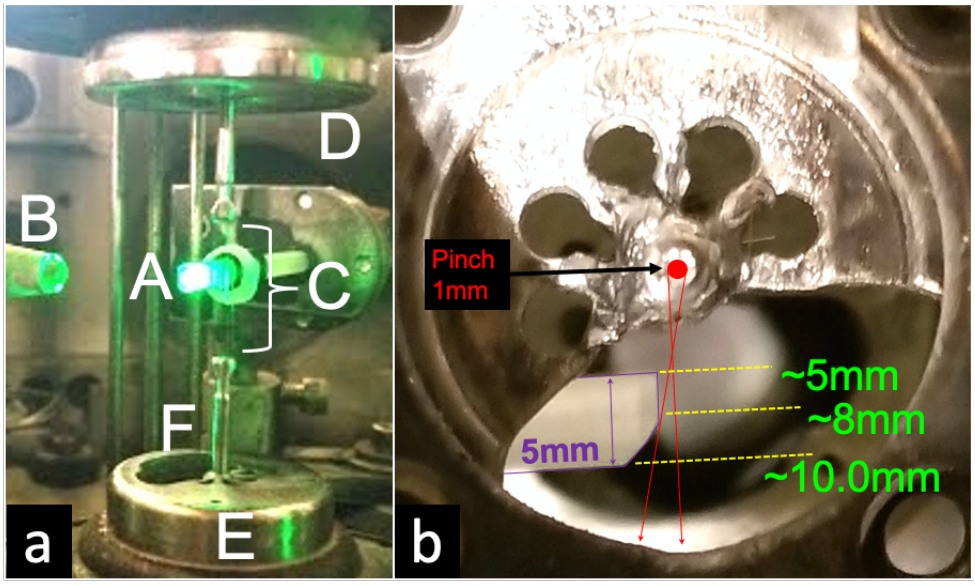

FIGURE 5.1: a: Horizontal perspective. A: nozzle tip, B: spectrometer collimator, C: wire-array, D: anode, E: cathode, F: vertical laser diagnostic window. b: Vertical view of the anode, with nozzle visible in the vertical laser diagnostic window.

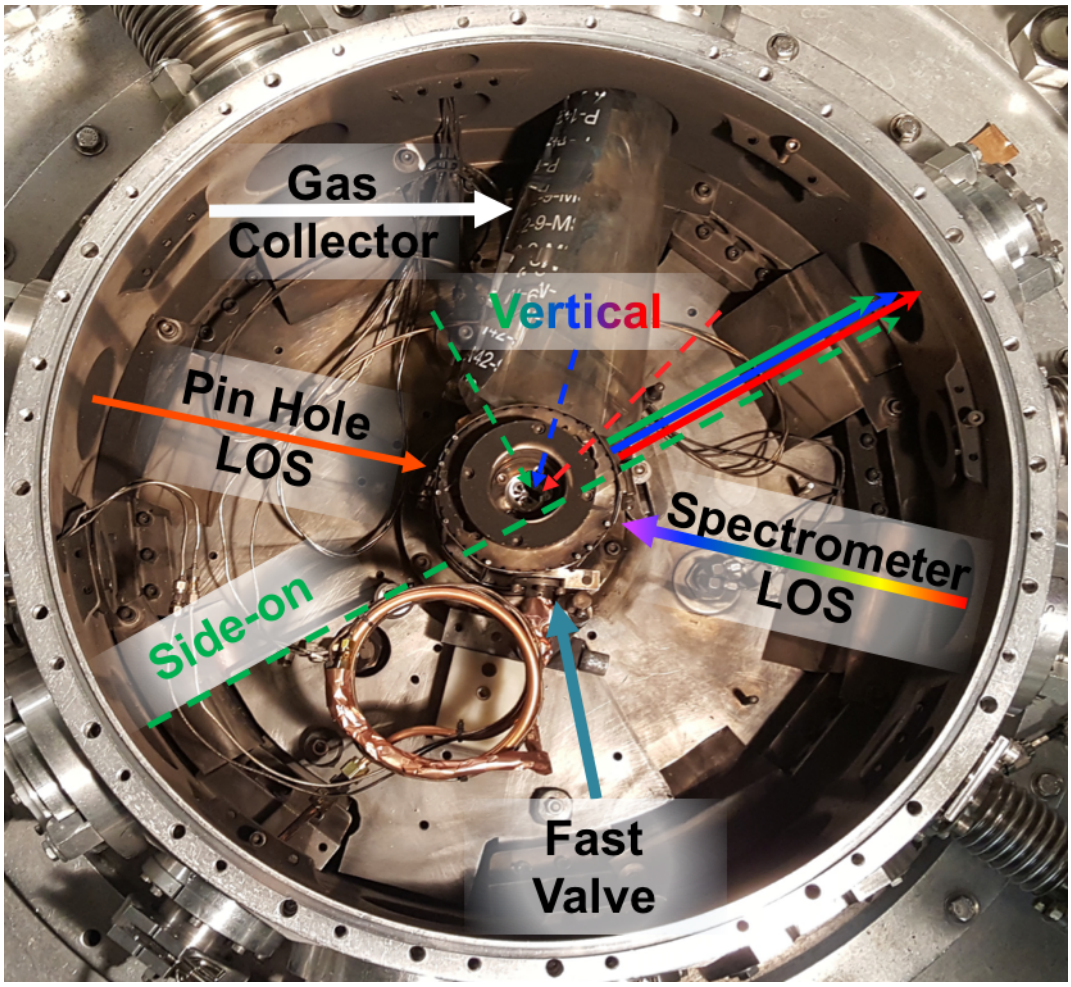

FIGURE 5.2: Top view of the Zebra chamber. Diagnostic line of sights shown for: Vertical and Side-on interferometry, KAP spectrometer, x-ray pinhole imager, and PCD, XRD, and Bolometer (Bolo). Platform components shown are: Gas collector, gas line, and fast valve.

5.2 Diagnostics

The diagnostics used for these experiments include: side-on and vertical laser probing, X-ray spectroscopy, photo-conducting detectors (PCDs), X-ray detectors (XRDs), X-ray pin-hole imaging, and bolometery. The configuration of the diagnostics in and around the Zebra chamber for the photoionized gas jet campaigns is depicted in Fig. 5.3(b). The current produced by Zebra is measured via B-dot and V-dot probes placed along the current path and within the Zebra chamber anode plate. The three b-dots installed within the anode plate are used to measure the load current through the z-pinch. Diagnostic timing is coordinated via a V-dot probe placed before the magnetically insulated transmission line. Laser diagnostics are delayed to be coincident with the X-ray pulse, see Fig. 5.3.

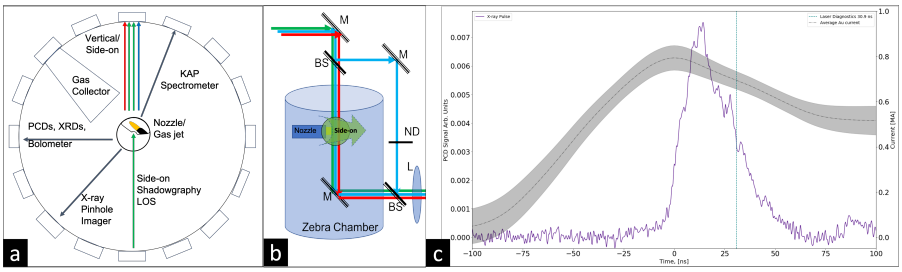

FIGURE 5.3: a: Vertical diagnostic schematic of the Zebra chamber. b: Side-on perspective diagnostic schematic of the Zebra chamber. c: Timing plot of current(red trace), average Au current(black trace), X-ray burst(purple trace), timing of laser diagnostic pulse(green dashed line).

5.2.1 Laser Diagnostics

A multitude of laser diagnostics were fielded for the photoionized gas jet campaigns, which include: Mach-Zehnder (MZ) interferometry, air-wedge (AW) shearing differential interferometry, shadowgraphy, and Schlieren. The laser diagnostics used an EKSPLA SL334, Nd:YAG, laser with a 150 ps pulse duration operating at wavelengths 1064, 532, 266, and 213 nm. [33] A charge-coupled-device (CCD) was used to record images during the experiment for each laser diagnostic channel. Narrowband interference filters were

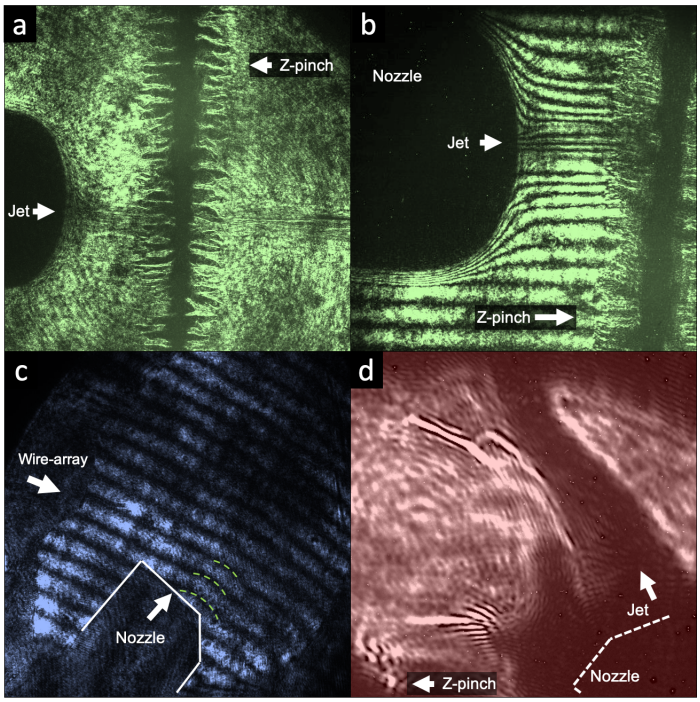

FIGURE 5.4: a: Side-on shadowgraphy(λ= 532 nm) of gas jet nozzle, Z-pinch, and photoionized neon gas jet with 500 psi backing pressure. b: Side-on air-wedge shearing interferogram(λ= 532 nm) of photoionized neon gas jet with 500 psi backing pressure and Z-pinch. c: Vertical Mach-Zehnder(λ= 266 nm) of argon gas jet with 600 psi backing pressure before a Zebra shot. d: Vertical shadowgraph(λ= 1064 nm) of photoionized neon gas jet with 400 psi backing pressure.

used to block the intense light produced from the z-pinch, removing noise from the laser diagnostics.

5.2.1.1 Shadowgraphy

Laser shadowgraphy, aka "fancy laser shadow image", is a basic yet important and widely used technique. While shadowgraphy is typically used qualitatively the physical principle behind shadowgraphy can be exploited for quantitative analysis of electron density and temperature, n_e and T_e respectively. The absorption of the laser light that causes this "fancy shadow" is due to bremsstrahlung absorption(i.e. inverse bremsstrahlung / free-free absorption). The coefficient of inverse bremsstrahlung, in units of cm^{-1}, is proportional to the square of the probing laser wavelength, λ, defined

in the following manner,[33]

$$\delta = 8.73 \cdot 10^{-30} \cdot \lambda^2 \cdot \frac{n_e^2 \cdot Z \cdot \Lambda}{T_e^{\frac{3}{2}} \cdot \left(1 - \frac{n_e}{n_c}\right)^{\frac{1}{2}}}; \tag{5.1}$$

where Λ is the Coulomb logarithm, Z is the ionic charge, T_e is the electron temperature in eV, and n_c is the critical electron density of which the laser wavelength λ in cm^{-3} can propagate through before becoming an evanescent wave unable to transmit through. The Coulomb logarithm

$$\Lambda = [24 - ln(n_e^{\frac{1}{2}} \cdot T_e^{\frac{-3}{2}})], \tag{5.2}$$

handles the relative importance of small-angle collisions to that of large-angle collisions.

For these experiments multi-color shadowgraphy was implemented in a variety of perspectives, both before and during the Zebra shot. Before the Zebra shot, 532 nm side-on shadowgraphy allowed verification of the nozzle placement with respect to the wire-array. As well, allowing a secondary method to inspect the wires of the wire-array to make sure they are intact.

During the Zebra shot, the side-on shadowgraphy channel is used to image the nozzle, photoionized plasma jet, and the stagnated Z-pinch, see Fig. 5.4. Such shadowgraphy, while mainly qualitative, has proven to be very useful for understanding characteristics of the jet during the shot, such as jet performance and ionization of the jet. As well, because there is an inherent jitter with the interrelated timing of the diagnostics with Zebra, the side-on shadowgraphy reveals the stage of z-pinch at which the laser diagnostic snapshot has captured. Further, this perspective is one of several that we can use to confirm whether or not accidental discharge of the current into the jet has taken place (see Sec. 5.4.3).

Dual-color shadowgraphy, 266 and 1064 nm, was used as a method to assess homogeneity of the photoionization of the gas jet. For shots that investigated the photoionization

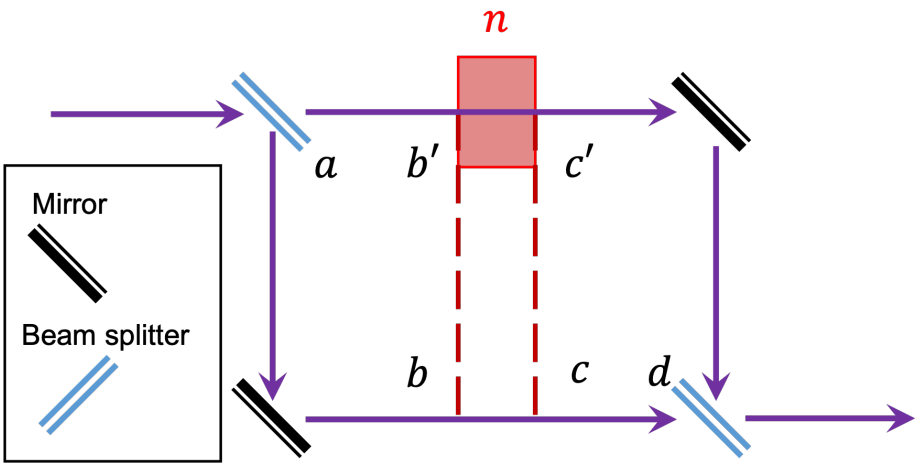

FIGURE 5.5: Optical schematic for a Mach-Zehnder interferometer, for a discrete media of uniform index of refraction. A specific example that illustrates the optical path lengths for the two beam paths: target beam path: $OPL_{a,b',c',d}$ and reference beam path: $OPL_{a,b,c,d}$

of gas jets produced with low backing pressures IR shadowgraphy at 1064 nm was used (Fig. 5.4.D), in order to have a diagnostic that was sensitive to low the electron density.

5.2.1.2 Mach-Zehnder interferometer

Before the Zebra shot, the atomic density of the gas jet is characterized with a Mach-Zehnder interferometry, operating at a wavelength of λ=266 nm or 213 nm, with a resolution of 15.0 μm. A typical Mach-Zehnder implementation is shown in Fig. 5.5. The phase shift in radians [Eq. 5.3] due to a discrete uniform media with refractive index, n', measured with a Mach-Zehnder interferometer is the integrated difference of the refractive index difference between the two beam paths.

$$\phi = \frac{2\pi}{\lambda} \int_0^L (n' - n) dx. \tag{5.3}$$

Now, for the application of probing neutral gas jets and photoionized gas jets, the situation is a bit more complex. The jets, instead of being rectangular and uniform, they are cylindrical and have a radial density distribution. Transforming to cylindrical

coordinates we arrive at Eq. 5.4. Once the expression for the phase shift is in cylindrical coordinates an Abel inversion can be applied to unfold index of refraction as a function of radius[Eq. 5.5].

$$\phi = \frac{2\pi}{\lambda}\int_0^{r_0}\frac{n'(r)-1}{(r^2-y^2)^{\frac{1}{2}}}rdr. \tag{5.4}$$

$$n'(r) = 1 - \frac{\lambda}{4\pi^2}\int_r^{r_0}\frac{\phi(x)}{(x^2-y^2)^{1/2}}dx \tag{5.5}$$

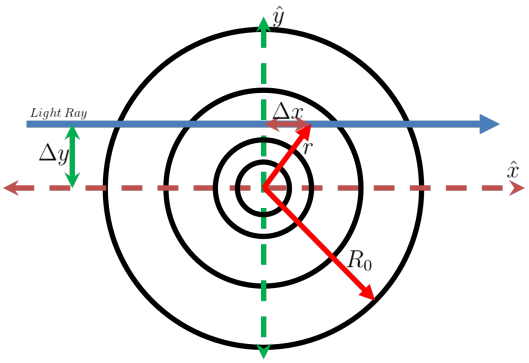

FIGURE 5.6: Abel inversion schematic, which transforms a cylindrically symmetric object from image space to object space.

Once the refractive index has been extracted from the phase information atomic or molecular density, N, can be solved for via the Lorentz-Lorenz equation

$$\frac{4}{3}N\alpha = \frac{(n^2-1)}{(n^2+2)}, \tag{5.6}$$

if the polarizability of the medium, α, is known. The calculated density values can be improved upon by using measured values for the index of refraction for the specific wavelength of the probe laser[44, 18]. The density of the gas jet can be calculated from the ratio of the gas jet density and the density of the gas at standard temperature and pressure.

$$N = \frac{(n-1)}{(n_0-1)} N_o, \tag{5.7}$$

where $N_o = 2.68 \times 10^{19} cm^{-3}$ is the number density of an ideal gas at standard temperature and pressure and n_o is the measured index of refraction of the medium.

5.2.1.3 Air-wedge shearing differential interferometer

During the Zebra shot two air-wedge shearing differential interferometers operating at wavelengths of λ = 532 nm and λ = 266 nm are used to measure the electron number density of the photoionized gas jet, see Fig 5.7. As well, a side-on 532 nm air-wedge interferometer allows another angle to assess photoionization uniformity of the gas jet (see Fig. 5.4).

The air-wedge interferometer is capable of measuring higher electron density than the Mach-Zehnder interferometer. The phase shift measured by an air-wedge interferometer is given by,

$$\phi = 4.46 \cdot 10^{-14} \lambda \int_0^L n_e(x) dx, \tag{5.8}$$

where ϕ is the phase shift measured in fringes, λ is the wavelength of the probe laser measured in cm, L is the length of the medium. A side by side comparison of the extracted phase shift maps from shot with neon at 400 psi probed at wavelengths λ = 532 nm and λ = 266 nm is shown in figure 5.7. From the phase shift one can quickly solve for the electron areal density, as it is simply the phase shift scaled by a constant factor;

$$n_e^{areal} = 4.46 \cdot 10^{14} \lambda^{-1} \phi \tag{5.9}$$

In a similar fashion to the neutral gas jet analysis, we can capitalize on the cylindrical symmetry of the photoionized plasma jet. We can convert the Cartesian representation

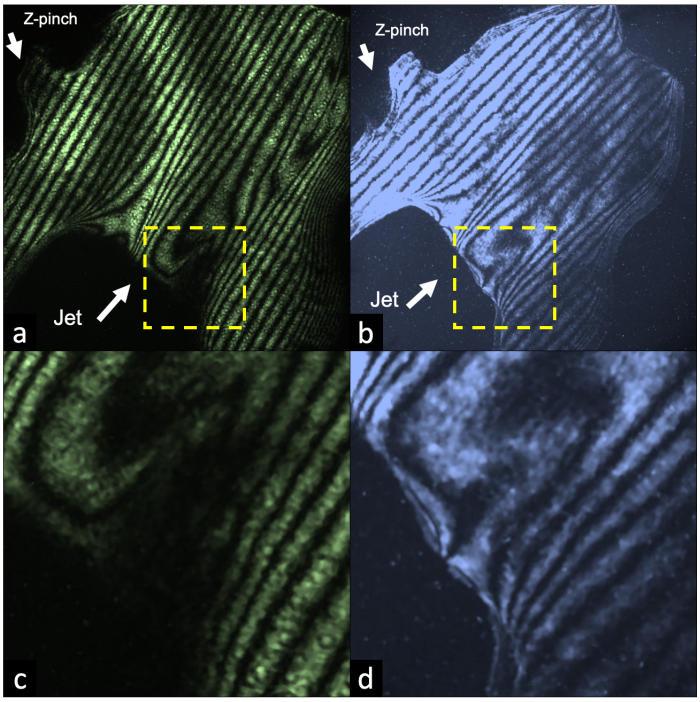

FIGURE 5.7: Photoionized neon gas jet with 400 psi backing pressure. a: Air-wedge shearing interferogram with λ= 532 nm. b: Air-wedge shearing interferogram with λ= 266 nm. c: Expanded view of dense plasma from a. d: Expanded view of dense plasma from b

of the phase shift to a cylindrical representation.

$$\phi = \frac{2\pi}{\lambda n_c} = \int_y^{R_0} \frac{n_e(r)}{\sqrt{r^2 - y^2}} r dr. \tag{5.10}$$

As was done with the neutral gas jet analysis, we can employ the inverse Abel transform to unfold the electron number density from the measured phase shift.

$$n_e(r) = -\frac{\lambda n_c}{\pi} \int_r^{R_0} \frac{d\phi(y)}{dy} \frac{dy}{\sqrt{y^2 - r^2}}. \tag{5.11}$$

The side-on air-wedge interferometer shares the same line of sight as the shadowgraphy channel, which observes the side-on structure of the plasma jet. A quantitative analysis of the side-on air-wedge interferometry was not performed, due to the fact that the side-on

line of sight views the nozzle and wire-array at angle instead of directly perpendicular. This angled view is the result of prioritizing the perpendicular view of the gas jet for the x-ray spectrometer, see Fig. 5.3. Hence, the side-on air-wedge interferometer is used primarily to gather qualitative information about the z-pinch and the photoionized gas jet.

5.2.2 Spectroscopy

A variety of time-integrated and time-resolved X-ray diagnostics were employed for the photoionized gas jet experimental campaigns. For time-integrated x-ray diagnostics we implemented X-ray absorption spectroscopy and X-ray pinhole imaging. The spectral range of interest for x-ray absorption spectroscopy is ∼800-950 eV, 13-16Å. The time-resolved x-ray diagnostics included: photo-conducting diodes (PCDs), X-ray diodes (XRDs), and bolometery. The PCDs and XRDs were used to record the time evolution and X-ray power of several discrete X-ray emission bands from the Z-pinch. The bolometer was used to measure total broadband X-ray power of the Z-pinch.

5.2.2.1 KAP Crystal Spectrometer

Time-integrated X-ray absorption spectra was recorded using a concave cylindrically bent KAP crystal spectrometer using Kodak Biomax film. The KAP crystal has a 2d lattice spacing of 26.6Åwith a 15 cm radius of curvature. The range of spectral resolution for these KAP crystals used was, $\lambda/\Delta\lambda$ ∼800-1000. A 1-2 μm Mylar filter was used to protect the KAP crystal from plasma debris and a fast shutter was also used to protect the crystal from larger debris. An 8 μm thick beryllium filter was used directly in the X-ray film cassette to block optical emission from the pinch. The spectrometer was fielded with slit width range of 0.8-1.2 mm, with the slit oriented perpendicular to the axis of the pinch. In this orientation the slit spatially resolves the width of the plasma jet. Typically, the Z-pinch emission spectrum is clearly differentiated in space from the absorption spectrum of the neon plasma jet. Line outs are taken from Z-pinch emission spectrum

and from the photoionized gas jet plasma absorption spectrum. The wavelength axis is established from the spectrometer calibration shots using nickel and stainless-steel Z-pinches with known spectral lines. A "fog" value, a measurement of film optical depth with no exposure, is subtracted from the line outs. The line outs in optical density are subsequently converted to exposure via the method outlined by Knauer and Marshall [37, 47] for Biomax film made by Kodak. A measurement of the scattered background light intensity is also subtracted out. The last step is to convert the absorption spectrum to a transmission spectrum by dividing the absorption spectrum by the continuum without absorption lines. An experimental transmission spectrum is analyzed by least squares minimization with a collection of synthetic transmission spectra in which the areal density of each ion charge state is varied to find the best fit to the data. The results provide total areal densities for each ion stage, thus giving the charge state distribution of the plasma. The synthetic spectra are calculated using atomic structure data from FAC[19] and line shapes that include natural and Doppler broadening. Absorption transitions within the spectrum arise from ground and low excited states of each ion stage.

5.2.2.2 X-ray pinhole imager

The X-ray pinhole imager was used to gain further insight into the radiation features of the Z-pinch, such as the location of "hot spots" and "cold areas". Hot spots are discrete localized intense X-ray emission sources along the axis of the pinch. These hot spots correlate to the position of implosion bubbles[29] and micro-pinches that form along the axis of the Z-pinch[30]. The hot spots seen in the time-integrated X-ray pinhole image are also seen recorded on the spectrometer X-ray film as horizontal bands where the width of the band corresponds to the size of the emitting hot spot.

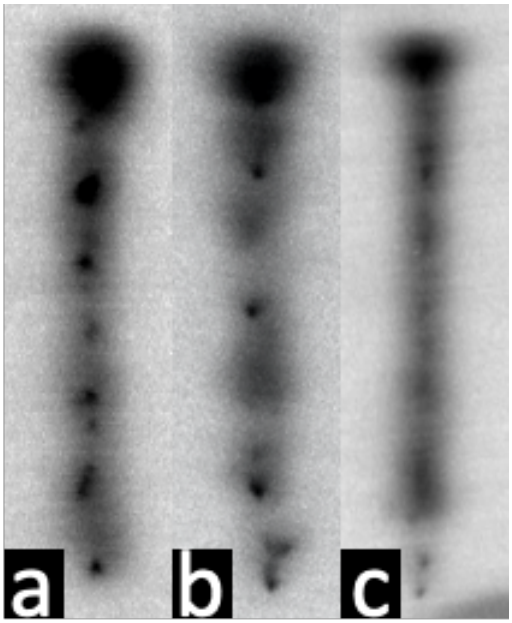

FIGURE 5.8: Time integrated X-ray pinhole images, panels a, b, and c show pinhole images for molybdenum, gold, and gold and stainless steel Z-pinches. Pinhole size is 25 μm.

5.3 IPAs: Interferometry Processing and Analysis Suite

The processing and analysis of interferograms is tricky, as it has predominantly been performed by hand. The initial and most basic idea behind the processing of an interferogram, Mach-Zehnder or Air-wedge, is measuring the deviation of a fringe from its unperturbed reference position. Figure 5.9 shows a Mach-Zehnder interferogram of a neutral nitrogen gas jet with a 1000 psi backing pressure. The inset figure of Fig. 5.9 shows an idealized example of measuring the unperturbed fringe width "W" and the perturbed fringe deviation measurement "S".

For a rudimentary evaluation of phase this can be performed for specific locations of the interferogram. Figure 5.10 shows an example of processing the central vertical axis of the interferogram shown in Fig. 5.9. The results of the phase measurements made in Fig. 5.10 are shown in Fig. 5.11. From this effort we can see the phase shift characteristics

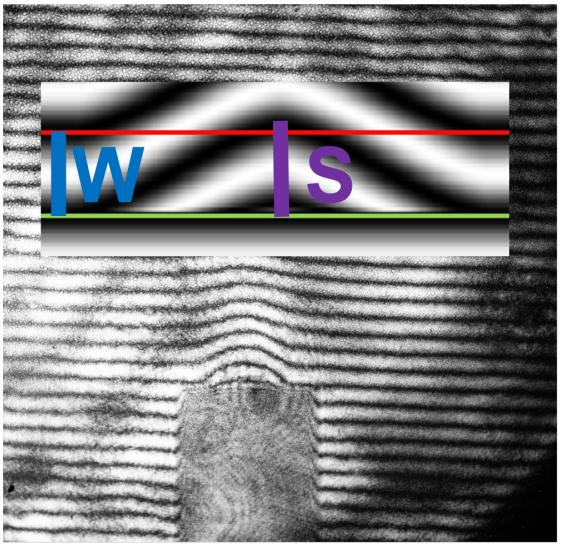

FIGURE 5.9: Mach-Zehnder interferogram of a neutral nitrogen gas jet with a 1000 psi backing pressure. The inset figure shows an idealized example of measuring the reference fringe width "W" and the perturbed fringe shift "S"

for various points along the central axis of the gas jet.

In order to achieve a comprehensive understanding this must be done for every point along the fringe as well as every fringe. It is this aspect of interferogram processing that has kept a lot of interferograms unprocessed and used mainly for qualitative purposes. In an effort to prevent this unfortunate fate for interferograms the Interferometry Processing and Analysis Suite (IPAs) was developed.

The IPA suite is composed of two main components: alphaDraw, a web app for interferogram fringe identification called and the alphaEngine, a processing and analysis engine. The IPA suite is capable of handling standard interferometry such as Mach-Zehnder interferograms as well as differential interferograms, like those produced with air-wedge shearing interferometers. As well, Talbot-Lau x-ray deflectometry spectroscopy is supported. Untested yet expected to work is the processing of VISAR data. The power of the IPA suite comes from the ability for a scientist to specify a variety of features in the interferogram that are then used by the engine for the processing.

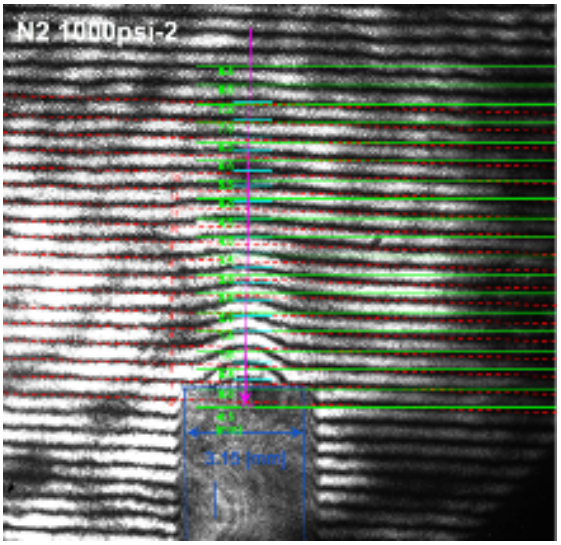

FIGURE 5.10: Example analysis of the central axial profile of a nitrogen gas jet with 1000 psi backing pressure.

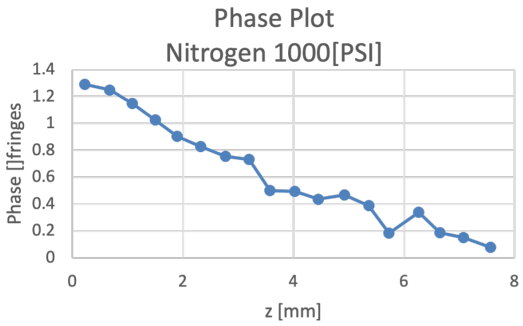

FIGURE 5.11: A plot showing the result of the by hand phase measurements performed in Fig. 5.10.

5.3.1 The alphaDraw Web App

The alphaDraw web app is the initialization tool for interferometry data for the IPA suite. Figure 5.12 is a screenshot of the alphaDraw front-end, a touch capable web app written primarily in HTML, JavaScript, and CSS. The back-end of alphaDraw is implemented with Node.js.

The core feature that alphaDraw provides is a graphical user interface that allows feature specification. Most importantly is the identification of reference fringes and

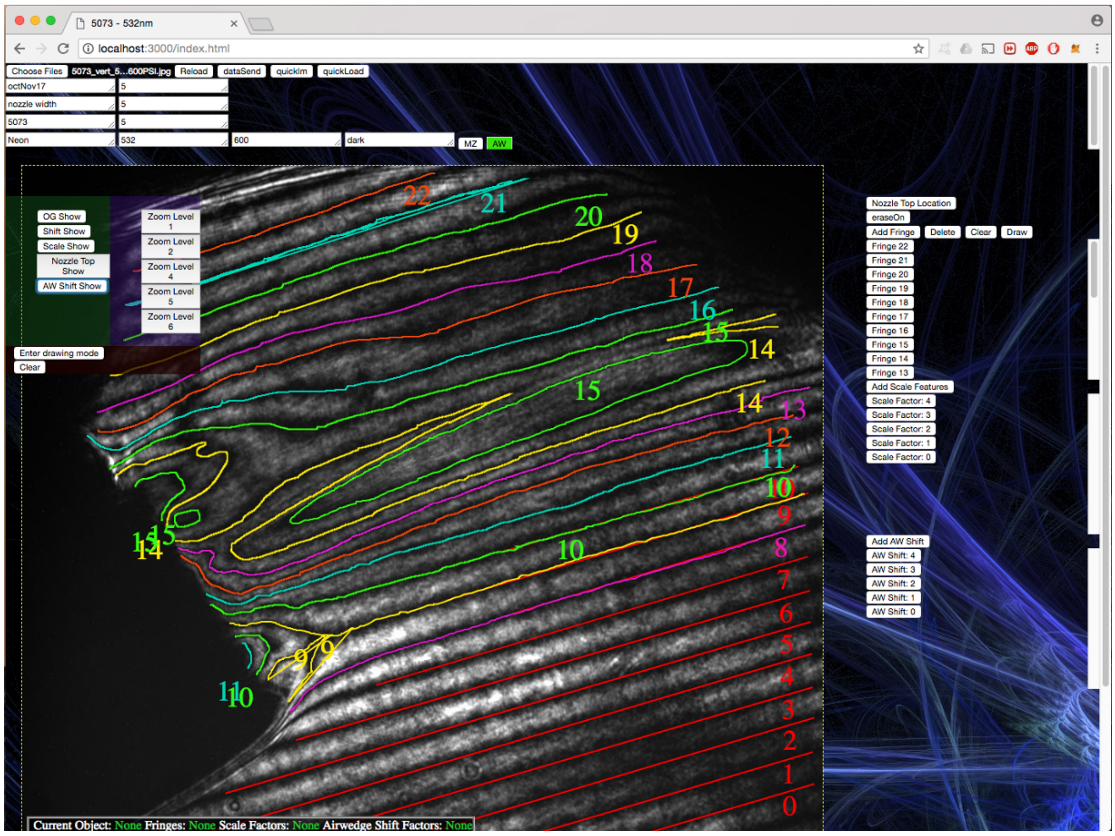

FIGURE 5.12: Screenshot of the alphaDraw web app. A photoionized gas jet is shown with the unperturbed(red lines) and perturbed(multi-colored lines) traced.

perturbed fringes. For interferograms that don't have enough reference fringes, the web app supports the use of reference interferograms. When reference images are used, alphaDraw provides a method to align the reference fringes to the interferogram being processed. There are as well a variety of auxiliary features that are either required and/or helpful to assist in the processing, some of these features include:

- Physical scale: Used for image to object space conversion
- Air-wedge shift: air-wedge specific property
- Object location: Used for orientation

5.3.2 The alphaEngine

The alphaEngine implements a plethora of routines that cover three main categories: processing, analysis, and error analysis. The routines and subroutines are written in python. To improve calculation time a variety of routines have been written utilizing what is known as "just in time" (JIT) compiling, which compiles the subroutine script to machine-code before running. This has a large accelerating effect vastly improving computation time. Further, parallel processing has been implemented at multiple levels within the alphaEngine framework. One of the several ways parallel processing is leveraged is in the processing of individual fringes for a single interferogram. For interferogram data sets, interferograms processing and analysis can be parallelized as well. Thus, by combining JIT and multiple level parallelization, speed increases can be as much as 300$times$ without.

5.3.2.1 Interferogram Processing

The processing routines implemented by the alphaEngine are composed of two main steps, initial and post-processing/analysis. The initial processing is responsible for extracting the phase map from the interferogram using the information provided by the alphaDraw web app. The post-processing is responsible for the extraction various data maps. The For the Mach-Zehnder interferometry the most important data maps are ones of refractive index and atomic number density. For the air-wedge interferometry the data maps of interest are the refractive index, areal electron density, and the electron number density.

An important capability of the alphaEngine is the fringe placement correction routines. Since the fringes are traced by the user this naturally allows for subjectivity of the true fringe placement between users, even between two separate traces conducted by the same user. As a way around this dilemma a sophisticated correction routine has been developed to make an interferogram trace objective. The correction routine steps

through each fringe trace point by point. For each point the algorithm takes a line out that is perpendicular to the fringe. The line out is then fit with a Gaussian and the center of the Gaussian is chosen as the corrected point. The correction routine allows for more accurate trace placement and objective reproducible fringe traces between different users and/or different traces of the same user.

Figure 5.13 shows the result of the phase map extracted from the Mach-Zehnder interferogram shown in Fig. 5.9. The complete phase map is produced by interpolating between all of the phase shift measurements calculated along the perturbed fringes. The result of Fig. 5.13 shows the true power of the IPA suite. Phase maps can be extracted with high level detail, down to the pixel step size. This high resolution capability allows for more accurate averaging/smoothing and interpolation. Radial and axial profiles for this specific interferogram are shown later in the chapter in Sec:5.4.1. The results calculated by hand in Fig. 5.11 compare very well with the central axial profile for the 1000 psi case in Fig. 5.25.

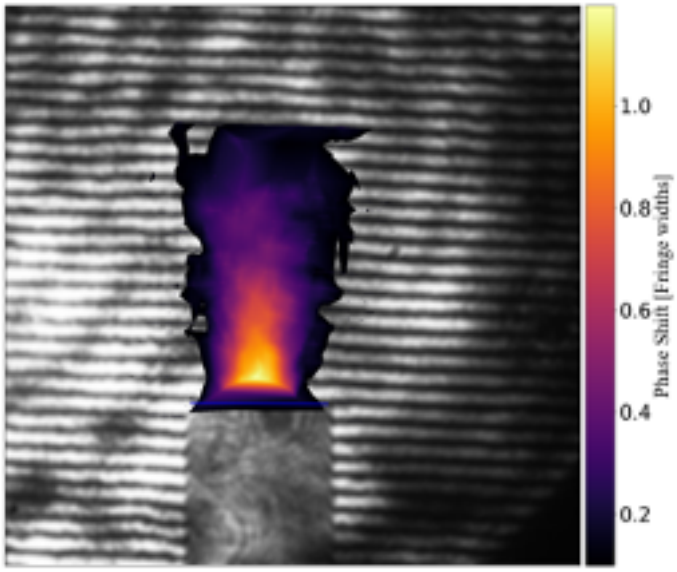

FIGURE 5.13: Extracted phase map of the interferogram in Fig. 5.9.

The phase map extraction for air-wedge interferometry follows a similar initial set of step as the Mach-Zehnder however this only produces the pre/initial phase map.

There is a second step required for the extraction of the true phase map of an air-wedge interferogram. Figure 5.14 shows the initial phase map that is calculated phase map extraction process for air-wedge interferograms. The steps to produce this initial phase map are the exact same as for the Mach-Zehnder phase map extraction.

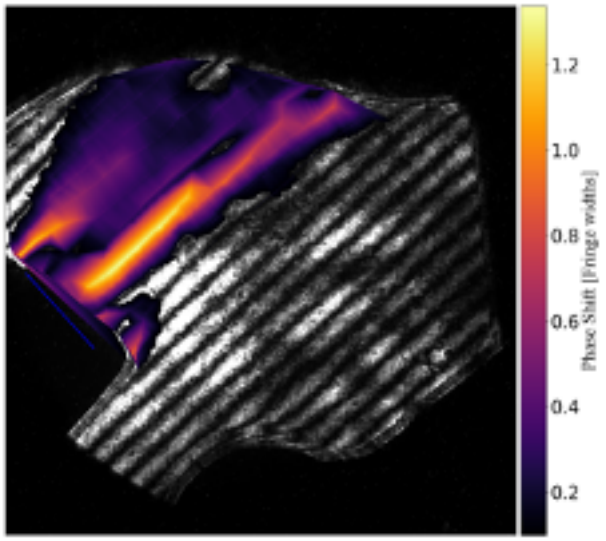

FIGURE 5.14: Example of the initial phase map extracted from an air-wedge interferogram.

The next step in the phase map extraction process for air-wedge interferograms requires measuring the air-wedge characteristic shift. Air-wedge interferometers get their name because two glass interfaces are placed close together with one side offset by a small displacement. The air-wedge produces two separate images that are slightly offset from each other. These two images constructively and deconstructively interfere, producing what is known as a differential interferogram. This displacement manifests two images that are slightly shifted from each other. The shift of these two images manifests in the interferogram as kind of "double image" effect. Figure 5.15 shows an example interferogram reference image with an inset. Once this air-wedge characteristic shift has been measured the true phase map can be extracted.

The next step required to extract the true phase map of an air-wedge interferogram requires integration of line outs from the initial phase map that are perpendicular to

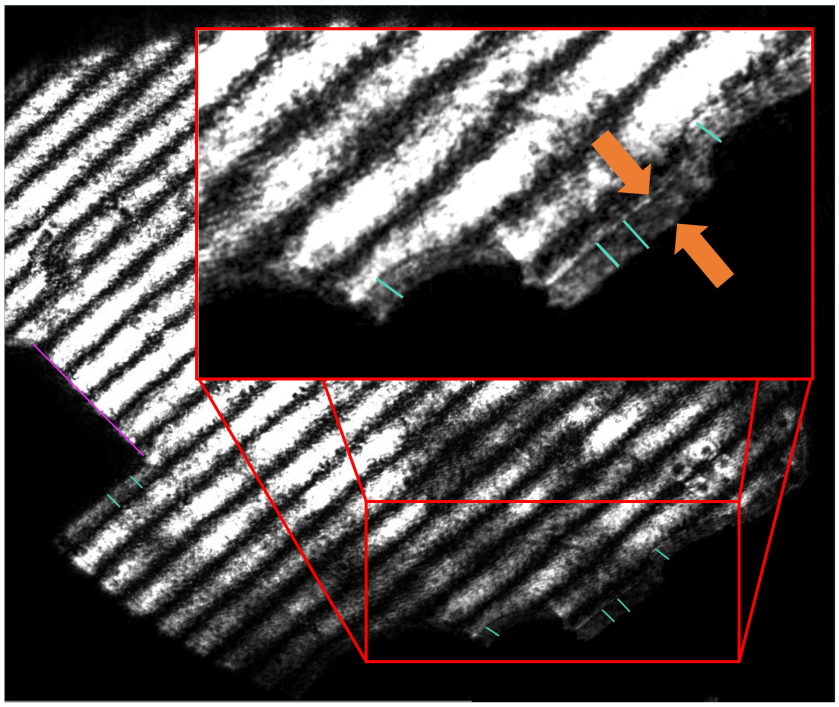

FIGURE 5.15: Example of a reference air-wedge interferogram. The orange arrows denote the air-wedge shift found in air-wedge interferograms. The teal lines represent the measurements of the air-wedge shift values, made with the alphaDraw web app.

the fringes. The line outs must have at least one end in a region of zero phase shift. As well, the line outs must be discretized by the characteristic air-wedge shift value found in Fig. 5.15. Starting on the zero phase shift end of the line out, the phase shift is accumulated from one point to the next point, i.e. each point is summed with all the previous points before it. Once this has been for each line out, the result is a collection of lines parallel to the reference fringe lines that are the true phase shift values for the locations on the interferogram, separated by an interval of the characteristic air-wedge shift. Figure 5.16 shows an illustration of the locations of each of the phase shift lines, starting from the point of zero phase shift. Similar to the Mach-Zehnder phase map extraction and the initial phase map extraction, interpolation is used to provide the remaining values. Figure 5.17 shows the true phase map extracted from the 532 nm air-wedge interferogram of a photoionized supersonic gas jet with 600 psi backing pressure.

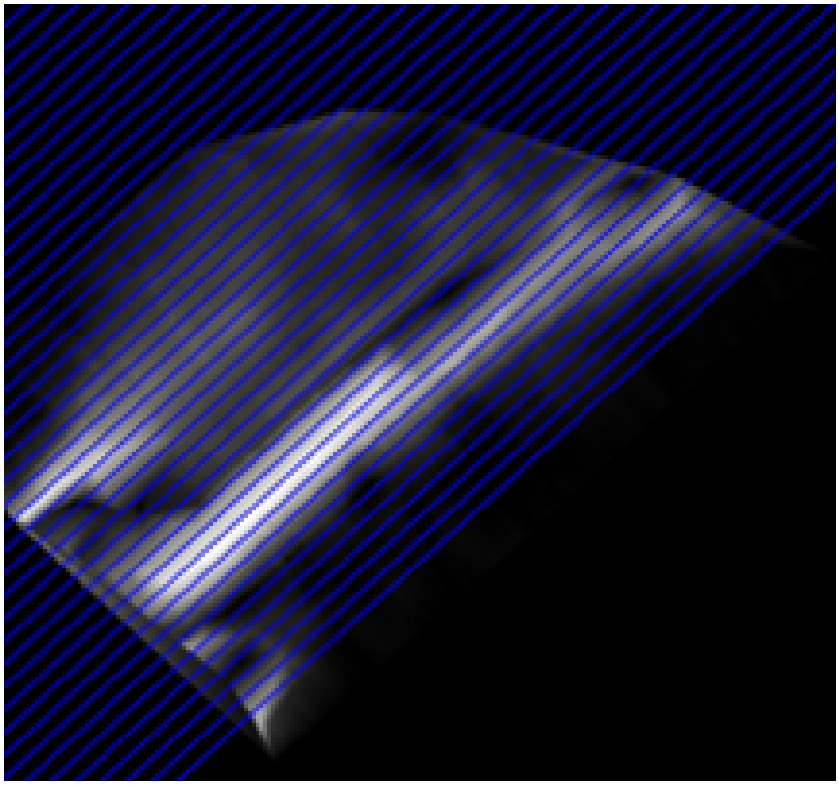

FIGURE 5.16: An example intermediate step that is required to extract the true phase map of an air-wedge interferogram from the initial phase map of Fig. 5.15

5.3.2.2 Phase Map Post-processing and Analysis

The alphaEngine has a full complement of tools to utilize for further post-processing and analysis of phase maps. Of the tools available, the Abel inversion capability is one of the most important. If the object being interrogated with interferometry has cylindrical and/or spherical symmetry, the alphaEngine can determine the axis of symmetry and employ Abel inversion methods to unfold the phase map from image space into a data map in object space.

The Abel inversion capability was of great importance for both the characterization of the neutral gas jets and the photoionized gas jets. For the Mach-Zehnder interferograms of the neutral gas jets, the Abel inversion routines were utilized to unfold phase maps into refractive index maps of the supersonic gas jet, implementing Eq. 5.5. Similarly, for

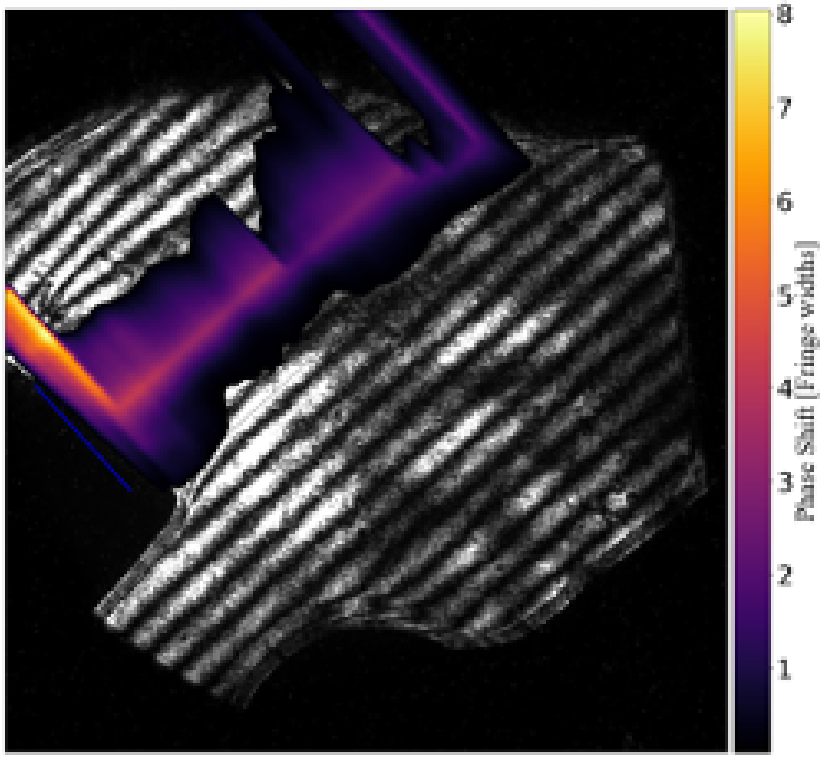

FIGURE 5.17: The true phase map extracted from a 532 nm air-wedge interferogram of a photoionized neon gas jet with 600 PSI backing pressure.

the air-wedge interferograms, the Abel inversion routines are used to unfold the phase maps, almost directly, straight to electron number density maps employing Eq. 5.11. Either case, neutral or photoionized, the alphaEngine has the ability to implement an Abel inversion in a variety of ways. Typically, if the cylindrical symmetry of the gas jet is robust the left and right side are averaged first and then the Abel inversion is taken of the averaged radial profile. For cases where the symmetry in the interferogram is not robust the Abel inversion can be applied to the left and right side of the jet individually.

Now, before everyone gets alarmed at the idea of using an Abel inversion on a non cylindrically symmetric object... hear me out. For the case of the photoionized supersonic gas jets, the line of sight for the vertical two-color air-wedge interferometers can have contamination. The contamination occurs from the load hardware ablating from the x-ray flux of the z-pinch. The ablation of the load hardware produces a free electron

cloud above and below the gas jet on the opposite side from the z-pinch. Thus, in a situation like this the object does have cylindrical symmetry, however on one side it is augmented with noise, therefore for the uncontaminated side we are authorized to use the Abel inversion. This effect can be seen in Fig. 8.2, where the right side of the jet is much more well-behaved functionally than the left side.

5.3.2.3 Data Map Error Analysis

The alphaEngine calculates three separate phase maps per interferogram. This is made possible by calculating the mean and standard deviation of the measured physical scale factors performed in the alphaDraw web app. Standard practice is to measure the scale factor a minimum of five times per interferogram. Further, for each set of interferograms that have the same scale factor, a superset of scale factor measurements is utilized to calculate a more precise mean and standard deviation value. Once the mean and standard deviation has been calculated, one phase map is calculated with the mean scale factor value, a second is calculated from the mean plus one standard deviation, and the third phase map is calculated using the mean minus one standard deviation. These phase maps are then individually processed and then used to together at the end as a method to estimate uncertainty in the results.

Now, for the case of the air-wedge interferometry there is another feature involved that is utilized for the error analysis which is the air-wedge shift value. This value is as well measured a minimum of five times per interferogram. For air-wedge interferograms of the same wavelength and air-wedge setting, a superset of air-wedge shift measurements is collated from which a more precise mean and standard deviation are also calculated from. Similar to the scale factor, the mean, the mean plus one standard deviation, and the mean minus one standard deviation are used for each of the three initial phase maps. This provides nine individual air-wedge phase maps that are processed independently and then utilized to provide a method to estimate the uncertainty.

5.4 Nozzle Designs

Supersonic gas jets have several desirable features for our application. First of which is their collimated behavior. Seeing as the goal was to position the gas jet as close as possible to the z-pinch, between the mega volt potential of the anode and cathode; it was very important that the gas jet did not expand and interfere with the safe operation of Zebra. Second, the plasmas that we are trying to reproduce are uniform in both density and ionization, similar to the gas cell where the goal is to produce a hydro-unperturbed photoionized plasma. Thus, supersonic gas jets are an excellent choice as a defining feature is their uniform radial density profiles; unlike sonic or subsonic density profiles that are parabolic in nature. The differences in jet profile can be compared in Fig. 5.18 & 5.19. From a data analysis perspective it was important that the gas jets be as uniform as possible in order for robust axial symmetry. The extraction of spatial density profiles from interferometry of both the neutral and photoionized gas jets relies on Abel inversions, which in turn is dependent on axial symmetry(see Sec:5.6). One may suggest, "Why not use a rectangular jet? As a rectangle is a much simpler geometry to calculate and extract density from." Indeed, a slab would be much easier to work with, however, this goes against feature number ***one***: The gas jet should be collimated tightly so as to not expand in a precarious manner that may interfere with the current flow through the z-pinch and/or the return current cage.

With the matter settled on the type of gas jet, we turned to the previous effort of gas jet characterization done by Malka and Semushin. [44, 65] Their work focused on determining optimized conical nozzle parameters for the production of supersonic gas jets, see Table 5.2. The gas jet experiments utilized two different nozzles specified by the first two rows; Nozzle1 and Nozzle2 are the designations for the first and second row, respectively. Based on these specifications, 3D models were built in Blender[8] a 3D design and rendering software. Figure 5.20 and 5.21 show the 3D rendered images of Nozzle1 and Nozzle2, with the relevant dimensions displayed. Nozzle1 has a semicircle

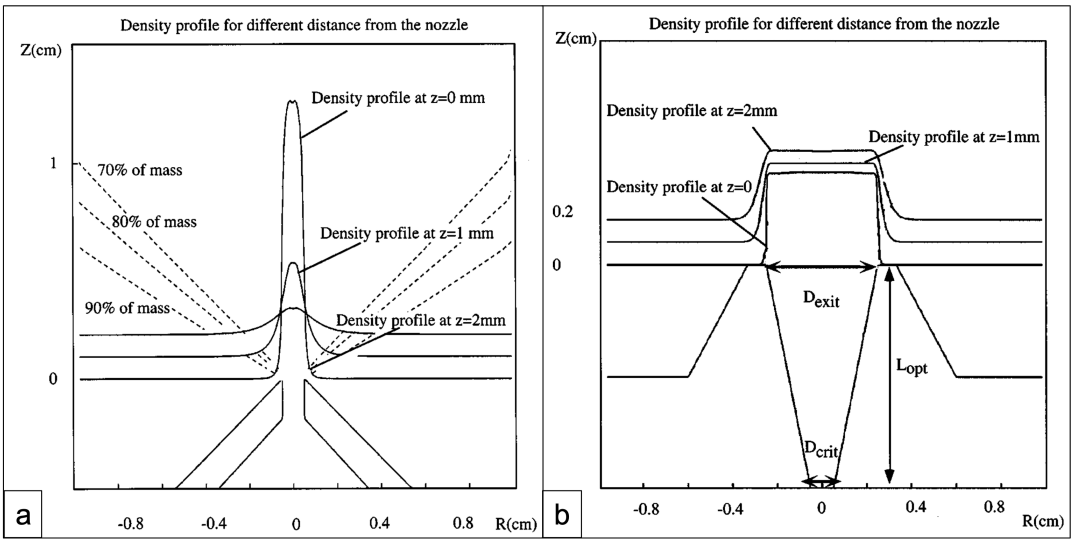

FIGURE 5.18: **a.** Solid lines: density profiles for subsonic nozzle, z=0, 1, and 2 mm. Dashed line: percentage of mass in the flow. **b.** Density profiles for conical nozzle, z= 0, 1, and 2 mm. [65]

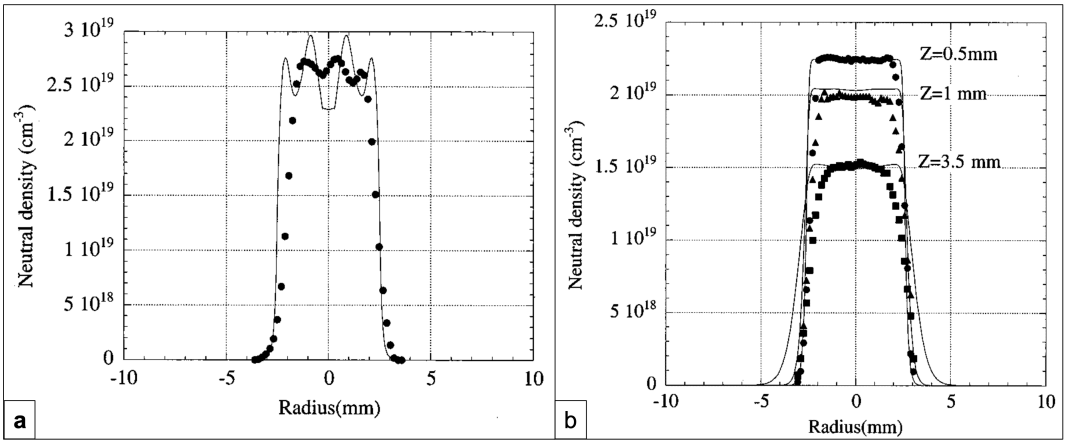

FIGURE 5.19: **a.** Experimental and simulated data for parabolic nozzle for 100 bar backing pressure. Dotted line: experiments. Solid line: simulations. **b.** Experimental and numerical data for conical nozzle for sections with different Z and for 100 bar backing pressure. Solid line: simulations. Experiments: circles (z=0.5 mm), triangles (z=1 mm), squares (z=3.5 mm). [65]

$D_{crit}(mm)$	$D_{exit}(mm)$	$I_{opt}(mm)$	M_{exit}	$n_{exit}(cm^{-3})$
1	2	6	3.5	18×10^{19}
1	3	7	4.75	7.5×10^{19}
1	5	10	7	2.7×10^{19}
1	10	15	10	0.75×10^{19}
0.5	1	4	3.3	16×10^{19}
0.5	2	5	5.5	4.5×10^{19}
0.5	3	5	6.2	2.1×10^{19}
0.5	5	7	9.5	0.7×10^{19}
0.5	10	15	14.5	0.2×10^{19}

TABLE 5.1: Optimized nozzles parameters. D_{crit}, D_{exit}, and L_{opt} are defined in Fig. 6. The Mach number and the density at 0.5 mm from the nozzle exit are M_{exit} and $_{exit}$ respectively. [65]

parapet around the nozzle exit. The goal of the parapet was to block/inhibit radiation of the pinch from reaching the inner regions of the nozzle, mitigating ablation and other adverse effects. How successful the parapet was is up to debate. One unfortunate consequence of the parapet was the ablation of the parapet which caused a dense plasma region right near the tip of the nozzle, which introduced complexities in the processing and analysis of the air-wedge interferometry of photoionized gas jet, (see Sec: 5.29). In the end, Nozzle2 turned out to be a better solution. The gas jets produced from Nozzle2 were better collimated than those of Nozzle1, this can be seen in Fig. 5.29 as well. The nozzles were printed by Shapeways, an online 3D printing company.

5.4.1 Characterization of neutral gas jets

Gas jet performance and characterization is commonly done with Mach-Zehnder interferometry. [4, 44, 65, 63] Shadowgraphy[27, 71, 69, 70, 63] and Schlieren[27, 73] laser imaging are two other methods that are as utilized for assessing the properties of gas jets. For the photoionized gas jet experiments, Mach-Zehnder interferometry at 266 and 213 nm was employed to characterize the physical gas jet profile and the radial atomic/molecular density profiles of the gas jets.

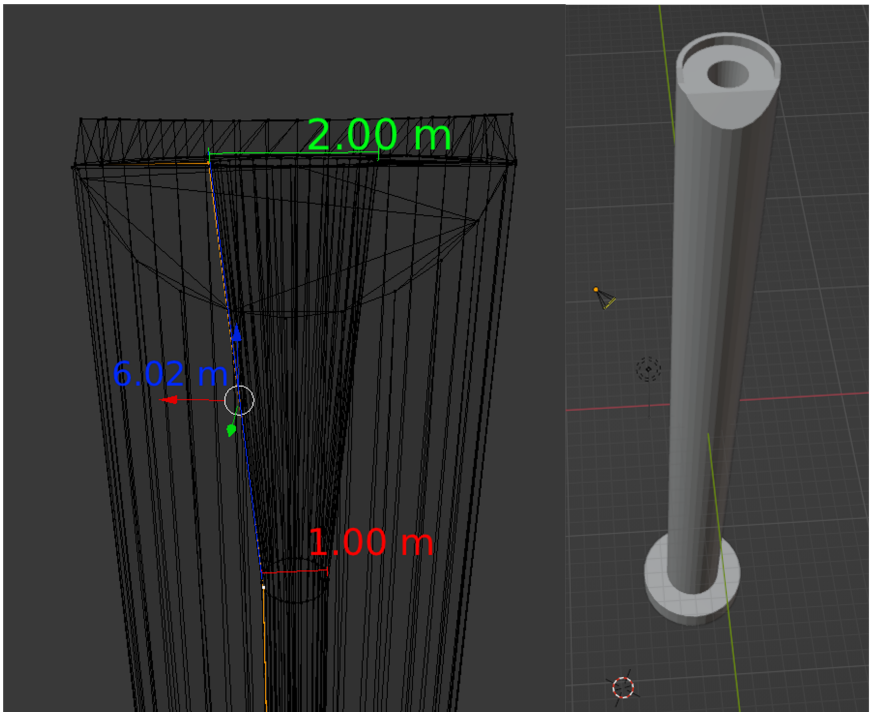

FIGURE 5.20: First nozzle used for the majority of experiments, 2017-2020. The parameter of this nozzle follow the first line in 5.2.

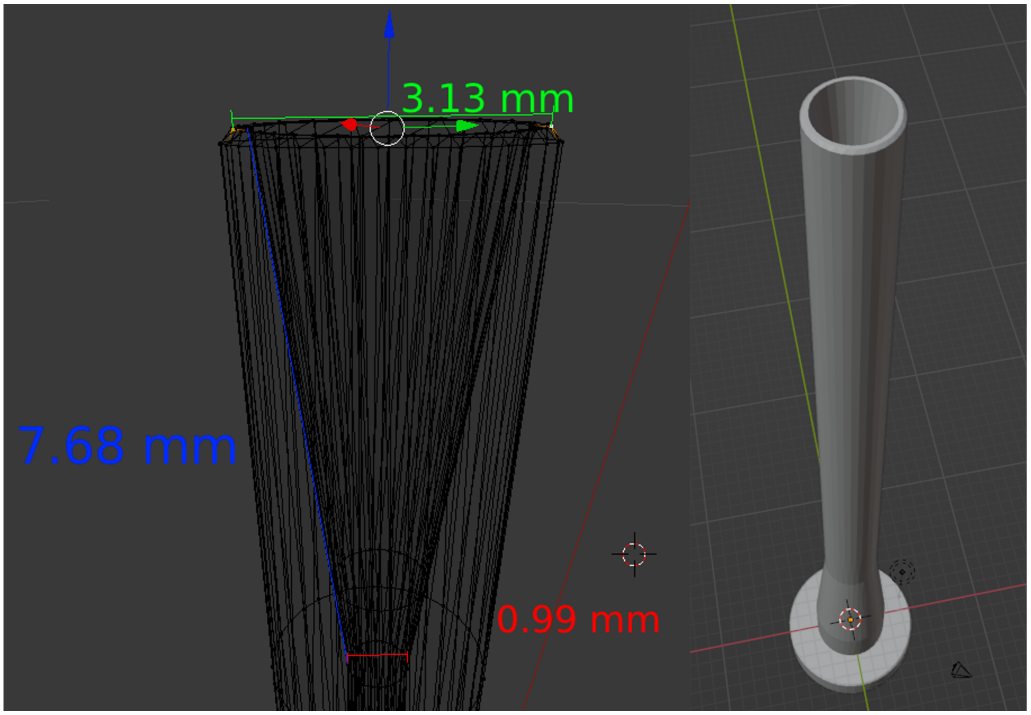

FIGURE 5.21: The second nozzle used for the experiments in 2020 and after. The parameter of this nozzle follow the second line in 5.2.

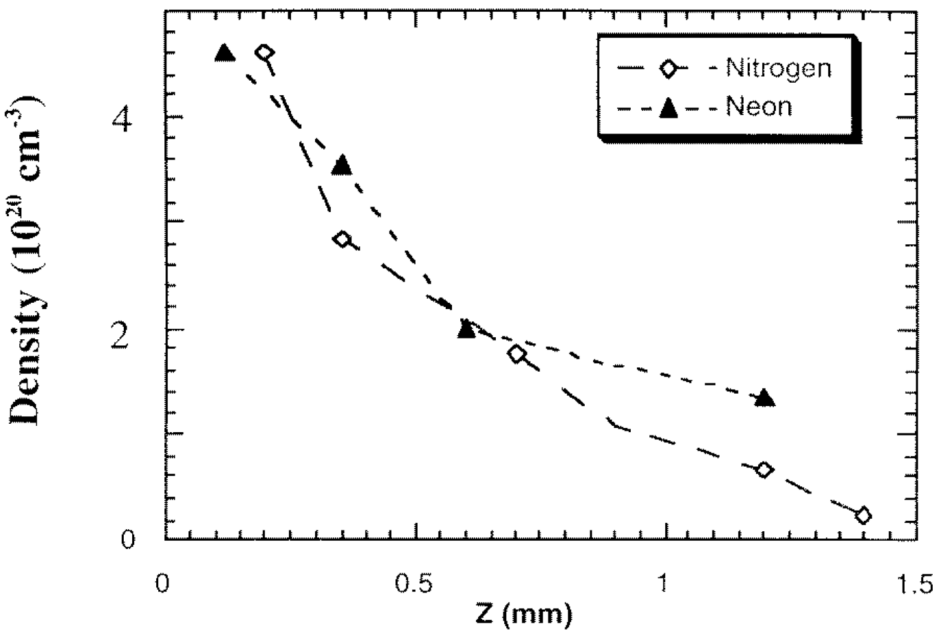

FIGURE 5.22: "The axial density of the N_2 and Ne gas jets under the same conditions (for a 1mm diameter nozzle at a gas-reservoir pressure of 5×10^4 Torr)"[4] The terminology "gas-reservoir pressure" is equivalent to "backing pressure" which is used in this text.
1 Torr $\cong$ 0.01934 psi; thus, 5×10^4 Torr $\approx$ 966.8 psi.

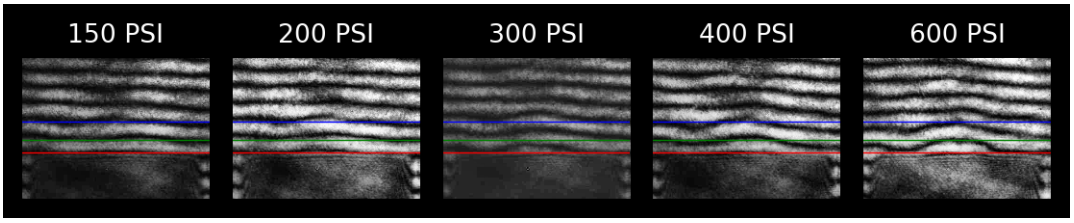

FIGURE 5.23: Mach-Zehnder interferometry of neutral nitrogen gas jets, with backing pressures (left to right): 150, 200, 300, 400, 600 psi.

5.4.1.1 Room 102 studies

Independent assessment of the gas jets used in these experiments was performed in an adjacent laser lab, using a 266 nm Mach-Zehnder interferometer configured to probe gas jets in a small vacuum chamber. A variety of gas jet surveys for the nozzles that were used in the main experiments were conducted. Some of the surveys include:

- Gas jet behavior at different backing pressures
- Gas jet evolution
- Refractive-index sensitivity of different gases(nitrogen, neon, and argon)

5.4.1.1.1 Effect of backing pressure

For a given nozzle type, the density of the gas jet is determined by the backing pressure of the nozzle. The range of pressures investigated for the photoionization experiments on Zebra are in the range of 200-1000 psi. Figure 5.23 shows a series of interferograms taken of nitrogen gas jets at different backing pressures using Nozzle2, ranging from 150-600 psi. As the pressure increases the jet produced becomes longer; which can be seen by the increasing distance at which fringes are perturbed from the nozzle top. As well, the density of gas jets increases which can be inferred by the degree of perturbation of a single light or dark fringe.

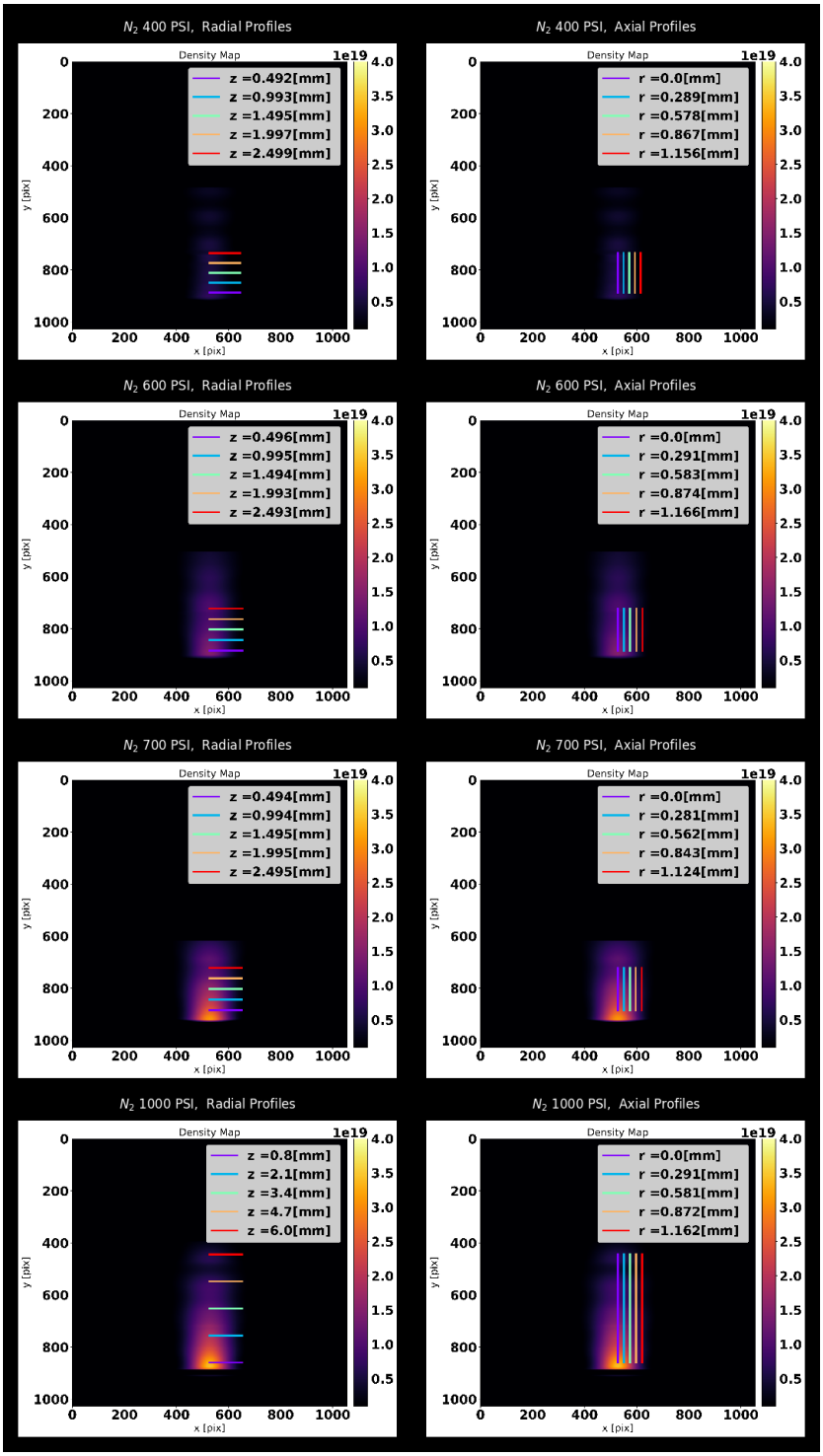

FIGURE 5.24: Atomic density maps extracted from Mach-Zehnder interferometry of neutral nitrogen gas jets at backing pressures: 400, 600, 700, 1000 psi

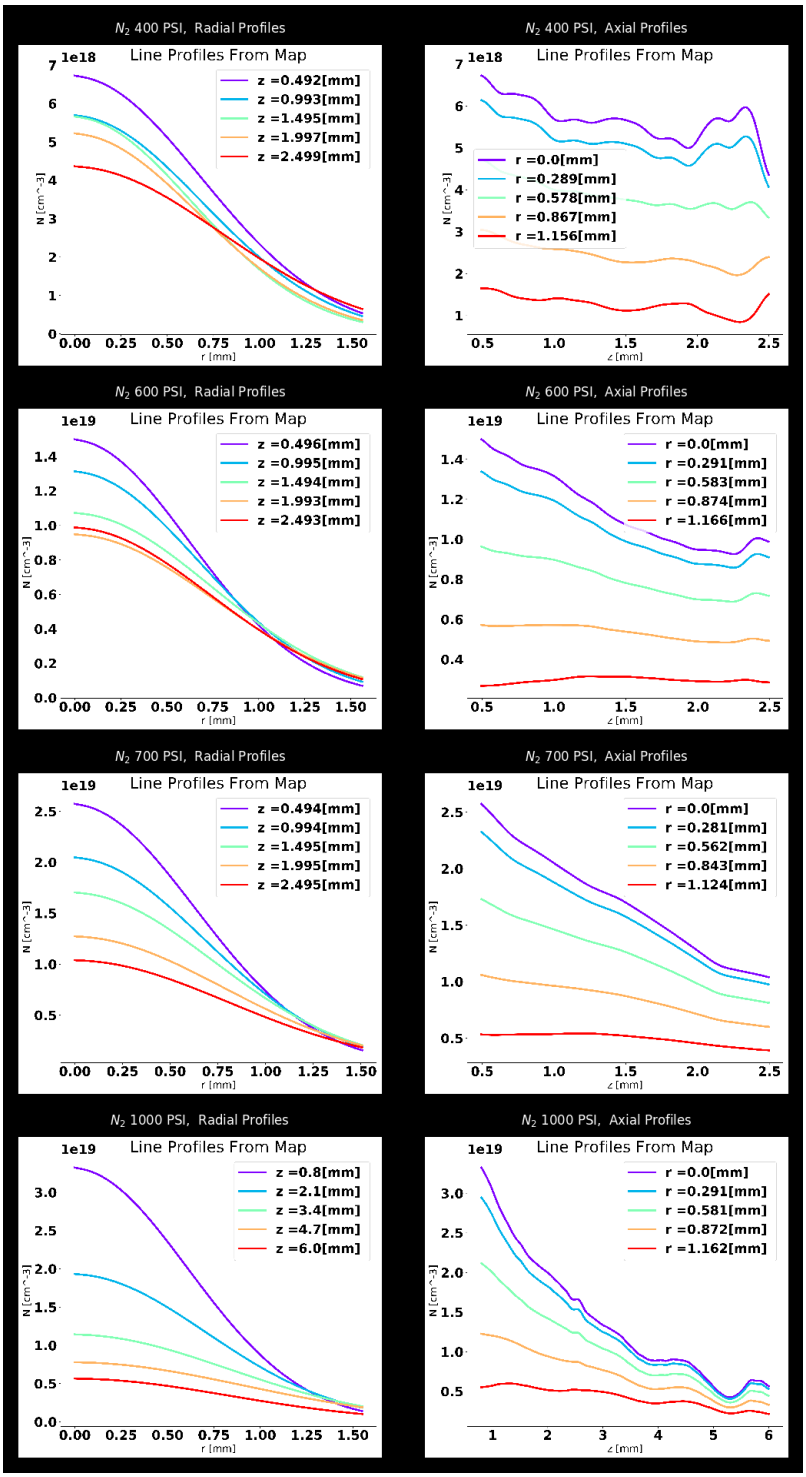

FIGURE 5.25: Radial and Axial atomic density profiles extracted from the atomic density maps shown in Fig. 5.24, for neutral nitrogen gas jets at backing pressures: 400, 600, 700, 1000 psi

Gas type	$n(\lambda = 266nm)$	$(n_{266} - 1)$	$n(\lambda = 213nm)$	$(n_{213nm} - 1)$
Nitrogen(N_2)	1.00031837	0.00031837	1.00033462	0.00033462
Argon	1.00030064	0.00030064	1.00031595	0.00031595
Hydrogen(H_2)	1.00015229	0.00015229	1.00016413	0.00016413
Neon	1.000068304	0.000068304	1.000070024	0.000070024

TABLE 5.2: Tabulated values for experimentally determined values of the refractive index in the ultraviolet for:[5] nitrogen(N_2), argon, hydrogen(H_2), and neon.

5.4.1.1.2 Gas jet evolution

Timing of the gas jet was also a critical parameter to investigate. Figure 5.26 shows the evolution of a gas jet at 600 psi. The jet takes ∼0.8 ms to reach a quasi steady state, which lasts on the order of ∼3.4 ms, followed by ∼0.6 ms of dissipation/break up.

5.4.1.1.3 Refractive index sensitivity of Mach-Zehnder interferometry

The phase shift resulting from a change in refractive index for a Mach-Zehnder interferogram is inversely proportional to the wavelength of the probe laser and proportional to the integrated index of refraction of the medium over the length of the medium. Figure 5.27 shows a comparison between nitrogen and neon gas jets of the same pressures and jet evolution. From the analysis of the nitrogen and neon gas jet we can see that while the extracted phase shifts are different the extracted densities are similar. In particular, it has been investigated before that nitrogen and neon gas jets produced with the same nozzle and pressure result in nominally identical jet densities. [4] This is an important connection that we utilized for the neon photoionization experiments with Zebra. As is evident in Fig. 5.27 the refractive index of neon is much less than that of nitrogen and argon. When the refractive index is as weak as it is for neon, characterization of low density jets with Mach-Zehnder interferometry is challenging. To circumvent the challenge, nitrogen was used for the characterization of the gas jets when it was two difficult with neon.

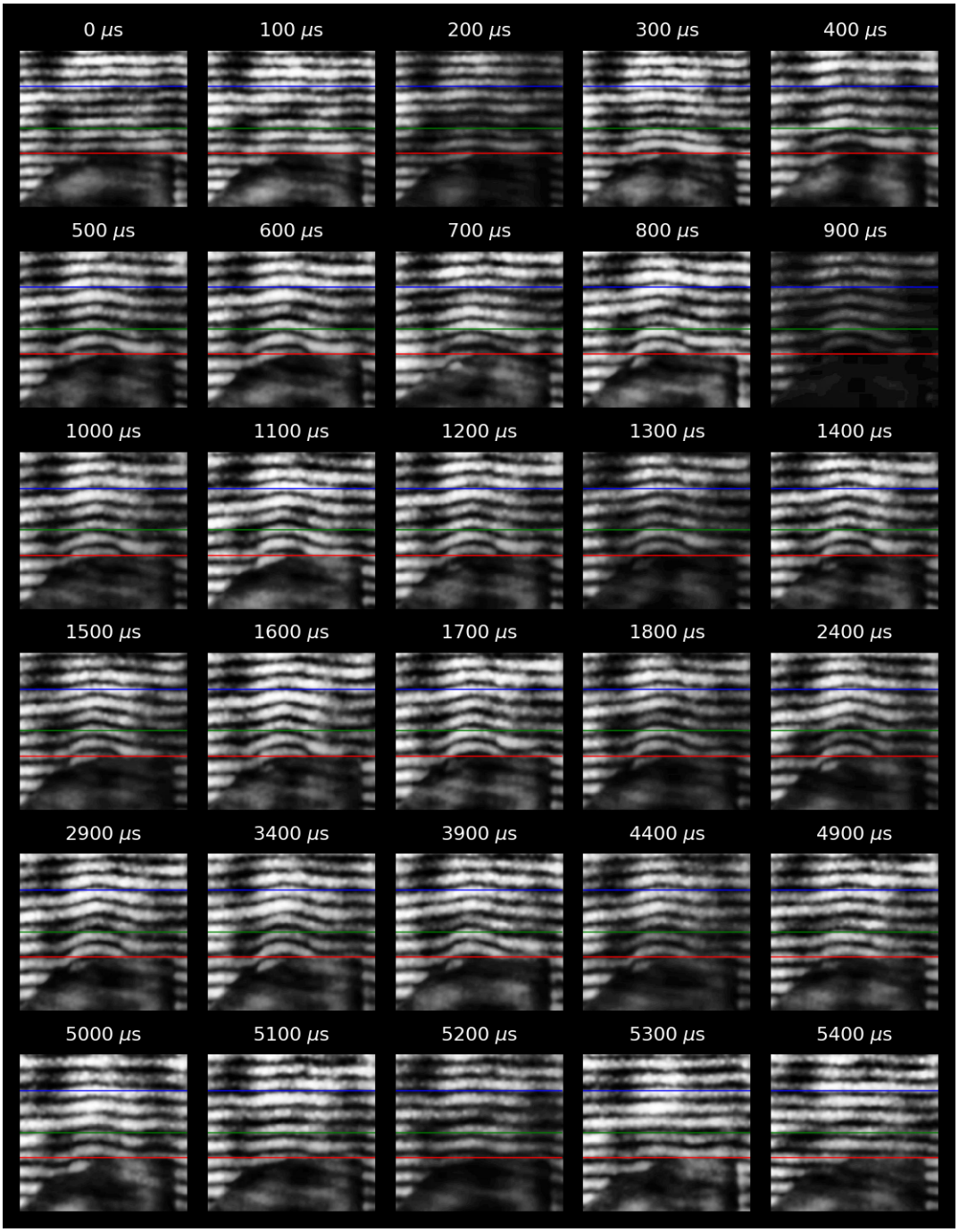

FIGURE 5.26: Time evolution of a neutral nitrogen gas jets with backing pressure of 600 psi.

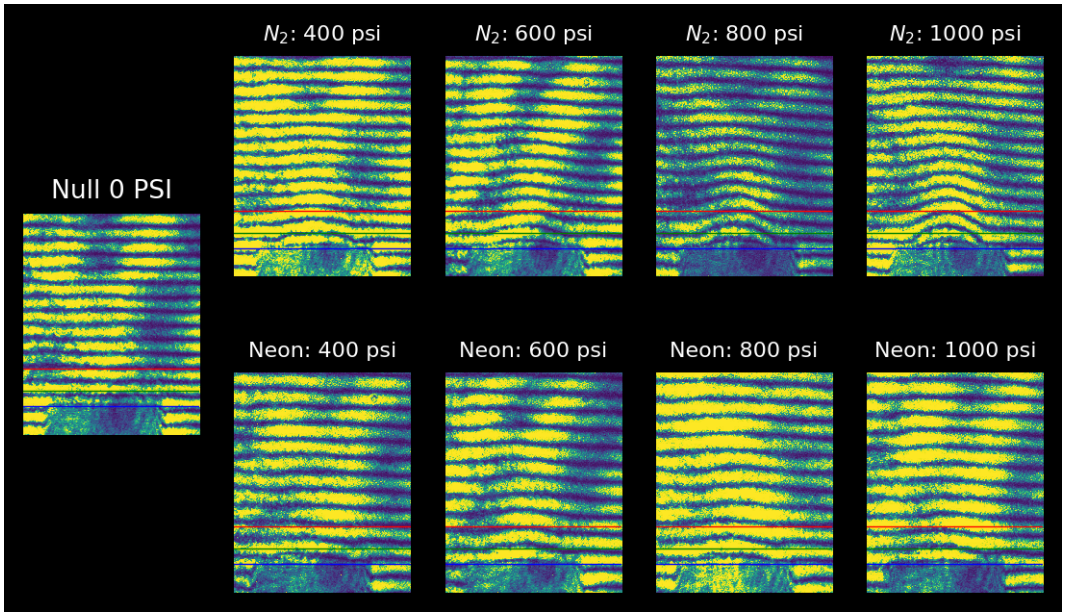

FIGURE 5.27: Neutral nitrogen vs neon gas jets

5.4.1.2 Neutral Gas Jet Characterization in Zebra

Mach-Zehnder characterization of the neutral gas jets produced within the Zebra chamber presented a greater challenge than when conducted in room 102, the adjacent laser lab. One of the first obvious added complexities was the extra windows required for the Zebra setup. The vertical beam path through the Zebra chamber incorporates the following: 1× 2" Dia. vertical vacuum window port, 2× vertical vacuum window port protective 1"x1" quartz slide, 1× protective quartz 1" diameter quartz disc, 1× side vacuum window port, and 1× protective 2" diameter quartz disc. Compared to the vacuum chamber in the adjacent laser lab, there are four more windows the laser diagnostic must pass through when working in the Zebra chamber. These extra windows each represent another location that can perturb the laser light causing decoherence. Another factor that makes Mach-Zehnder characterization more difficult in the Zebra chamber was the increase distance the laser needs to propagate. This increased distance increases the time that the laser pulse traverses through the air, which also causes decoherence. The quality of the undisturbed fringe lines is clearly evident between the Mach-Zehnder

interferometry that took place in the adjacent laser lab and in Zebra.

5.4.1.2.1 Nozzle variability comparison

Each shot with Zebra utterly and completely destroys each nozzle used to produce the gas jets. Luckily, we were able to order large quantities of 3D printed nozzles, with one major drawback. Each nozzle while fabricated to be identical, all have minor variations which lead to slight changes in performance, most of the time unnoticeable/tolerable. Due to the inherent variability, it was important that we characterize the gas jets from each nozzle to be sure that the jets were adequate. However, it would have been too time-consuming to characterize each nozzle in room 102, the adjacent laser lab. Instead, prior to each Zebra shot, the neutral gas jets produced by each nozzle were characterized in the Zebra chamber. The characterization process involves taking multiple reference Mach-Zehnder interferograms. If the planned shot is with neon, there are two sets of reference images taken. The first set is with a gas that has a strong index of refraction like nitrogen or Argon, see Fig: 5.28. Once there is satisfactory understanding that the nozzle is performing nominally identical from shot to shot, we proceed with the rest of the shot preparation. Based on these characterization efforts we suggest that the gas jets produced by the nozzle before the Zebra shot are nominally identical to the gas jet produced and probed during the Zebra shot.

5.4.1.2.2 Nozzle type comparison

Lastly, the gas jets produced by Nozzle1 and Nozzle2 were studied and found to have several contrasting characteristics. Figure 5.29 shows a comparison extracted phase maps from the two different nozzles, detailing the two main characteristic differences. The first being that Nozzle1 has the parapet that ablates and causes plastic plasma to form near the tip of the nozzle. The presence and absence of this ablated plasma is located by the red box in Fig. 5.29. This extra ablated nozzle plasma causes irrecoverable complication to the phase shift measured by interferometry, as it is integrated into the

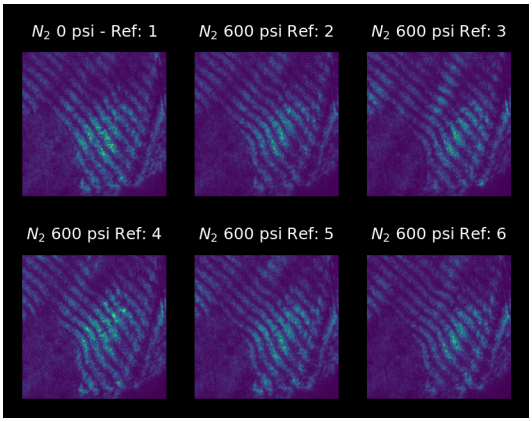

FIGURE 5.28: Example of nozzle characterization with 600psi nitrogen gas jets before the zebra shot.

measurement in an inconsistent and unpredictable fashion. The second characteristic is the collimation of the gas jet. Nozzle2 produces a much more collimated gas jet on average than that of the one produced by Nozzle1, denoted by the green arrows in Fig. 5.29.

5.4.2 Gas Jet Manifold

There were two main hurdles that had to be overcome in order to produce astrophysically relevant photoionized plasmas with a Zebra. The first obstacle was proximity of the photoionization target with the radiation source. Since Zebra produces less radiation flux than Z, the photoionization target would need to be much closer to the radiation source. The second obstacle was target containment and positioning. Since the target needs to be close to the Z-pinch a bulky object such as a gas cell would not be very feasible and or practical. Using a supersonic gas jet as a photoionization medium turned out be the perfect target that solved both hurdles.

The gas jet platform developed for Zebra provides controlled systematic delivery of gas jets within the Zebra chamber near the z-pinch radiation source. The gas jet platform consists of an automated 3-valve manifold system integrated into the Zebra diagnostic triggering system.

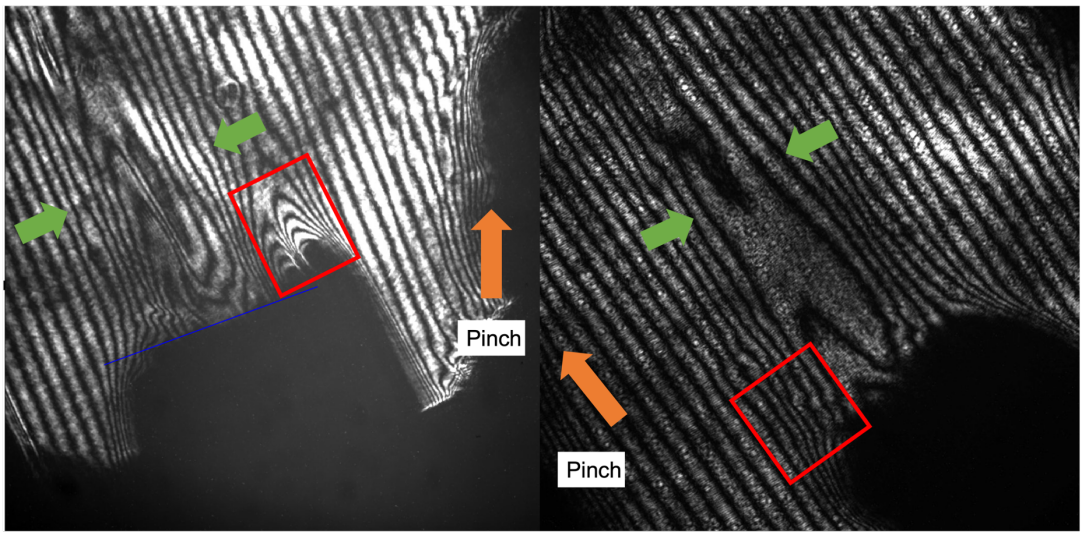

FIGURE 5.29: Left interferogram is of a photoionized gas jet using nozzle 1. Right interferogram is of a photoionized gas jet using nozzle 2. Red box shows the presence of nozzle ablation in the left image and the absence of this ablation in the right image. The green arrows show the wider jet produced with nozzle 1 and the more collimated nature of the jet produced with nozzle 2.

The Zebra chamber is 60 cm in diameter with the cathode co-axially located in the center of the anode plate. Vacuum chambers, like Zebra's, are designed not to allow gas to come in, as well, nor were they designed to be operating with volumes of gas spontaneously appearing inside out of thin "Vacuum". To solve this problem an automated 3-valve gas manifold was designed. The manifold consists of two general purpose solenoid valves and one high-speed high-vacuum miniature pulse valve, aka "Fast Valve". The main purpose of the manifold is to keep the internal gas fill line at low pressure while not in use, so that small micro leaks don't compromise the vacuum and to keep the cryo-pump from wearing out too quickly. The manifold operation first charges the gas fill line with valve #1. Valve #2 produces a pulse of gas that flows through the supersonic nozzle. Subsequently, after the gas jet has been produced and valve #2 and valve #1 close, valve #3 opens the manifold up to atmosphere, outside of the chamber, to relieve the pressure in the gas fill line. Figure 5.30 shows a cartoon of the gas fill manifold and the basic flow of operation.

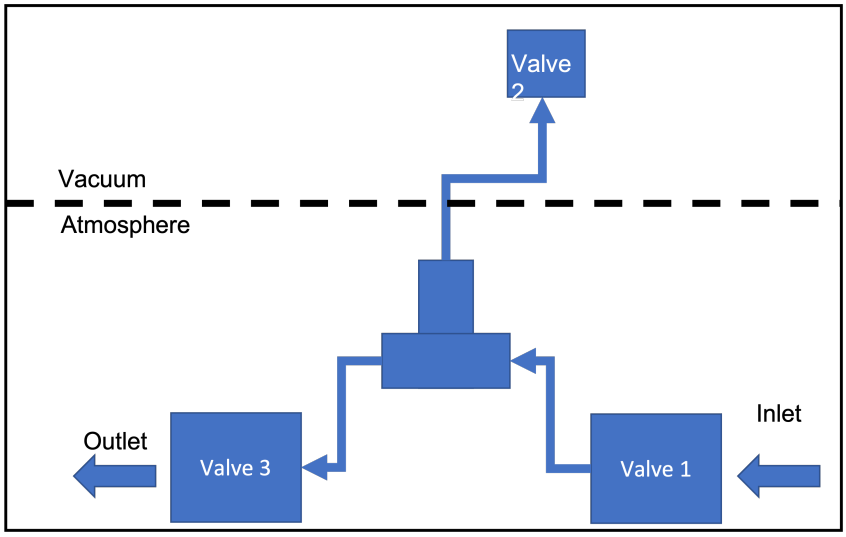

FIGURE 5.30: A schematic depicting the 3-valve manifold system for the gas jet platform

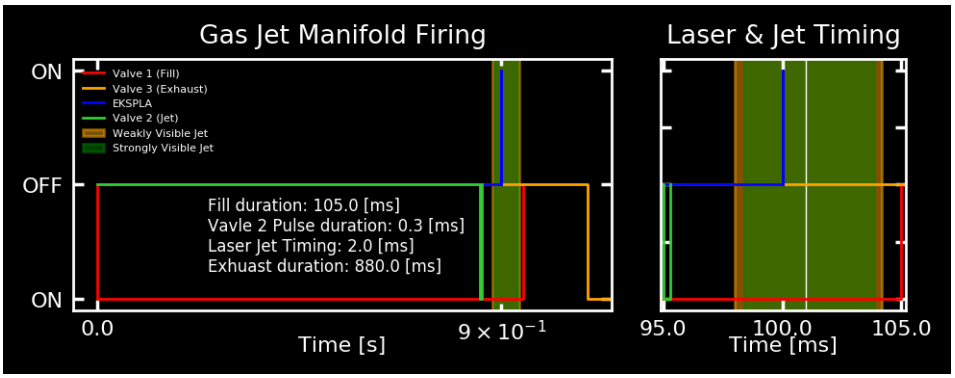

FIGURE 5.31: Firing sequence of the gas jet manifold system for the photoionized gas jet platform on Zebra. Left plot: Shows the entire sequence with an inverted log scale for the time axis to accentuate the early timing of the system. Right plot: Expanded view of the gas jet duration and laser diagnostic timing.

The gas jet platform has several key features. The first being the ionization medium, the gas jet, can be placed in close proximity to the Z-pinch, on the order of 5-7 mm, see Fig. 5.1. While the distance of the photoionized gas cell[48] is 4.3 or 5.9 cm. Interestingly, because the gas jet is produced and photoionized within the return current cage, the gas jet becomes magnetized, B$\sim$10-15 T, by the azimuthal magnetic field produced by the z-pinch. [31] The second key advantage of the gas jet platform is that it does not require any device to contain the gas, which provides several benefits. The gas jet experiences the full power of the X-ray flux since there are no attenuating media between the source and the target such as windows or tamping layers. In this configuration, MA class pulsed-power accelerators, like the Zebra, are able to produce an X-ray flux incident on the surface of the gas jet that is comparable to that of the incident X-ray flux on the front of the cell in the photoionized gas cell experiments on Z. As well, because there is no media between the Z-pinch and the gas jet, no shocks are produced into the gas jet, reducing the complexity of the system. Besides zero attenuation and no shock, another benefit is that the gas jet does not have to expand to reach the proper densities like in the Si/O foil experiment[40]. Further, the gas jet experimental configuration with Zebra allows for a plethora of laser and X-ray diagnostic perspectives, see figure 5.3.

5.4.3 Mitigation of unintended current discharge

When Zebra fires, there is a 2 mega-volt potential between the anode and cathode. The introduction of a gas jet near the z-pinch, within the return current cage, between the anode and cathode presents a very clear and present danger of accidental current arching in which current may discharge into the jet and/or nozzle.

Such current arching is made obvious via two primary hallmark signatures: either the gas jet appears as a dark shadow, see Fig. 5.32, or a jagged path leading through the fringes towards the nozzle and or jet. The first option, a dark shadow in the location of the jet indicates the electron density has surpassed the critical plasma density for the laser diagnostics ($N_c(\lambda = 532nm) = 4.0 \times 10^{21} cm^{-3}, N_c(\lambda = 266nm) = 1.6 \times 10^{22} cm^{-3}$).

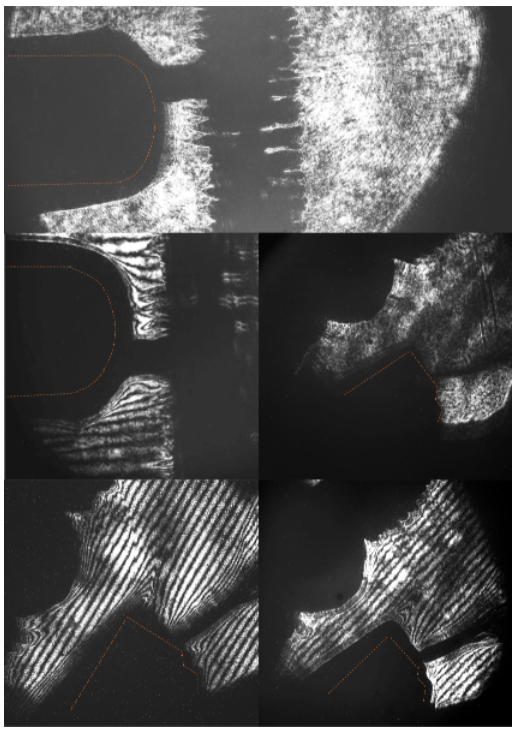

FIGURE 5.32: Example of current discharge from the return current cage arching into a nitrogen gas jet with 600 psi backing pressure. Top: 532nm side-on shadowgraphy. Middle left: 532nm side-on air-wedge interferometry. Middle right: 266nm vertical shadowgraphy. Bottom left: 532nm air-wedge interferometry. Bottom right: 266nm air-wedge interferometry.

This high level of ionization is only made possible due to collisional ionization from current driving the z-pinch. The second option, a jagged path leading through the fringes towards the nozzle and or jet. In this situation there is clear evidence that there is no such current arching. Thus, on first pass, what we observed, within seconds, is extremely strong evidence that the gas jet has been photoionized via the pinch radiation.

Several measures have been taken to isolate the Fast-valve and gas line from current conducting surfaces. First, the gap between the anode and cathode has been increased from 20 mm to 67 mm. Second, the anode stage that the Fast-valve is mounted on is insulated via plastic tubes and rubber pads that keep the stage from contacting the anode plate. Third, 2-3 rubber O-rings and a Teflon ring are placed on the nozzle to

help resist current. Fourth, the gas fill line is coiled, see Fig. 5.2. The coiled gas line acts as an inductive resistor, opposing any initial current that does start to travel down the line. Lastly, the gas line feed through into the Zebra chamber is made of an insulating material. In combination, all of these measures have helped reduce unwanted current discharge into the chamber.

5.5 Summary

This chapter presented a new platform that has unlocked a regime of laboratory astrophysics experiments for university-scale pulsed-power generators that has only been made possible with large-scale ICF experimental facilities, for the study of astrophysically relevant photoionized plasmas. The nature of these experiments requires an intense broadband source of radiation which has been the barrier that limited investigation into laboratory produced photoionized plasmas. The origin of this experiment was from a lack of laboratory photoionized experiments, resulting in slow progress in the field.

Through the safe and successful implementation of a supersonic gas jet system into the Zebra vacuum chamber, photoionized plasmas can be produced and interrogated. Utilizing gas jets as a photoionization medium provides two important benefits. The first being, the hydrodynamics of a supersonic gas jet are self containing resulting in a collimated gas jet. Thus, that there is no auxiliary material needed to position or contain the gas. The second benefit is that the gas jet can be placed much closer to the x-ray source than other photoionization schemes can support. These two key factors allow the gas jet platform to capitalize on the inverse square law, making the flux through the gas jet similar enough to provide complementary experiments. Further, because the motion of the gas jet is order of magnitude slower than that of the x-ray flux the jet is effectively frozen in space during the x-ray pulse.

In the coming chapter the data collected from photoionized supersonic gas jet experiments will show that in a very similar way to the gas cell experiments, the gas jet

platform on Zebra utilizes the x-ray flux in the same manner: to heat, ionize, and backlight the photoionized plasma. Even though these experiments operate in a lower photon energy range than the photoionization experiments on Z, the results between the gas jet and gas cell platforms are complementary. Further, and most importantly, the plethora of laser diagnostics and the longer x-ray pulse make the investigations of photoionized plasmas with Zebra unique and **cutting edge**.

Chapter 6

The Photoionized Gas Cell Experiments

The gas cell platform was developed to study astrophysically relevant photoionized plasmas—like those found in warm absorbers around accretion powered objects like x-ray binary systems[51] and active-galactic-nuceli[52]. The platform has a simple approach—A volume of gas contained within a centimeter scale cell is exposed to the overwhelming x-ray flux produced by Z.

6.1 Evolution of the experimental platform

6.1.1 —Proto-Gen—

The photoionized gas cell experiment, originally fielded circa 2001,[2] had an internal volume of the gas cell was $1\times2\times2.34$ cm^3 in which the 1 cm width and 2 cm height of the gas cell faced the pinch and the 2.34 cm depth of the gas cell was along the radial direction, see Fig. 6.1. The initial front and back windows used were 1.5 μm thick Mylar. In this—proof of concept—the only diagnostic used was x-ray absorption spectroscopy.

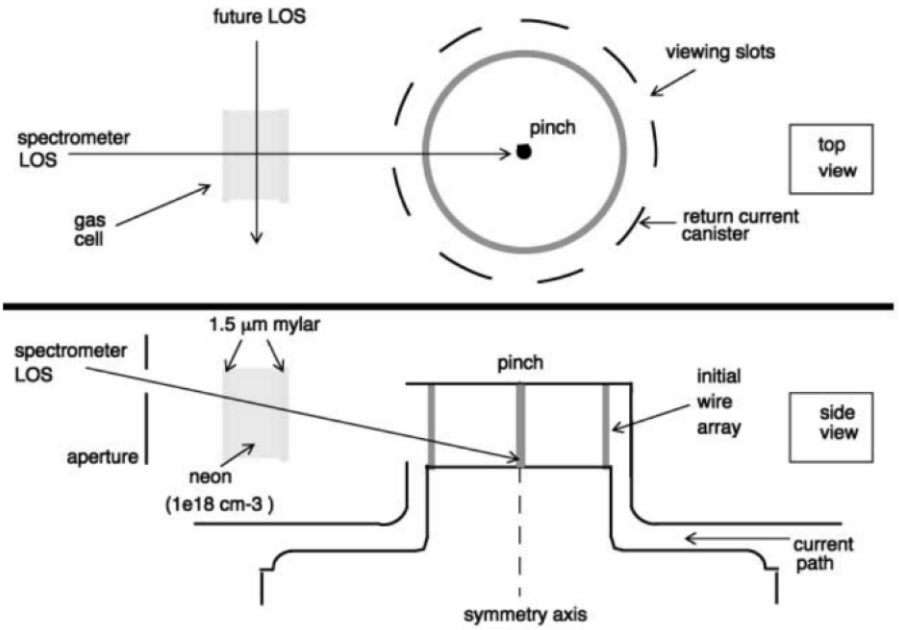

FIGURE 6.1: Schematic diagram depicting the initial setup and orientation of the gas cell experiment. [2]

6.1.2 The Generations

The gas cell has evolved since the original proof of concept experiments. Several aspects of the cell and the platform as whole has changed due to changes implement with the Z-machine. Changes with the platform have namely been internal volume and window material. While, the changes in Z have been from increased current to drive the Z-pinch dynamic hohlraum (ZPDH) and the stile of return current cans. Table 6.1 has been adapted and updated from the dissertation of Daniel Mayes, the graduate student who passed the "torch" that is the gas cell platform.

In the new generation III style of gas cell the internal volume of the cell is now $2\times2\times1.15$ cm^3. One of the two "knobs" of the ionization parameter, $\xi = 4\pi F/n_e$ (2.2.2.1), that can be adjusted is the placement of the cell with relation to the z-pinch radiation, either in the “close” position which is 4.3 cm from the z-pinch and the “far” position, 5.9 cm from the z-pinch. In the close position the x-ray impinging on the front window is

Generation	Gen-I	Gen-II	Gen-III
Time Period	2008–Early 2011	June 2011 – 2018	2019 – Present
Window Material	Mylar	Si_3N_4	Mylar
Window Size [mm]	10.9×20.0	5×5	20×20
Window Thickness	1.4μm	50 or 75 nm	1.4μm
Distance	44	43 or 59	44, 60, TBD
Slots in RCC	18	9	9
Slots in Current [MA]	< 25	> 25	> 25

TABLE 6.1: "Properties that distinguish between different gas cell generations, including the time period, window properties, distance between the gas cell front window and z-pinch axis, number of slots in the return current canister (RCC), and the current in the load." — Adapted and Modified D.C. Mayes dissertation[50]

$\sim 1.3 \times 10^{12}$ W/cm^2, while, the x-ray flux in the far position is reduced by a factor of two. The second "knob" of the ionization parameter that is tuneable with the gas cell is the initial gas density within the cell before the Z shot. Filling pressures are in the range of 3.5–120 Torr, equivalent to atomic/molecular density in the range of 0.1–4^{18} cm^{-3}. While, not part of the ionization parameter, another knob relevant to astrophysical studies that we can manipulate with the gas cell is the element/gas species we can investigate. The initial and primary gas of study so far has been neon. [2, 21, 49] Neon and hydrogen mixtures have been tested, and recently mixtures of neon and argon were fielded, during my torch bearing.

6.2 Diagnostics

Until recently, a pressure transducer and a crystal x-ray spectrometer have been the main forms of diagnosis of the photoionized plasma within the cell.

6.2.1 TREX: Twin-elliptical-crystal time- and space-resolved soft x-ray spectrometer

If you ever find your self walking in the Z facility, unlikely, you should meander over to line of sight 330 of the Z-machine, this is where you will find the lair of TREX. [38] Developed by Pat Lake at Sandia National laboratories, TREX is a beast that requires regular taming. There are several important designs features that should be noted. First, is the genius use of elliptically bent crystals as a method to reduce contaminating spectra. This is accomplished by constructing an ellipse in which one of the two foci is at the location of the target, near chamber center, and the other foci is at the location of the x-ray film. By using such a carefully determined geometry TREX implements a cross-over filter that physically blocks any radiation that is outside of either foci. Further, TREX is a twin crystal spectrometer which allows for a variety of configurations: double data collection, time-gated and time-integrated, and or two different crystals for observation of two different spectral regions. When fitted with an elliptically bent KAP (potassium acid phthalate) crystal, observes neon K-shell absorption spectra in the photon energy range of 860–1230 eV. For K-shell argon absorption spectra, in the photon energy range of 2770–4574 eV, can be observed by configuring TREX with polyethylene terephthalate (PET). Analysis of the x-ray absorption spectra allow the extraction of the charge state distribution, electron density, and the electron temperature of the plasma. [21, 46, 49]

6.2.2 Pressure

The second diagnostic added to the gas cell platform was a pressure transducer. With this addition the pressure transducer allowed for in-situ gas fill pressure readings up until the shot time of Z. Of the various benefits, most importantly was that this provided a much more accurate estimation of the true neutral density in the gas cell at shot time. Prior to the pressure transducer, the gas neutral density was defined by the fill pressure. This, while at first seems innocent, becomes unfortunately messy if there happens to be a leak in the gas cell. In this circumstance the pressure at shot time was estimated by

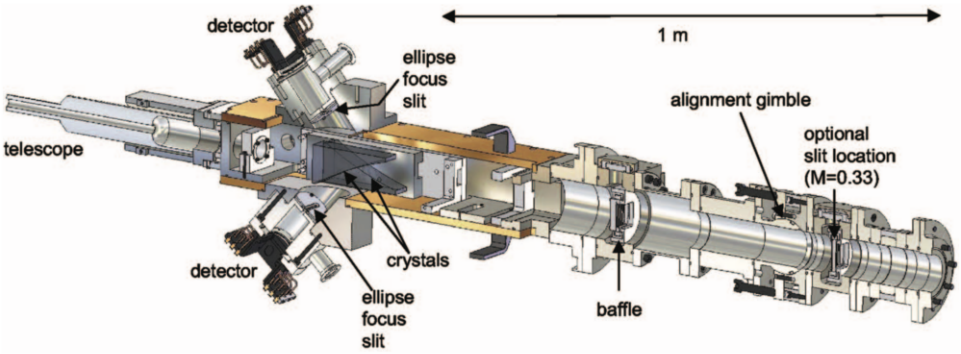

FIGURE 6.2: Cut-away diagram of a twin crystal/twin MCP detector spectrometer. [38]

factoring in the, *very rough*, leak rate. Now, even if there is a leak, the pressure will still be known to a high degree. Leaks can be compensated for by overfilling to hopefully hit the right pressure by shot time.

A second benefit of the pressure transducer is the ability to measure the pressure in real time up until shot time. There has been several times that an issue with the gas fill could have been rectified had the real time pressure measurements been operating. For example, shot z3461 had the misfortune of a large accidental burp of atmosphere. Ironically, the gas cell did not burst... as it tends to pop just lookin' at it wrong. The result was a gas cell that was primarily filled with nitrogen, oxygen, argon, and other various gases that compose the air we breathe. What's more, the spectra measured from this shot was unusable unlike the spectra from popped gas cells, as that spectra is much needed null data.

6.2.3 Photon Doppler Velocimetry

A new chordal interferometry fiber based diagnostic has been integrated into the gas cell platform, known as Photonic Doppler velocimetry (PDV). This new diagnostic provides an alternative method to measure electron density, as well as allowing for a means to validate simulated electron densities. An important aspect of modeling done to date is the presence of inward propagating shockwaves generated from the front and

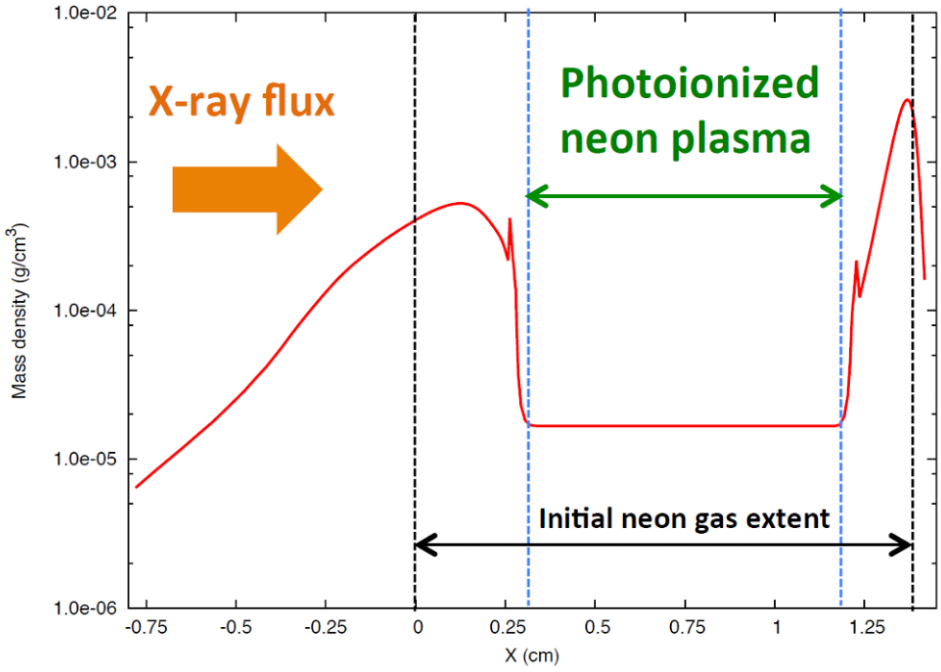

FIGURE 6.3: A simulation performed with Helios-CR at the time of the x-ray pulse peak, showing the extent at which the front and back propagating shocks have reached. The central region between the shocks the predicted location of the qausi–hydro-unperturbed neon plasma.

rear windows upon irradiation from the z-pinch radiation. One-dimensional radiation hydrodynamic simulations predict a region of quasi–hydro-unperturbed photoionized neon plasma. Figure 6.3 shows the location of the front and back shock propagation at the time of the x-ray pulse peak. The space between these shocks in the predicted region of the quasi–hydro-unperturbed photoionized neon plasma, that has yet to be validated.

6.3 Development of PDV

An important initial test for the PDV diagnostic was the ability to assess the uniformity of the plasma within the gas cell. A measurement that was not possible with x-ray absorption spectroscopy and of course certainly not with the pressure transducer. It is prudent that first we dive into the theory of these measurements so that some of the design consideration nuances will make more sense.

6.3.1 PDV Theory

Prior to the development of PDV, Fabry-Pérot interferometers and VISAR (Velocity Interferometer System for Any Reflector) were used to diagnose km/s velocities[**strand2006**]. Remarkably, PDV shares the important capabilities of both VISAR and Fabry-Pérot velocimeters, while side-stepping the disadvantages of each. Like VISAR, PDV can measure over long intervals and is compact compared to Fabry-Pérot interferometers. Similarly to Fabry-Pérot interferometers, PDV is less sensitive to variation in light intensity and can detect multiple velocities. Unlike VISAR and Fabry-Pérot velocimeters, PDV is not vulnerable to abrupt velocity changes. By combining the advantages of these two velocimeters and improving on their disadvantages, PDV has become a robust diagnostic for high speed velocity measurements.

Now, taking into consideration that PDV has been developed off of widely available telecommunication technology and the straightforward implementation required, it is of no surprise that PDV has become a widely used diagnostic[13]. For example, the load current of cylindrical z-pinches and liners has been inferred from PDV measurements[57]. For MagLIF (Magnetized Liner Inertial Fusion), PDV has been used to measure the speed of flyer plates to infer the maximum current going through the load[25]. Further PDV has been used to observe the surface of exploding, electrically thick, metal rods that are pulsed with large currents, $\sim$1MA, to investigate the electrothermal instability[28].

The basic physics principle at the heart of PDV, is the observation of a changing optical path length. The optical path length, defined by a "send" and "receive" fiber optic probe, can be precisely measured and tracked over time via PDV, see Fig. 6.4. For velocity measurements, the "send" and "receive" probe are one in the same since it is the moving object in question that reflects the sent light back to the receiving probe. Thus, the path length is ultimately twice the distance from the dual-purpose probe to the moving object. For velocimetry the optical path length changes due to the physical path length changing. The bouncing of light of the moving object gives rise to a double relativistic

Doppler shifted frequency, given as,

$$f_{2\Delta} = \frac{c - v}{c + v} f_0, \tag{6.1}$$

where $f_0 = c/\lambda_0$ is the reference PDV laser frequency, v is the velocity of the moving object, and c is the speed of light. At first blush, the double relativistic Doppler shift of the reference frequency is not immediately obvious. The first shift arises as a consequence of the perceived frequency of the reference laser in the high velocity reference frame of the moving object. Once the reference laser light has been absorbed by the object, which has been relativistically Doppler shifted $f_0 \rightarrow f_0'$, it is remitted back towards the send/receive probe. Just as before, due to the difference in reference frames of the probes and moving object, the light emitted from the moving object has an extra kick,$f_0{}' \rightarrow f_0{}''$. Thus, by the time the laser light reaches the receive probe the reference frequency has been relativistically shifted twice. This is where the magic of PDV comes in, by interfering the reference frequency with the Doppler shifted frequency a time changing beat frequency can be recorded, with the following functional form,

$$\bar{f}(t) = |f_{2\Delta}(t) - f_0| \approx 2\frac{|v(t)|}{\lambda_0}. \tag{6.2}$$

The detection of plasma and radiation with PDV has been proposed[14] and implemented[14, 56, 58]. In contrast to PDV measurements of velocity, plasma measurements are due to a time changing refractive index as opposed to a changing physical path length. In general PDV measurements with have both of these factors, typically one or the other is negligible (Eq. 6.3).

$$\frac{d}{dt} OPL(t) = \hat{n}\dot{L} + L\dot{\hat{n}} \tag{6.3}$$

For plasma, PDV the first term on the LHS of Eq. 6.3 drops out and the second term is dependent on the index of refraction rate of change. Putting this together we can define

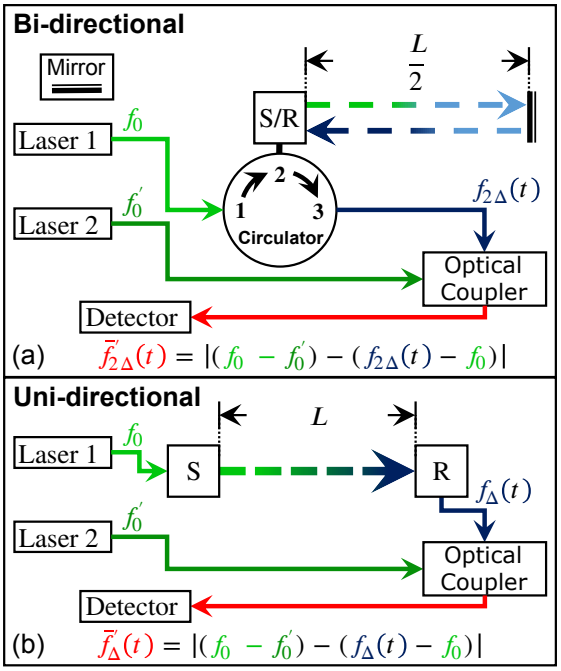

FIGURE 6.4: The two styles of PDV are: (a) bi-directional which uses a dual send and receive probe (b) uni-directional uses separate send and receive probes[67]

the PDV plasma measurement more clearly. PDV is capable of measure the time rate of change of the refractive index integrating over the PDV path. We can formulate in the following way,

$$\bar{f}_\eta(t) \approx -\frac{\eta}{\lambda}\frac{d}{dt}\int_0^L n(x,t)dx. \tag{6.4}$$

Figure6.5 shows the refractive index of a plasma as function of electron density. The range chosen reflects the expected electron density range. If the refractive index is assumed not to vary along the path, Eq. 6.4 becomes,

$$\bar{f}_\eta(t) \approx -L\frac{\eta}{\lambda}\frac{d}{dt}\hat{n}(t). \tag{6.5}$$

From this point, we can integrate Eq. 6.5 and produce a refractive index time history. Next the electron density can be calculated by solving for it using the equation for the

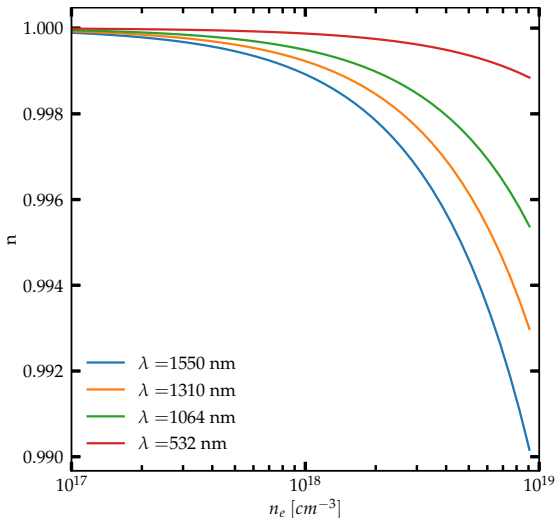

FIGURE 6.5: The refractive index for wavelengths 1550, 1310, 1064, 532 nm shown for the expected the range of the expected electron number density.[67]

refractive index.

$$n(n_e) = \sqrt{1 - \frac{n_e}{N_c(\lambda)}} = \sqrt{1 - \frac{(e\lambda)^2 n_e}{m_e \varepsilon_0 (2\pi c)^2}}, \tag{6.6}$$

Plasma measurements and more generally changes in the index of refraction, can be made via two different styles of PDV configuration. The configuration implemented for velocity measurements is known as bi-directional, where a dual-purpose send and receive probe are used in conjunction with a reflective surface, ie. the moving object. The bi-directional configuration is illustrated in Fig. 6.4(A). The alternative PDV configuration style is known as uni-directional (Fig. 6.4(B)). Uni-directional PDV uses separate send and receive probes with no need for a reflective surface. Since there is no "bounce" of the laser light there is only a single relativistic Doppler shift and when $v \ll c$ it can be approximated as,

$$f_\Delta \approx \frac{2c - v}{2c + v} f_0. \tag{6.7}$$

In the uni-directional PDV configuration the emergent beat frequency takes a slightly different form,

$$\bar{f}(t) = |f_\Delta(t) - f_0| \approx \frac{|v(t)|}{\lambda_0}. \tag{6.8}$$

To account for the difference in the implementation of PDV, the inclusion of a configuration coefficient η can help to clear up any confusion,

$$\bar{f}_\eta(t) = |f_{\eta\Delta}(t) - f_0| \approx \eta\frac{|v(t)|}{\lambda_0}, \tag{6.9}$$

where,

$$\eta = \begin{cases} 1 & uni-directional \\ 2 & bi-directional \end{cases}. \tag{6.10}$$

Regardless of the PDV configuration, the standard implementation of PDV is incapable of perceiving direction; that is, the interference that results in the observed beat frequency is proportional to the absolute value of the velocity. There are a variety of PDV schemes that utilize a frequency offset such that depending on the observation the measurement either increases above the offset or decreases, thus providing a means to detect directionality. Through the use of an auxiliary PDV laser or an acoustic-optic frequency shifter, an offset in the reference signal can be achieved. The beat frequency that results from the inclusion of a frequency offset is given in following manner,

$$\bar{f}'_\eta(t) \approx |\Delta f_0 + \eta\frac{v(t)}{\lambda_0}|, \tag{6.11}$$

where $\Delta f_0 \equiv f_0 - f'_0$ is the difference in the two reference laser frequencies used. There are two main styles of frequency shifted PDV, up-shifted and down-shifted. Up-shifted PDV is used when measurements won't exceed the dynamic range of the oscilloscope. Conversely, measurements that require a larger dynamic range can implement down-shifted PDV. The price for extending the dynamic range with down-shifted PDV is a

poorly resolved ambiguous measurement when $\eta v/\lambda_0 \approx |\Delta f_0|$. For the PDV measurements shown in Ch. 9, up-shifted PDV was used. In an effort to reduce unnecessary complexities that detract from comprehensive understanding, the frequency offset will be removed from the discussion without any loss of specificity. This can be done because the offset is essentially a gauge that ultimately has no effect on the physics being measured, rather it is purely a diagnostic magic trick that allows directionality in the measurements to be revealed. This provides us the space and freedom to focus only the Doppler shifted frequency that is a result of the photoionized of the gas in the cell, $f_{\eta\Delta}$.

6.3.2 PDV Signal Processing and Analysis

The beat frequency is extracted from the raw PDV measurement via Short-time Fourier-transforms (STFT),

$$S(t,f) \equiv \int_{-\frac{\tau}{2}}^{\frac{\tau}{2}} w(t-t')s(t')e^{2\pi i f t'}dt'. \tag{6.12}$$

The beat frequency is extracted by implementing STFTs along the raw digitizer signal; for each designated point in the raw digitizer signal a STFT of width τ is centered about $s(t')$, utilizing a windowing function, $w(t-t')$, to bound the integration. Various parameter choices can be made depending on the physics under investigation. The STFT analysis requires the duration of integration to be small enough that the change in velocity is negligible. If the STFT integration covers a range that is large enough to have a non-zero change in velocity, processing artifacts will arise. This stipulation also has implications for rapidly accelerating phenomena[13].

On the topic of windowing functions, the "Hann" window was implemented for the data presented; the Hann window provides the best frequency precision on average for most cases and is the most stable at larger frequencies >2 GHz[12, 13]. Depending on the parameter constraints and other aspects of the diagnostic implementation, overlapping of STFTs may be employed for data smoothing from one STFT analysis to the next.

The end result of the STFT processing produces a frequency power spectrum like the

one presented in Fig. 6.6. The spectrogram shows the measured relativistic Doppler shift due solely to the effects of the increasing plasma density. Note the initial frequencies are centered about 0. Had we chosen to keep the complexities of the frequency offset in the discussion the initial frequencies Fig. 6.6 would have been centered around 1-2 GHz instead. The spectrogram was processed using STFT durations of $\sim$1.1 ns with $\sim$0.3 ns overlapping temporal regions on either side. The spectrogram shows the most comprehensive picture of the measurement, showing the ionization of the gas starting $\sim$60 ns before the peak of the x-ray pulse that occurs at 0 ns. Chapter 9 will go into great depth revealing what we can learn from extraction of beat frequency and electron density time histories that can be extracted from such spectrograms.

6.3.3 PDV frequency uncertainty

The uncertainty in the measured beat frequency from PDV are contingent on three main parameters: Digitizer sample rate f_s [GS/s], Fourier analysis window duration: τ [s], and the Noise fraction: $\frac{\sigma_s}{A}$.

The dynamic range of the PDV measurement, aka the maximum resolvable beat frequency, is primarily dependent on the sampling rate of the digitizer, f_s. The largest beat frequency possible to be recorded is defined by the Nyquist limit, $\tilde{f}_\eta^{\max} \equiv f_s/2$. For the PDV system on the Z-machine, the sample rate is 80 GS/s (80 GHz). Thus, considering the Nyquist limit, the dynamic range is limited to 40 GHz. Based on simulated electron density time histories, the expected maximum beat frequency was on the order of 10 GHz. Thus, this authorized the use of up-shifted PDV without worry of maxing out the digitizer and loosing data.

An important factor, second only to the sample rate, is the STFT analysis duration, τ. As mentioned earlier STFT analysis requires a constant beat frequency, i.e. constant refractive index, over the analysis duration. Thus, depending on the expected dynamics in the experiment an upper bound on the length duration can be determined. The longer the duration used the lower the uncertainty is in the values extracted. One of the sources

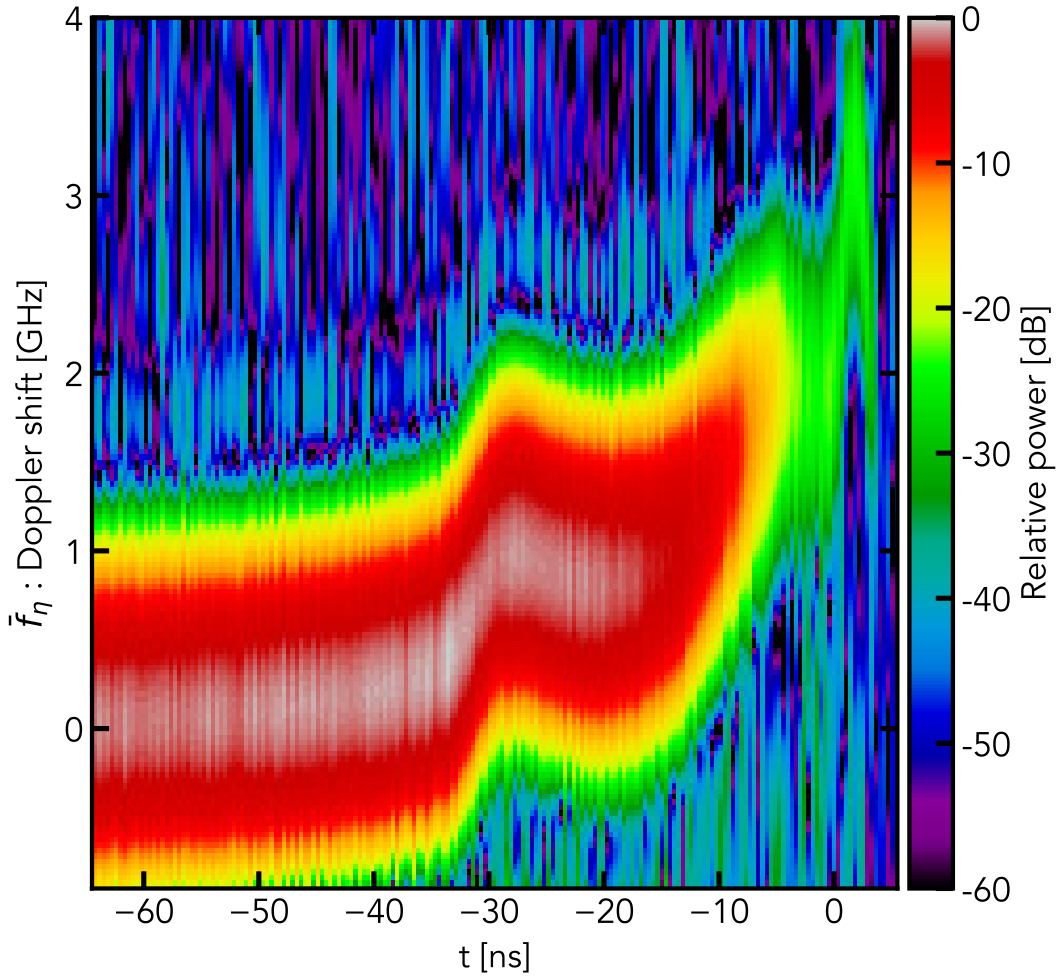

FIGURE 6.6: "Power frequency spectrogram from the back PDV probe of shot Z3600, neon gas fill with 15 Torr. The spectrogram has a frequency offset of $\Delta f_0 \approx 2$ GHz. Spectrogram processing parameters: $f_s = 80$ GS/s, $\tau \sim 1.1$ ns, STFT overlap $\sim$0.6 ns. Time axis leads up to the peak x-ray pulse, located at 0 ns." [67]

of strength PDV draws on is the massive amount of measurements made. For a digitizer with 80 GHz bandwidth, an analysis duration of 1 ns provides 80 measurements per duration window, thus even short durations are still packed full of relevant information.

For PDV measurements, the ratio of the signal's standard deviation and the signal amplitude, σ_s / A, defines the noise fraction[12, 13]. The PDV measurements presented used NKT photonics' erbium doped fiber amplifier and a MITEQ photodetector with a frequency response in the range of 0.0001–20 GHz. The PDV system used on Z has a noise fraction quoted to be on the order of 10%[13]. Such low noise fractions are due in part to the precise and stable nature of the laser used as well as precise and characterizable detectors. Thus, the lower limit of the noise fraction is bounded by the inherent photon noise of the detectors used.

Taking these three main parameters, the expected uncertainty for PDV is,[13]

$$\sigma_{\bar{f}} = \frac{1}{\pi}\sqrt{\frac{6}{f_s \tau^3}}\frac{\sigma_s}{A}. \tag{6.13}$$

We can go further and define the limiting case for the frequency resolution,

$$\sigma_{\bar{f}} \geq \frac{1}{\pi}\sqrt{\frac{hc}{\lambda P_T \tau^3}}, \tag{6.14}$$

where h is Planck's constant and P_T is the power of the signal returned from the target. PDV owes its high-quality low noise to several important functional characteristics of the expected uncertainty that should be discussed. Maybe the most significant is the inverse proportionality of the uncertainty to the square root of the sample rate; As already discussed, high sample rates play a major role in the precision that can be achieved with PDV. Next in terms of significance, as before, the analysis duration is highly important as the uncertainty is proportional to $\tau^{-3/2}$. Last but not least, is the proportionality of the uncertainty with the noise fraction. Based on the highly characterizable signals possible the standard deviation of the signal is inherently low. With lasers being what

they are, intense coherent light sources, the signal amplitude is typically very strong and when combined with robust probe alignment, the uncertainty is driven even lower.

If we take the example values used earlier we can start to get a feel for what is possible with PDV, ex. 10% noise fraction, τ=1.0 ns, sample rate of 80 GS/s results in uncertainties of the beat frequency of the order of MHz.

6.3.4 Refractive index resolution

The ultimate goal is not just the beat frequency measurement, it is the measurement of the time changing refractive index of the plasma. Thus, it's important to push further to understand what resolution PDV is capable with regards to measurements of the refractive index.

By integrating Eq. (6.5) over one analysis duration τ, we can estimate the expected resolvable change in the refractive index.

$$|\Delta\hat{n}| \approx \frac{\lambda\tau}{\eta L}\bar{f}_\eta = \frac{\lambda\tau}{\eta L}|f_{\eta\Delta}(t) - f_0|. \tag{6.15}$$

Since the difference of the Doppler shifted frequency and the PDV reference frequency is the beat frequency; thus, the uncertainty of the beat frequency is the minimum difference that can be observed. From this understanding, one can use the uncertainty of the beat frequency in place of the difference in the right-hand side of Eq. (6.15). Following through with this substitution results in,

$$|\Delta\hat{n}| \geq \frac{\lambda}{\eta L}\sigma_{\bar{f}}\tau. \tag{6.16}$$

In a similar fashion, as was done with the beat frequency uncertainty analysis, we can evaluate Eq. (6.16) to get a feel for what refractive index resolution can be achieved. Therefor, evaluating Eq. (6.16) with $\sigma_{\bar{f}} \sim$15 MHz, $\tau \sim$1 ns, and L=20 mm, results in a resolvable change in the refractive index of $|\Delta\hat{n}| \sim 7 \times 10^{-7}$.

Now, unlike the uncertainty of the beat frequency, the resolution of the refractive index is dependent on the PDV configuration implemented, uni vs bi-directional. This duality is depicted in Fig. 6.7 where the uni-directional case is illustrated with solid traces and bi-directional with dashed traces. The traces that correspond with dBm value represent the limiting case of the minimum resolvable change and the red trace corresponds to the expected minimum resolvable change, with the noise fraction representative of the Z PDV system. Referring back to Fig. 6.5, the total change in refractive index expected in the photoionized gas cell experiments is on the order of $\sim 10^{-2}$ for λ=1550 nm. Taking the ratio of the total change with the expected resolvable change is on the order of $\times 10^4$, demonstrating the high level of precision and power possible with PDV.

6.3.5 PDV design considerations

6.3.5.1 PDV experimental goals

While the use of fiber optics allow for —easy— delivery of diagnostic lasers, there were still several design challenges that needed to be addressed. The primary objective for the PDV diagnostic was the internal assessment of plasma uniformity during the experiment. Uniformity was diagnosed via two uni-directional collimated PDV probes placed $\sim$4 mm apart, see Fig. 6.8. The fiber optic probes had a 0.15°beam divergence and a 0.3-0.4 mm beam waist, with a working distance over an order of magnitude larger than the width of the cell, $\sim$20 cm. The purple and green arrows in Fig. 6.9 show the front and back probes, respectively.

The choice of probe placement was a delicate balance between two factors. The first being, separating the two probes far enough in order to make sure the measurements were spatially distinct. The second factor was in relation to the shocks that are launched by the front back Mylar windows. While studying the shock propagation was of interest, it was not the goal for the initial testing of the PDV diagnostic with the gas cell, remembering that our primary goal was to interrogate the central region of the gas cell,

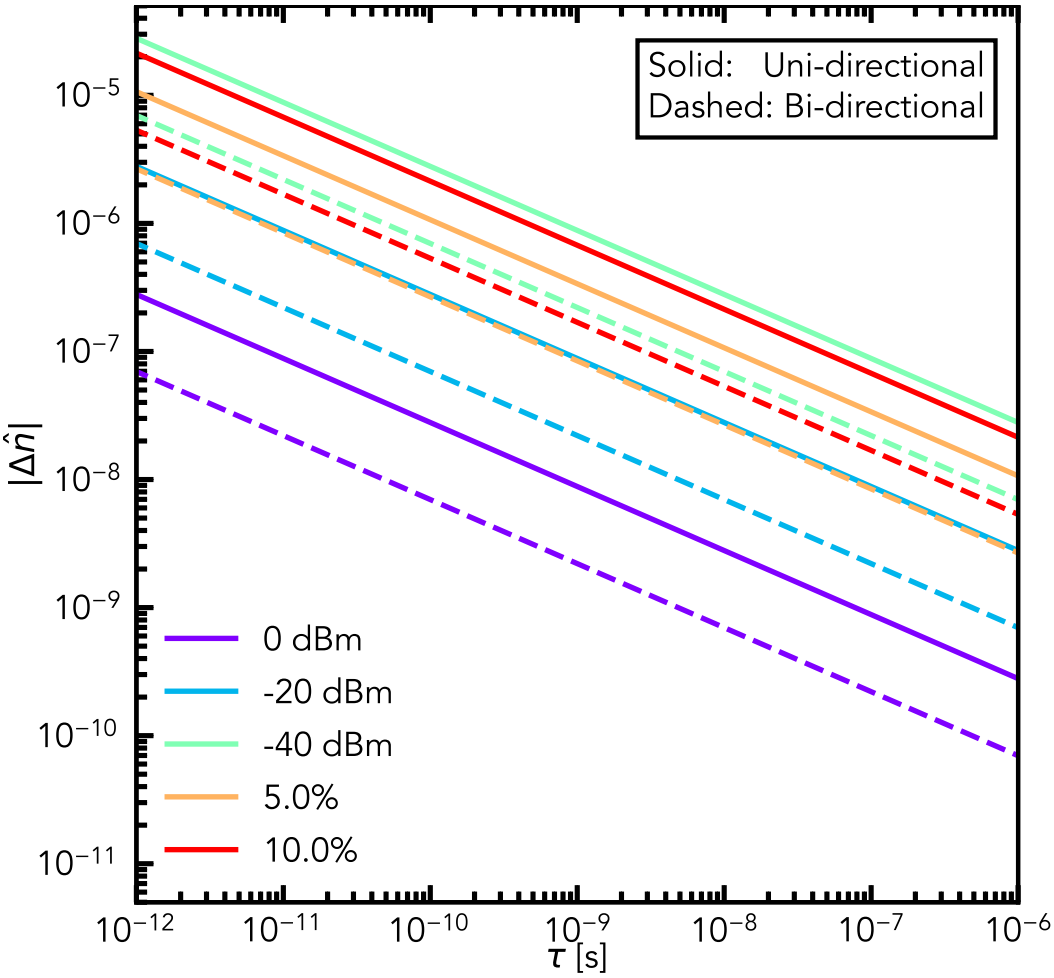

FIGURE 6.7: Minimum resolvable change in the refractive index for uni-directional and bi-directional. Values for the noise fraction and power are given. The values have been calculated for the length of gas cell, L=20 mm. [67]

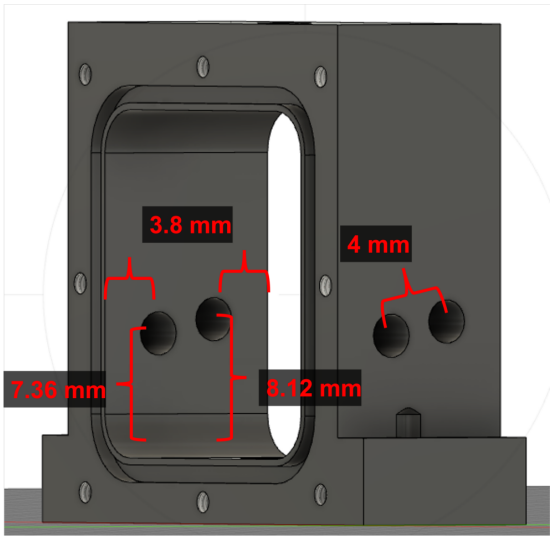

FIGURE 6.8: Location and relative dimensions of plasma PDV probe locations. Left side of the image is the front side of the cell that views the pinch. Probe locations are along the 12°line-of-sight of the TREX spectrometer.

in which the photoionized neon plasma was predicted to be qausi–hydro-unperturbed. Figure 6.10 shows traces of electron density evolving over time. The large spikes on the left and right are the positions of the front and rear Mylar windows, respectively. Arrows, are pointing at the location of the traces of electron density denoting the time that the x-ray pulse has peaked. Based on this analysis and the choices that needed to be balanced between distinct measurements while keeping the probes away from the shocks, a separation distance of 4 mm was chosen. The two probes were placed approximately 2 mm in front and in back of the horizontal center of the gas cell.

The secondary goal for the initial implementation of the PDV diagnostic was to extract electron density, specifically, time resolved electron densities. Such a measurement would not only allow a new method to test and validate simulated electron densities, it would as well provide a measurement that could be compared to the electron density measurements calculated from the x-ray absorption spectroscopy. This goal is what motivated the two probes to be placed along the 12°line of sight of which the TREX spectrometer views through the gas cell, see Figs. 6.9 & 6.8. Thus, allowing for coincident

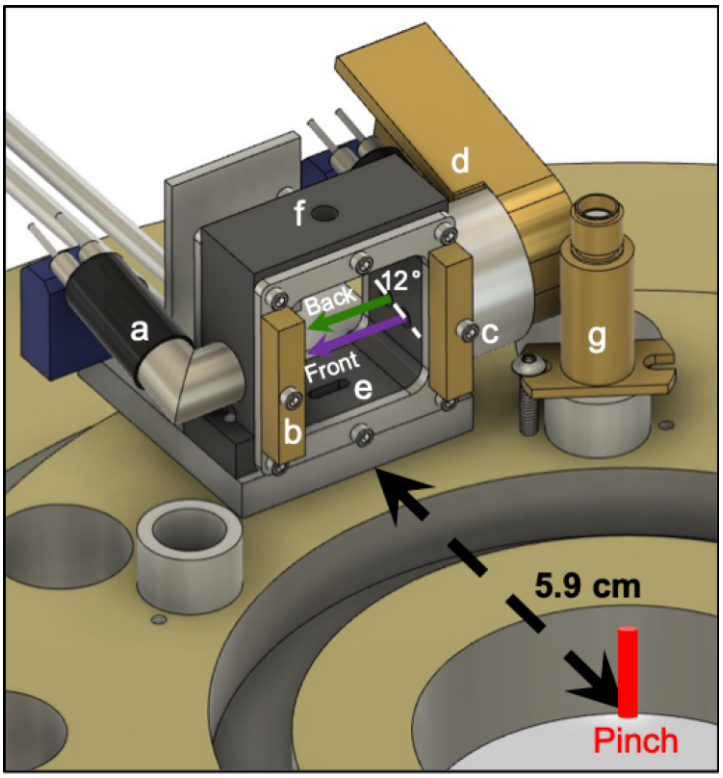

FIGURE 6.9: "View of the gas cell on the anode plate. In the “far” position the front window of the gas cell is 5.9 cm from the z-pinch. (a) 90°fiber optic component, responsible for sending and receiving the front and back probe beams (the purple and green arrows, respectively). (b), (c), (d): Radiation shields. (e) Gas fill inlet, (f) Pressure transducer port. (g) Anode plate B-dot. The B-dot and radiation shields on the left side were removed for figure clarity."- [67]

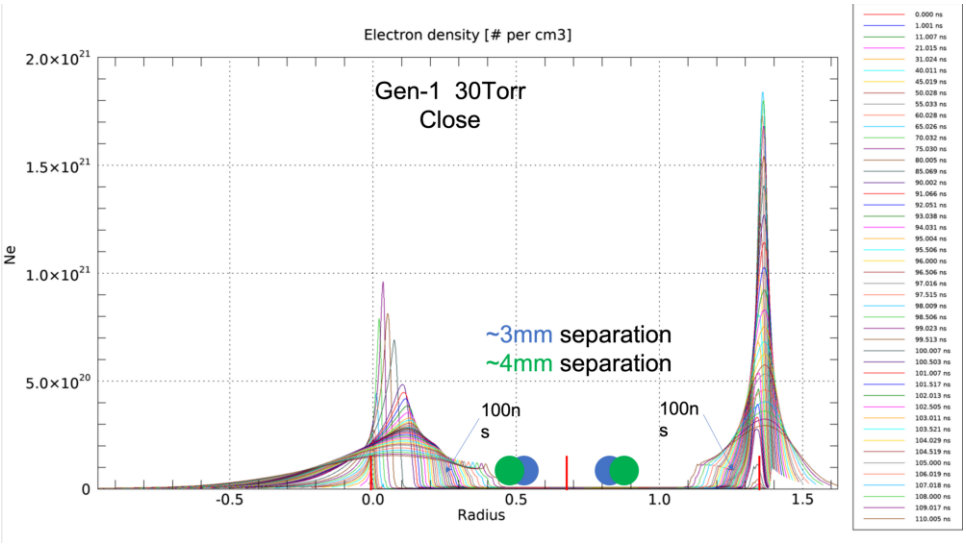

FIGURE 6.10: Probe placement location based on simulations of the photoionized neon gas cell with 30 Torr. Electron density profiles show the extent of the shocks generated. The green and blue dots represent proposed locations for the plasma probes with either a 3 or 4 mm separation, respectively

measurements in space and time to be made of the photoionized neon plasma for the first time.

6.3.5.2 PDV system performance

In a close second to the PDV experimental design considerations was the potential for adverse radiation effects within the fiber optic system due to the close proximity of the gas cell with the overwhelming radiation source that is the z-pinch dynamic hohlraum. [60] The optical properties of fiber optics can be modified when exposed to ionizing x-ray and UV radiation. [59] There are three interrelated effects possible within fiber optics when exposed to intense radiation. The first effect is known as radiation induced attenuation (RIA)—sometimes referred to as "fiber darkening"— which is the decrease in fiber transmission efficiency. A second possible effect is radiation induced light emission. The third effect, and the most important, is radiation induced refractive index changes. Fiber optics when exposed to ionizing radiation can experience a change in the internal refractive index. The refractive index is altered due the generation of

point defects, “color centers”, which cause density variation along the fiber within the silica matrix. [59, 6]

The potential for radiation inducing a time changing refractive index within the fiber optics was certainly disturbing to say the least, resulting in poor sleep. Such an effect was not only possible, it has been documented,[10] a source of discussion and pain due to the trouble such a noise artifact has caused in other experiments which were implementing PDV on Z... but much much much further away.

To combat such nightmare inducing effects, three radiation shields were made to protect the fiber optics delivering the lasers to the cell. Front facing shields were made from stainless-steel. Side shields made from brass, which protected the fiber optics from above, below, the sides, as well as the front. If it were not for Alexey’s careful eye, we almost missed a weak point in the shielding in the front facing portion of the shielding, to solve this, brass bars were handcrafted to strengthen the radiation shielding in the front of the cell, see Figs. 6.9. The three different radiations shields employed are shown in Fig. 6.11 with the relevant dimensions for the radiation blocking portion of the shields shown.

6.3.5.3 Gas cell placement

After all of these considerations for the implementation of PDV as a diagnostic for the gas cell, there was still one more. Being as the gas cell experiment is a ride-along, with several experiments, it is a strict priority that the gas cell, or any of the other experiment, does not interfere with any of the existing hardware or other experiments. The main concern, *annoyance*, was the B-dots on either side of the gas cell. These B-dots are shown in Fig. 6.9. Unfortunately, the complication from these was a limit to the gas cell footprint. While fiber optics are —bendy— they do have a limit to their bend radius. Dual 90 degree fiber optic probes were implemented to decrease the area taken up by fiber optics, see Fig. 6.12. A delicious secondary benefit of these 90 degree dual fiber optic probes was that the compact design of the probes improved the ability to shield the fibers.

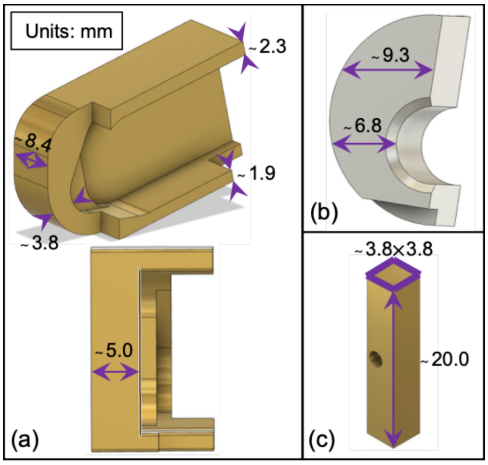

FIGURE 6.11: "Radiation shields used to protect and mitigate noise introduced into the fiber optic system, with relevant shielding dimensions depicted in units of millimeters. (a) Side shields (brass) protect irradiation of the optical components from the front, top, side, and bottom. (b) Primary front facing radiation shield (stainless-steel). The top dimension is for the portion shielding the RIET radiation noise probes and the bottom dimension is for the portion shielding the plasma probes. (c) Secondary front facing shield (brass) to protect a weakly shielded location between gas cell body and the primary front facing shield"-[67]

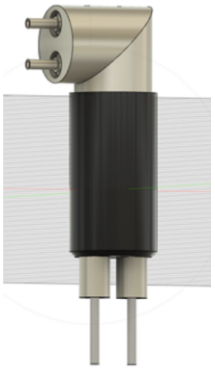

FIGURE 6.12: 90°fiber optic component, developed for the gas cell platform.

6.3.5.4 Characterization of the nightmare that is radiation induced effects

A time changing internal refractive index within the fiber optics had the potential to complicate the signal to the point of being unintelligible. The nightmare stems from the radiation signature that would be superimposed onto the data signal. When fiber optics are exposed to ionizing radiation, an increase in the internal refractive index occurs. This in turn, results in a measured beat frequency that has the opposite response to that of a plasma with an electron density that is increasing overtime. Specifically what this means is the following: If no other physical process occurs except for the irradiation of the fiber optics the measured beat frequency will be negative. Similarly, if the only physical processes being measured is that of a plasma evolving over time with an increasing plasma density, the measured beat frequency will be positive. Thus, the nightmare is two competing signals that have opposing time signatures, and without adequate shielding, irradiation of the fiber optics supporting the PDV diagnostic will have a superposition of competing signals that very well could be too gnarled to separate in any meaningful way.

In order to achieve some sort of sleep, it became clear that the characterization and quantification of the potential time dependent mayhem that could rear its head due to radiation induced effects in the fiber optics was crucial. Radiation Induced Effects and Timing (RIET) probes were integrated into the platform to handle this task. These RIET probes were simply, fiber optics with mirrors mounted on the ends, used in bi-directional PDV configuration(Fig. 6.13 b). To make sure that measurements made with RIET probes characterized the radiation noise in the plasma probes, they were made with same single-mode fiber (SMF-28) used to make the plasma probes as well as they were located as close as possible to the plasma probes. The RIET probes were used on both sides of the gas cell, see Fig. 6.14.

A point to note here is that the RIET probes had more shielding than the data probes. While there is a difference in shielding, it's a minor difference, about $\sim$2.5 mm more

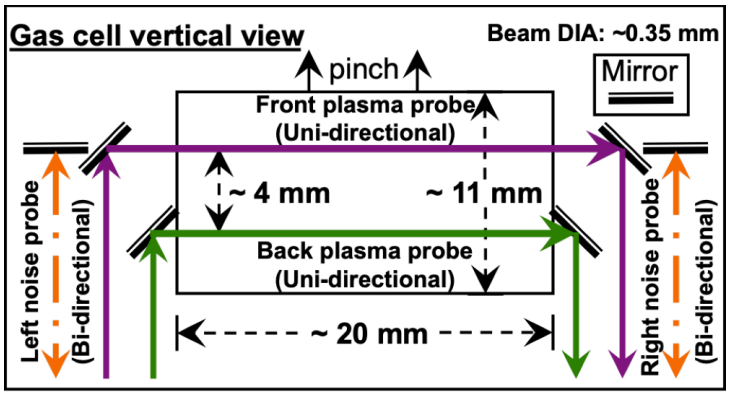

FIGURE 6.13: "Optical schematic of the gas cell and RIET (Radiation Induced Effects and Timing) radiation noise probes. The "Front" and "Back" PDV probes (uni-directional) measure plasma conditions within the central region of the gas cell. The RIET PDV probes (bi-directional) measure the effect of radiation on the system on the left and right side of the cell."- [67]

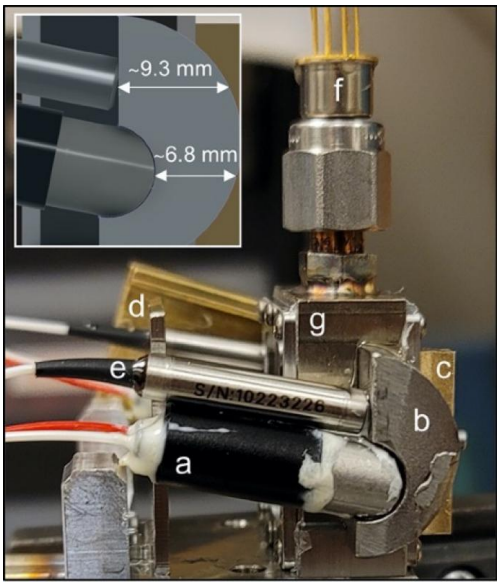

FIGURE 6.14: "Side view photo of the gas cell with PDV probes attached. Main figure: (a) 90°PDV probes. (b), (c), (d): Radiation shields. (e) RIET noise probe for the characterization of radiation induced effects in the fiber optics. (g) Gas cell body. (f) Pressure sensor transducer. Inset figure: schematic depicting the relative amount of shielding for the RIET, radition noise, probes (top, ∼9.3 mm) compared to the plasma probes (bottom, ∼6.8 mm)."-[67]

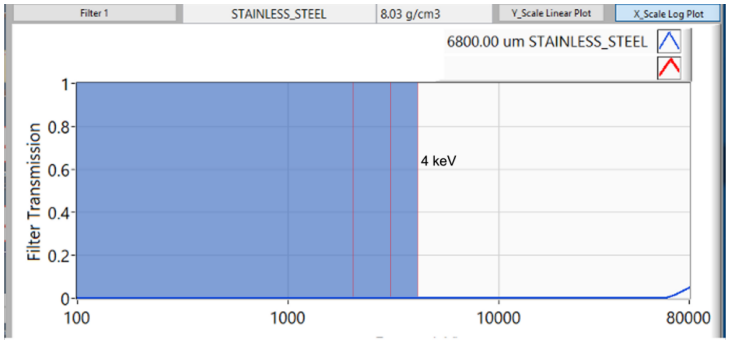

FIGURE 6.15: Transmission estimation for 6.8 mm stainless steel for photon energy range 0.1–80 keV. The range of significance for the radiation drive delivered from the ZPDH is < 4 keV.

than the data probes. As a check, Pat Lake at Sandia National Laboratories, used the filter transmission tool developed by Michael Jones, to calculate an estimation for what levels of transmission we could expect through the stainless steel shielding. Figure 6.15 shows the calculation of transmission through 6.8 mm of stainless steel, for a photon energy range of 0.1–80 keV. The transmission through portion shielding the probes only starts to rise around 80 keV with a transmission value < 0.1. Thus, for the difference in transmission that would result from a difference of ∼2.5 mm for the radiation range expected from the z-pinch dynamic hohlraum, < 4 keV, is of little concern. While this is the case, the shielding for the plasma probes vs the RIET probes will be optimized to be more equal to improve comparison. A RIET noise probe was included for the two fiber lines running to the cell. This allowed for resolving any potential asymmetries of the irradiation of the PDV system. As well, this allowed for redundancy of the radiation noise measurements.

6.4 Summary

The photoionized gas cell platform has been one of the few sources of high-quality laboratory data. This is due in part to the necessity of large-scale high-energy pulsed-power platforms originally designed for ICF experiments. The platform originally fielded in 2000 as a proof of concept has come a long way in terms of capability and

scientific observations.

"Over modeled and under diagnosed" has been the catchphrase for a while now. Implementing new diagnostics is not the priority of the national lab for ride-along experiments. Coming from working with laser diagnostics on Zebra, was the perfect background to take advantage of the newly available chordal interferometry diagnostic capability of the Z-facility, known as Photon Doppler velocimetry (PDV).

Incorporating PDV into the gas cell was a multi-team effort between UNR, Sandia, and the fiber optic company Ascentta. Prioritizing the scientific goals while acknowledging the operational constraints required careful thought and approach. This implementation of PDV represents several firsts at the Z facility. It is the first time that PDV has been successfully implemented in close proximity of the z-pinch, 5.9 cm. Another first was pushing the PDV diagnostic to make high-quality sub-nanosecond measurements allowing for electron density time histories to be extracted. Further, the effects of the harsh radiation environment were mitigated, which was confirmed by the characterization of the radiation noise, which showed the noise in the system was inconsequential compared to the PDV plasma signal from the gas cell. PDV has proven to be a valuable diagnostic for the photoionized gas cell platform.

Chapter 7

Experimental Results I: Spectral Characterization of Zebra's Radiation Drive

7.1 X-ray spectroscopy of aluminum z-pinch

Spectral characterization of aluminum z-pinch radiation drives were studied in the range of 40–700 Åon the 1MA Zebra pulsed-power driver. As is known currently, this is the first broad range spectral measurement of aluminum. Cylindrical wire-arrays composed of eight 15μm aluminum wires, 6 mm in diameter, and 20 mm in height were used for these experiments.

7.1.1 Al spectra in the range of 40-700 Å

The wide wavelength range, 40-700 Å, necessary to be covered by these spectral characterization studies necessitates taking many observations of the z-pinch spectrum along the Rowland circle of the spectrometer. This results in a mosaic of spectra that need to be stitched together. Figure 7.1 shows the result of creating a mosaic spectrum from the individually recorded spectra and different cord position along the Rowland circle.

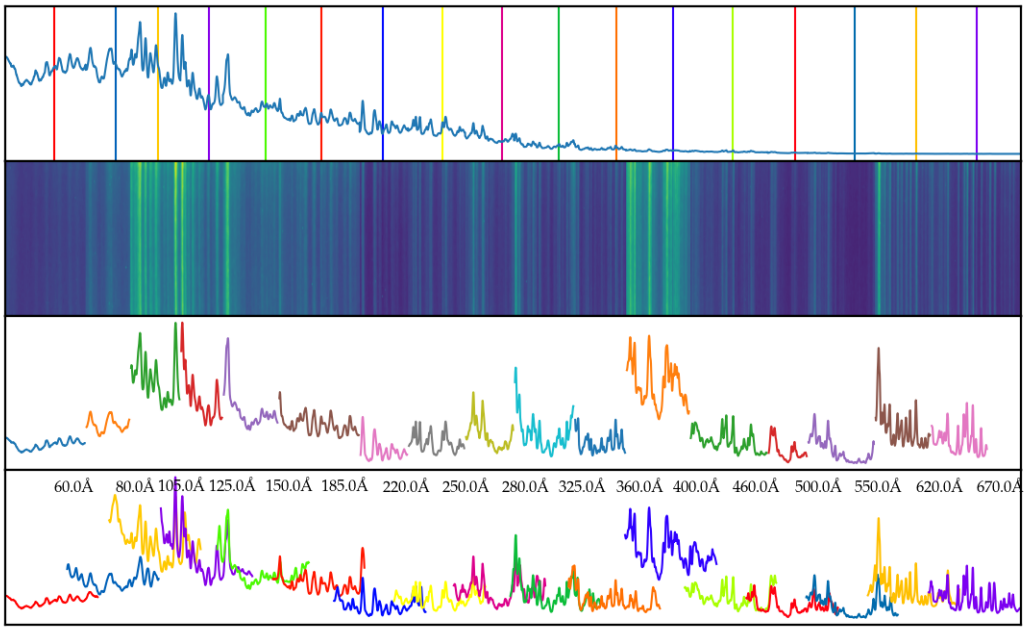

FIGURE 7.1: Example of mosaically stitched spectra from the summer 2020 campaign. 1st: Recorded spectra stitched together to show what the full spectrum would approximately look like if it were to be recorded all at once. 2nd: Final spectrum that results from stitching the spectra and matching the intensity at the stitch points. 3rd: The portions of the spectra that compose the final spectrum with the ends removed defined by the stitching. 4th: The individual spectra taken from each of the Zebra shots moving from high to low energy. These spectra have been aligned such that emission features from overlapping segments have been matched.

Starting at the bottom panel of Fig. 7.1, the individual spectra have been aligned such that overlapping emission features coincide between shots. The second panel from the bottom shows the resulting parts of each spectrum between the chosen stitch points. The 2nd from the top panel, shows the combined result of stitching the spectrum together and using the ratio of the intensities at the stitch points to scale the spectra. The top panel shows what the resulting spectra would be as if it were to be recorded all at the same time, without intensity matching at the stitch points.

7.1.2 Al spectra line identification

I had the great opportunity to explore the multitude of emission features with Haritha Hariharan, a fellow grad student. In the uncorrected form of the spectra in Fig. 7.1, the

spectra is much easier to investigate when it comes to identifying features. Haritha and I combed through the spectra using a combination of the NIST atomic database and PrismSPECT modeling to assist in the identification of line emission. Up to this point, Haritha and myself have had the most luck within the wavelength range 200–400 Å. In this range the aluminum ions found were C-, N-, O-, and F-like aluminum ions. Table 7.1 shows our combined effort to date of this writing.

An important note that should be considered is that these spectra are time integrated measurements. What this means, is that the spectrum includes aluminum emission from early stages of the pinch up through the implosion of the z-pinch and the stagnation phase. On top of the time integrated aspect of the spectra, the measurements are also spatially averaged over the length of the pinch. Thus, the information encoded in the spectra is a combination of multiple densities, temperatures, and charge states. Resulting in a complex spectrum that is challenging to detangle and understand.

7.1.3 Instrument corrections

In the mosaic form of Fig. 7.1 the spectral shape is starting to be revealed. However, the spectra needs several more corrections that are required in order to reveal the true spectral shape. Figure 7.2 shows the result of applying several corrections as well as the combined result. One correction that has been inherently applied from the beginning has been the CCD dark correction. This correction removes a lot of background noise and cleans up the spectra to a high degree. This is the starting point of the top panel of Fig. 7.2.

The grating correction may very well be one of the more important corrections to be applied. The grating efficiency is dependent on the optical coating and blaze will preferentially diffract a portion of the spectrum with higher efficiency than other portions. The efficiency of the grating is denoted by the dashed line. The result for the aluminum coated 600 l/mm grating is that longer wavelengths, lower energy, are reflected more

#	Ionization state	Ion	Iso	Lower	J_L	Upper	J_U	Å
1)	Al VII	Al^{+6}	N-like	$2s^22p^3$	3/2	$2s2p^4$	1/2	239.03
2)	Al VII	Al^{+6}	N-like	$2s^22p^3$	5/2	$2s2p^4$	3/2	240.77
3)	Al VI	Al^{+5}	C-like	$2s^22p^4$	2	$2s2p^5$	1	243.766
4)	Al VIII	Al^{+7}	O-like	$2s^22p^2$	2	$2s2p^3$	1	250.139
5)	Al VIII	Al^{+7}	O-like	$2s^22p^2$	2	$2s2p^3$	1	251.347
6a)	Al VII	Al^{+6}	N-like	$2s^22p^3$	1/2	$2s2p^4$	1/2	259.036
6b)	Al VII	Al^{+6}	N-like	$2s^22p^3$	3/2	$2s2p^4$	1/2	259.207
7a)	Al VII	Al^{+6}	N-like	$2s^22p^3$	1/2	$2s2p^4$	3/2	261.044
7b)	Al VII	Al^{+6}	N-like	$2s^22p^3$	3/2	$2s2p^4$	3/2	261.219
8)	Al IX	Al^{+8}	F-like	$2s^22p$	3/2	$2s2p^2$	1/2	305.055
9a)	Al IX	Al^{+8}	F-like	$2s2p^2$	5/2	$2p^3$	3/2	306.91
9b)	Al VI	Al^{+5}	C-like	$2s^22p^4$	2	$2sp^5$	1	307.249
9c)	Al IX	Al^{+8}	F-like	$2s2p^2$	3/2	$2p^3$	1/2	307.33
10a)	Al VII	Al^{+6}	N-like	$2s^22p^3$	3/2	$2s2p^4$	3/2	309.023
10b)	Al VII	Al^{+6}	N-like	$2s^22p^3$	3/2	$2s2p^4$	5/2	309.072
10c)	Al VII	Al^{+6}	N-like	$2s^22p^3$	3/2	$2s2p^4$	3/2	309.072
11)	Al IX	Al^{+8}	F-like	$2s2p^2$	1/2	$2p^3$	3/2	316.793
12)	Al IX	Al^{+8}	F-like	$2s2p^2$	3/2	$2p^3$	3/2	318.537
13)	Al IX	Al^{+8}	F-like	$2s2p^2$	5/2	$2p^3$	3/2	321.027
14)	Al VIII	Al^{+7}	O-like	$2s2p^3$	1	$2p^4$	0	340.23
15a)	Al VII	Al^{+6}	N-like	$2s^22p^3$	1/2	$2p^4$	3/2	343.290
15b)	Al VII	Al^{+6}	N-like	$2s^22p^3$	3/2	$2s2p^4$	5/2	343.641
16)	Al VII	Al^{+6}	N-like	$2s^22p^3$	3/2	$2s2p^4$	1/2	352.145
17)	Al VII	Al^{+6}	N-like	$2s^22p^3$	3/2	$2s2p^4$	3/2	353.145
18)	Al VII	Al^{+6}	N-like	$2s^22p^3$	3/2	$2s2p^4$	5/2	356.880

TABLE 7.1: Aluminum line emission features identified in the range 200–400 Å. From the line identification effort, C-, N-, O-, F-like aluminum ions are observed.

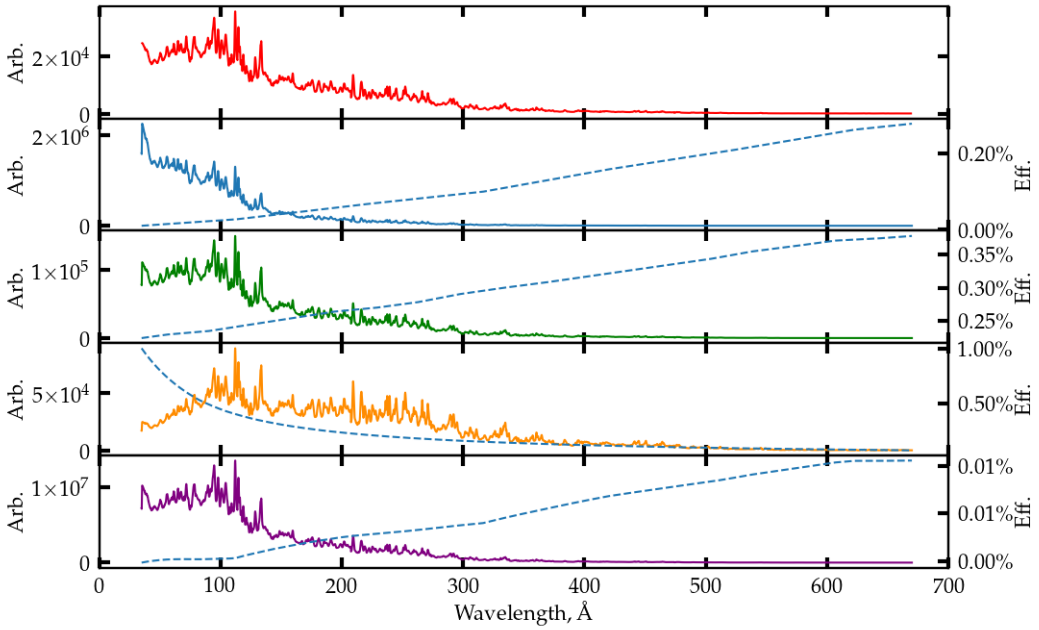

FIGURE 7.2: Recorded spectra stitched together to show what the full spectrum would approximately look like if it were to be recorded all at once.

efficiently and thus need to be reduced compared to that of the short wavelength high energy side which required a boosting of their relative intensity.

The third panel of Fig. 7.2 shows the result of the MCP response correction. Similar behavior to the grating correction, however much different in magnitude, the MCP detector responds more to long wavelength low energy than it does with the short wavelength high energy side.

The fourth panel of Fig. 7.2 shows a correction due to the effect of geometrical dilution of the radiation flux. Since the high energy spectra are much closer to the grating, the intensity of the spectra is larger by a proportionality factor of $1/r^2$ compared to that of the long wavelength low energy spectra. Differing from the previous two corrections, this correction has the effect of reducing the intensity in the short wavelength, high energy, side of the spectrum and bolstering the intensity of the spectrum towards longer wavelengths.

The combined result of all these corrections is shown in the fifth panel of Fig. 7.2. The composite efficiency curve represents an initial approximation to the total instrumental response. With the spectra now in this multiply corrected form one can begin to attempt to analyze the shape of the spectra to tease out details about the radiation drive.

7.1.4 Al spectra modeling: Radiation temperature analysis

With spectra processed with the relevant corrections in place, analysis of the spectral distribution can take place. The z-pinches driven by the intense current of Zebra are not true blackbody radiators, as they are transparent to UV diagnostics,[**Ivnov2016**, 32, 33]. However, they still to a degree exhibit similar characteristics. Figure 7.3 shows a Planckian fit to the aluminum spectra. This initial attempt to characterize the spectral distribution with a Planckian distribution provides compelling evidence that the Aluminum z-pinch produced by Zebra, is quasi-thermalized. The scaled Planckian fit results in a radiation temperature of $\sim$33 eV. A second, more approximate, method known as Wien's displacement law can be used. Wien's law relates the peak of a thermalized radiation source to the temperature of the blackbody radiator. Using this relation results in a radiation temperature of about 28.29 eV. The spectral peak was determined by smoothing the spectrum to reduce emission features, which are not characteristic of a thermalized radiation source. The r-squared value of the Planckian fit, however, lends credence to the partially thermalized nature of the aluminum z-pinch driven by Zebra.

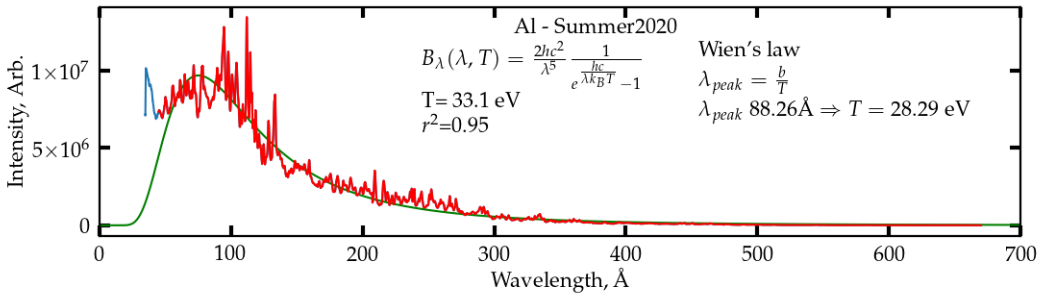

FIGURE 7.3: Initial effort at extracting a radiation temperature from the Al radiation drive recorded from the Summer 2020 campaign. Planckian fit estimates the radiation temperature T_R = 3.7 eV. Wien's Displacement law results in an estimated radiation temperature T_R = 28.3 eV

7.2 Summary

The results shown in this chapter document the initial effort of characterizing the spectral distribution of radiation drive of which Zebra is capable of producing. Characterizing a radiation source, such as a z-pinch is no small feat. There are a great many factors that contribute to the behavior of pulsed-power drivers that only add to the complexity of the load driven by the intense current.

Even though there is shot-to-shot variability, Zebra has shown to be remarkably stable and reproducible in the radiation fields produced. If Zebra varied more from shot to shot, fitting a Planckian would either not be possible or result in fits with poor r-squared values. Yet, as has been shown, the correspondence between experiment and theory is impressive. Providing compelling evidence that the z-pinch plasma is qausi–thermalized, with an approximate radiation temperature of ∼30 eV. This initial result will be used to guide future spectral characterization and inform modeling efforts.

Chapter 8

Experimental Results II: Photoionized supersonic gas jet experiments

The photoionized supersonic gas jet experiments were carried out with the ∼1MA Zebra accelerator. This new approach demonstrates for the first time a platform that unlocks the laboratory ability to generate and investigate astrophysically relevant photoionized plasmas utilizing university-scale pulsed-power generators. Further, the platform has accomplished for the first time, simultaneous multi-diagnostic multi-perspective interrogation of astrophysical laboratory photoionized plasmas. The data observed and collected from these experiments are complementary to that of the data acquired from photoionization experiments on Z[2, 21, 46, 50, 49] and Omega-EP[62]. While some of the results make for a clear comparison between the Zebra experiments and the others, the experiments on Zebra push beyond any of the other experiments in the use of advanced laser diagnosis. In tandem to the spectroscopic measurements, multi-color laser interferometry, and shadowgraphy illuminate spatial characteristics that have been hidden under a veil of spatially averaged measurements. In a finality of many firsts, due to Zebra's flexible ceaseless operative capability, these experiments, even in their infancy,

show shot-to-shot reproducibility which establish the supersonic gas jet platform on Zebra as a powerful experimental methodology for laboratory astrophysics.

The photoionization of the gas jet during the Zebra shot was studied via three independent diagnostics: Two air-wedge shearing interferometers, at wavelengths of 532 nm and 266 nm, and a KAP crystal X-ray spectrometer. These three diagnostics independently measure areal and volumetric electron density. Note, the measurements made from interferometry are 150 ps duration laser pulses, which are timed to be coincident with the peak of the X-ray pulse. While, the X-ray absorption spectrum recorded on the X-ray film is integrated over the duration of the 25-35 ns X-ray pulse. Second, the area observed between the interferometers and the spectrometer are also different. The interferometers view the entirety of the photoionized plasma from the vertical perspective. Whereas the KAP spectrometer field of view is highly localized to a small 300 μm slice of the gas jet. The temporal difference and spatial differences should be kept in mind for the upcoming comparisons between these two measurements. As well, the area investigated by these two diagnostics is very different. The interferometry views the entirety of the plasma; while spectra recorded is the result of a thin slice of plasma backlit by micro-pinches in the plasma.

8.1 Initial verification of photoionization

A critical question in the beginning of these experiments was, in what ways can we confirm photoionization of the gas jets? A critical question being that these gas jets are situated between a 2 MV potential. It would be difficult to use spectroscopy solely for initial confirmation of photoionization versus collisional ionization. If the nozzle and by extension the jet were placed in a manner that allowed current to jump into the jet how would one know definitively with spectroscopy analysis? Depending on the field of view (FOV) of the spectrometer, the results could be ambiguous. Certainly, if the spectrometer FOV was aligned directly at the location of the jet in which the

current jumped into, the areal electron density calculation and the charge state analysis would be unmistakable. However, for instance, if current jumped into the jet close to the nozzle and the spectrometer FOV was further up the jet the conclusions may not be so conclusive one way or the other. This task was effortlessly and quickly handled with the aid of laser diagnostics such as shadowgraphy and primarily air-wedge interferometry which easily answered this question.

With the laser diagnostics employed in the gas jet platform, spatial resolution was a valuable tool for quick visual diagnosis of the photoionization of the gas jet. A classic example of swift qualitative, bordering on quantitative, visual verification using 532 nm air-wedge interferometry is presented in Fig. 8.1. The left image of Fig. 8.1 is a reference shot taken before the Zebra shot and the right image is a snapshot of the photoionization of a nitrogen supersonic gas jet with 400 psi backing pressure driven by the x-ray flux produced by the implosion of a gold 8-wire array z-pinch. The original shape of the nozzle is denoted by the orange dashed line and the photoionized gas jet can be located by the oblong oval-esque perturbed fringe lines above the nozzle near the location markers 1 and 2. The location of the z-pinch is denoted via the red dashed line and location marker 3.

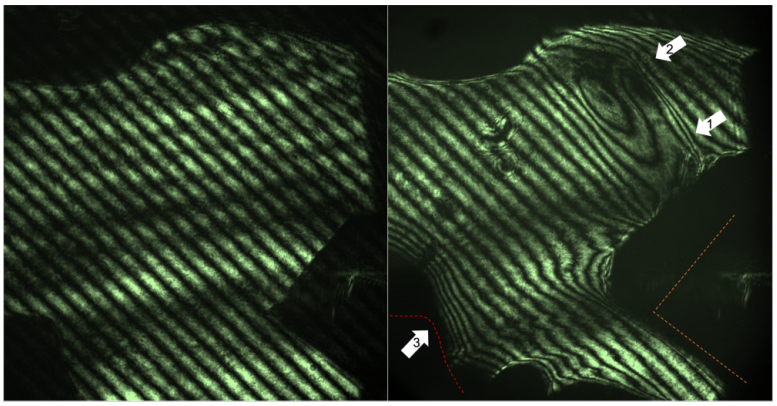

FIGURE 8.1: Air-wedge interferometry, 532 nm, of a nitrogen gas jet with 400 psi backing pressure, irradiated by the implosion of a gold 8-wire array z-pinch. Left image: Shows the reference image before the Zebra shot. Right image: Shows the photoionization of the gas jet. A penumbra effect results in non-uniform photoionization of the jet, which can be seen by comparing locations 1 and 2 denoted by the white arrows.

What makes Fig. 8.1 such an exquisite example is that the time it takes to understand what has occurred is primarily bottle necked by the time it takes to throw open the screen door for the laser diagnostics box. The first thing we look for, is the location above the nozzle to see whether there is strong deviation of the fringe lines. If there is like we see in Fig. 8.1, the next we gleam from such an image, simultaneously, is whether or not we observe any form of current discharge or "arching" from the surrounding load hardware and/or current return cage leading to the nozzle and/or jet.

By looking deeper into Fig. 8.1 there is more to be grocked[1]from the image on the right. Interferometry like what is shown in Fig. 8.1 and the rest of the work in this dissertation, can be analogized to topography maps... topophase maps if you will. If we take this perspective and apply it to the image on the right, specifically to the region that gas jet is located, we notice that locations pointed at by markers 1 and 2 have different topophase characteristics. The location pointed by marker 2 looks like a peak, a phase peak, whereas the location marked by marker 1 looks less steep and to be at the base of the phase peak. What we are seeing here is the effect of a shadowing of the x-ray flux by the nozzle and a small metal shield that extended off of the left side of the nozzle. The angle of the nozzle compared to the location of the pinch and the metal shield created a penumbra zone in the region denoted by marker 1. This region near the top of the nozzle experienced less x-ray flux compared to the region further away denoted by marker 2, and as a consequence resulted in less photoionization. This difference is electron density between these two locations and the gradient connecting them demonstrates unequivocally the photoionization of the gas jet.

[1]grok, v. /graak/ | /rk/ 1. transitive (also with object clause) To understand intuitively or by empathy; to establish rapport with. [66] 2. a complete, deep, intuitive understanding of a particular subject. 3. to understand so thoroughly that the observer becomes a part of the process being observed[23]

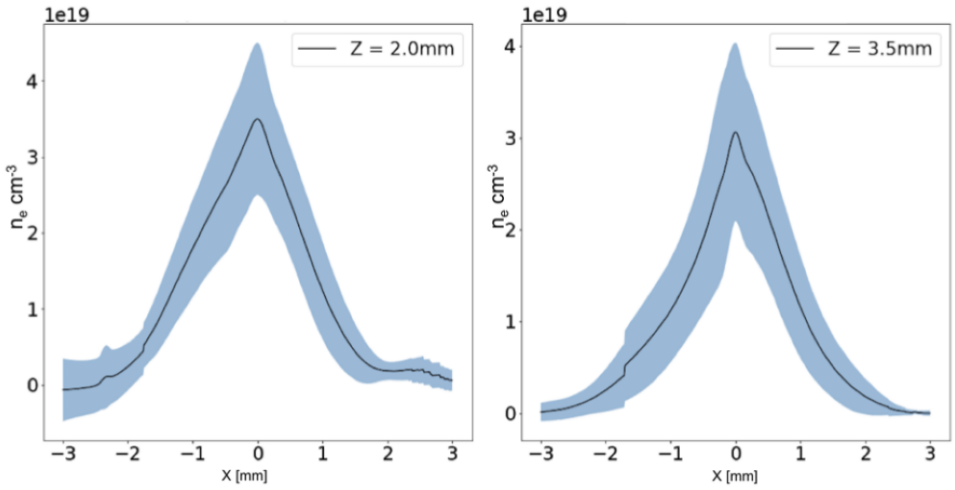

FIGURE 8.2: Average electron density radial profiles at z = 2.0 mm and 3.0 mm along the gas jet axis (left and right respectively). Electron density profiles extracted from interferometry. The blue shaded region represents the standard deviation between measurements.

8.2 Trends in spatial electron density measurements

While this qualitative approach is certainly helpful, *especially in the lab*, we can go further by extracting quantitative data from these interferograms. By extracting the phase information folded and tucked into the fringe lines, we can extract areal electron density and volumetric electron density that give "big picture" understanding of the photoionization of the gas jet.

Figure 8.2 shows two electron density profiles averaged over several shots at 2.0 mm and 3.0 mm along the photoionized neon jet. There are several items of interest to take away from these plots. First is that as discussed earlier, the side of the jet(right side) near the pinch is a much cleaner measurement. This is because the load hardware ablates and produces an electron density cloud above and below the gas jet in the line of sight of the laser diagnostic. This is clearly seen by comparing the left side to the right side in Fig. 8.2. Second, is that while there is a decrease in the peak electron density from 2 to 3 mm along the jet axis, the electron density is fairly stable.

An interesting measurement that was made possible by automating the interferometric

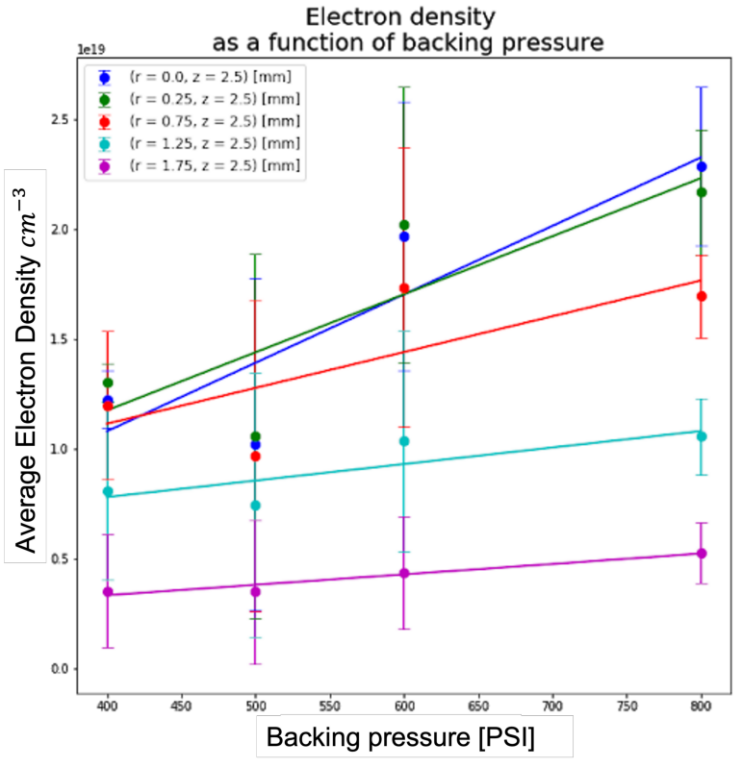

FIGURE 8.3: A plot showing the average electron density as a function of backing pressure. Average electron density trends are shown for radial positions 0.0, 0.25, 0.75, 1.25, 1.75 mm at 2.5 mm away from the nozzle.

analysis, was looking at trends with regards to pressure and machine current. Figure 8.4 shows a plot in which electron density was queried from many electron density maps in order to be plotted as a function of backing pressure and several distances from the gas jet axis at a point 2.5 mm in the gas jet away from the nozzle. This plot shows that even though one must contend with Zebra's jitter and varying peak currents delivered to the load and the uniqueness of each wire-array, there is a clear trend in electron density with backing pressure and distance from the central core of the gas jet axis. One aspect that is difficult to nail down precisely is the central region of the photoionized gas jet. This can be seen by the ambiguity in the traces for r = 0.0 mm and r = 0.25 mm, the blue and green traces respectively.

Figure 8.4 shows a trend between electron density at different locations at various radial positions and the relative strength of the current. This trend while being a bit more

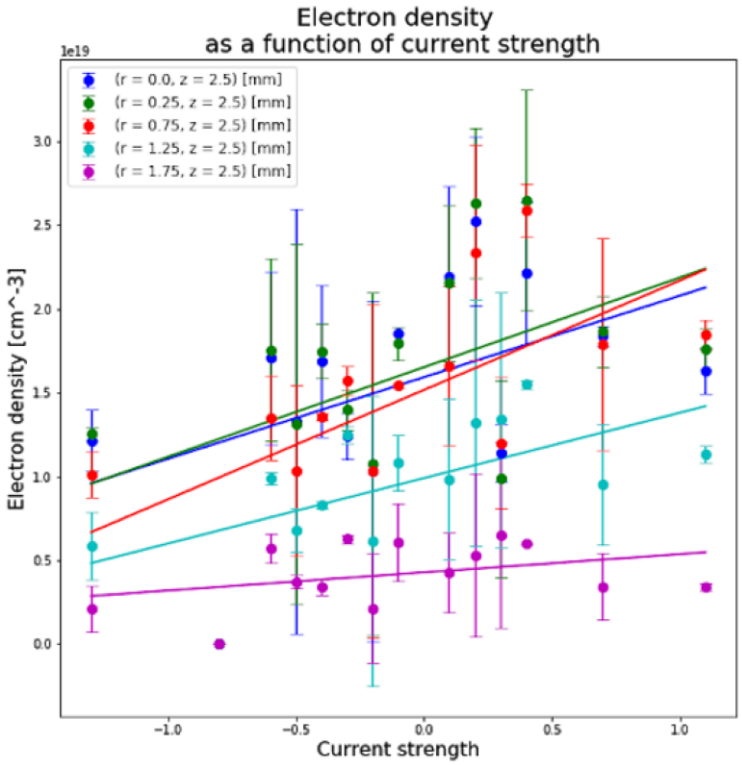

FIGURE 8.4: A plot showing the average electron density as a function normalized relative peak current, aka "current strength". A current strength of 0 represents the average peak current 0.9<1 MA of backing pressure. Average electron density trends are shown for radial positions 0.0, 0.25, 0.75, 1.25, 1.75 mm at 2.5 mm away from the nozzle.

messy than the ones shown in Fig. 8.3 still shows strong significance, considering all of the variability that occurs from shot to shot. Similar trends are found as those found in Fig. 8.3. The electron density measured within the photoionized gas jet increases systematically with current strength, as well as increases in density radially.

8.3 Transmission spectra

An averaged spectrum from four different shots is presented in Fig. 8.5. The four different shots include two spectrums from neon jets with 200 psi backing pressure, the third spectrum comes from a neon jet with 400 psi backing pressure, and the fourth spectrum comes from a neon jet with 600 psi backing pressure. From this averaged

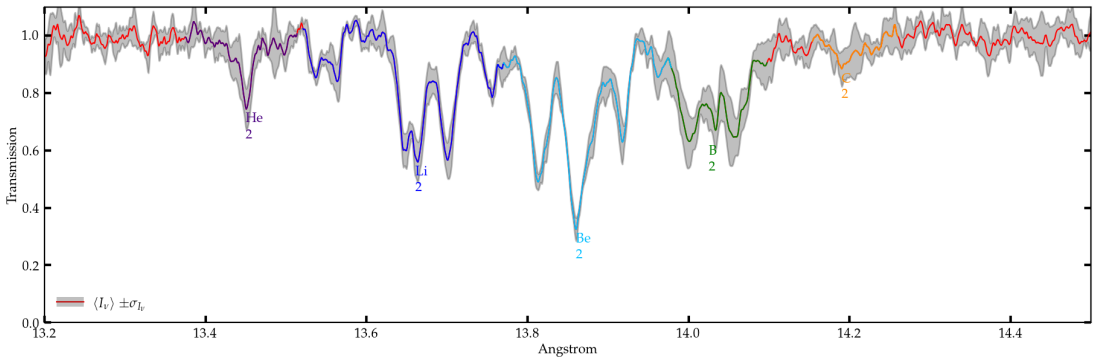

FIGURE 8.5: X-ray absorption spectrum averaged from four separate shots, composed of two shots with 200 psi, one shot with 400 psi, and one shot with 600 psi.

spectrum we can recognize the main contributing neon ions, C-, B-, Be-, Li-, and He-like neon.

At first inspection one may consider the locations of large variability, i.e. the B-like and C-like neon absorption features, to be due to density sensitivity. Figure 8.6 shows each of the four spectra plot together as well as individually. If we look at the individual spectra compared to the averaged spectra in the subplots of Fig. 8.6 we note that the large variance of the B-like neon absorption feature stems from the variability in the 200 psi neon spectra.

Figure 8.7 focuses solely on the two shots of 200 psi neon. What we learn from this focused perspective is that with the backing pressure constant, the variability in B-like, C-like, and He-like must be due to some other factor. The most likely factor is the x-ray drive. The shot to shot reproducibility of the radiation drive can stem from a variety of factors, the main two being the uniqueness of the wire-array and current drive through the array. One avenue of future work will be to use all of the data gathered to average out shot to shot variation to see the true characteristics of particular gas jets at specific backing pressures.

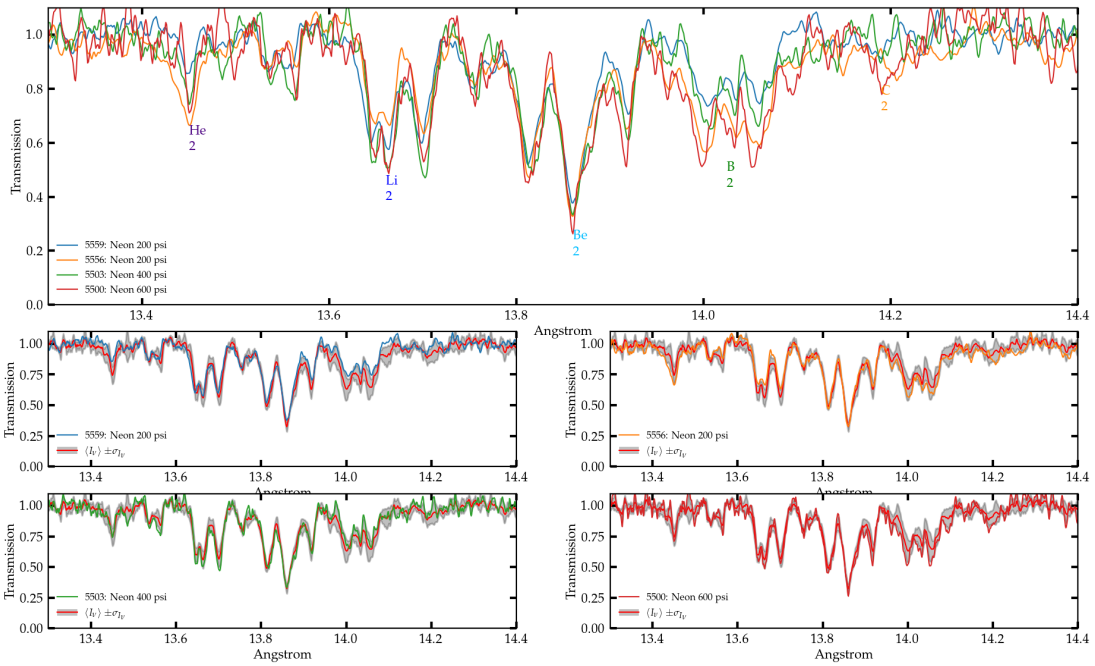

FIGURE 8.6: X-ray absorption spectrum from four different shots. Two shots with 200 psi, one shot with 400 psi, and one shot with 600 psi.

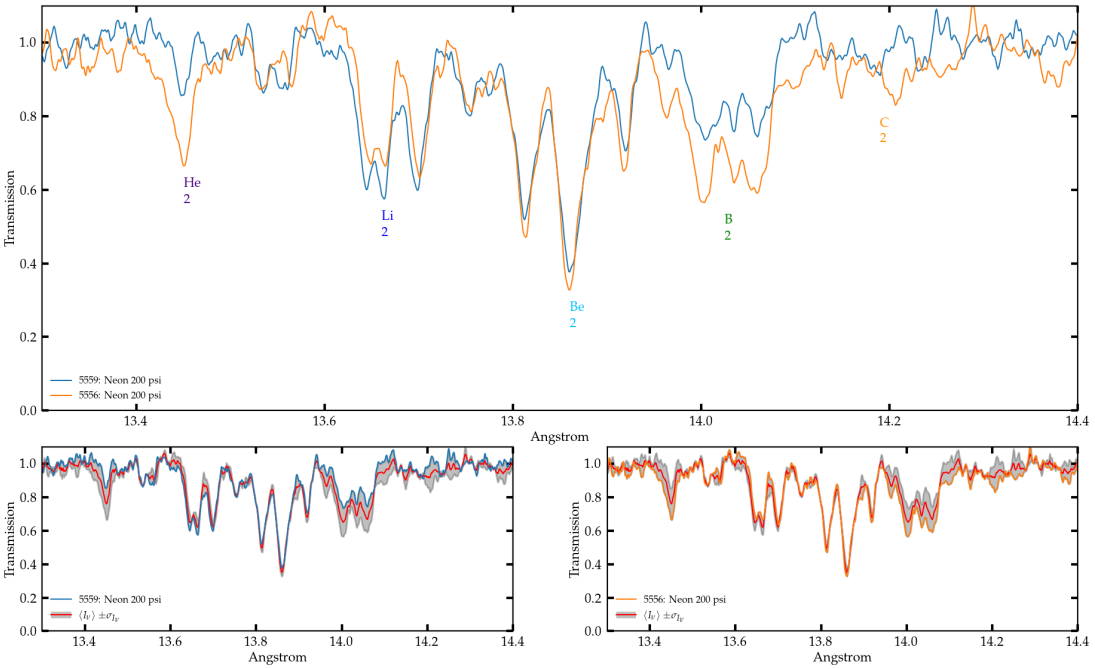

FIGURE 8.7: X-ray absorption spectrums two separate shots with 200 psi neon.

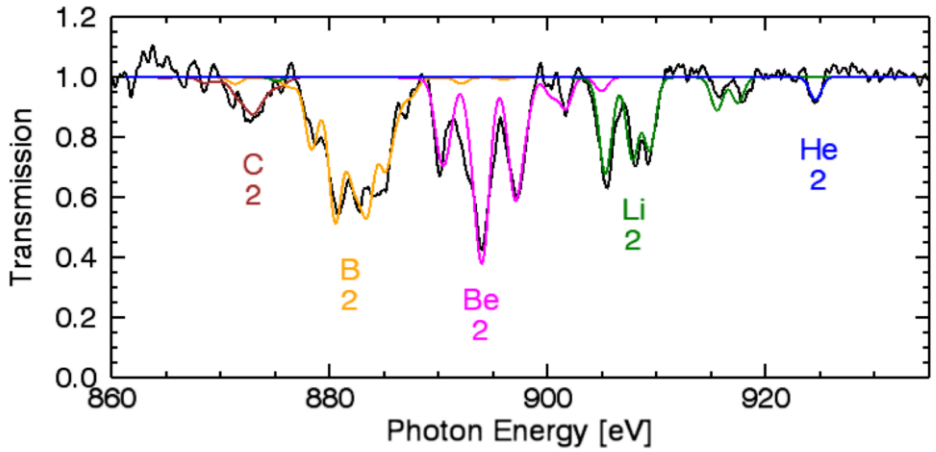

FIGURE 8.8: X-ray absorption composition from four different shots two with 500 psi and two with 600 psi. The color traces that overlay the spectrum represent the calculated fits done for the analysis of the spectra. The number under the label denotes the upper level of the transition. Spectroscopy data: (#5073 (600 psi), #5077 (500 psi), #5078 (500 psi), #5080 (600 psi))

8.3.1 Areal Ion and Electron Density

Several transmission spectra for neon with backing pressure 500 and 600 psi have been processed and analyzed by Dan Mayes. [48] An average transmission spectrum for these four spectra is shown in Fig. 8.8. The fitting of the C-, B-, Be-, Li-, and He-like neon are shown overlaid on the averaged transmission spectrum. The fractional population that results from this spectral analysis is shown in Fig. 8.9. Based on the analysis of these absorption features we see that the bulk of the fractional ion population is found in the B-, Be-, and Li-like neon ions, characterized by an average charge state, $\bar{Z} = n_e/n_a$, of 5.8. While, the C- and He-like neon populations, which are not very prominent, bound either side of the fractional ion population distribution.

Based on the two fractional neon ion populations that bound the fraction ion distribution, C- and He-like, we can get a broad understanding of the radiation drive delivered from Zebra. By consulting Table 8.1 we see that the ionization potential for C-like neon is 126.21 eV. Since a minor amount of C-like neon is present, this insinuates that the

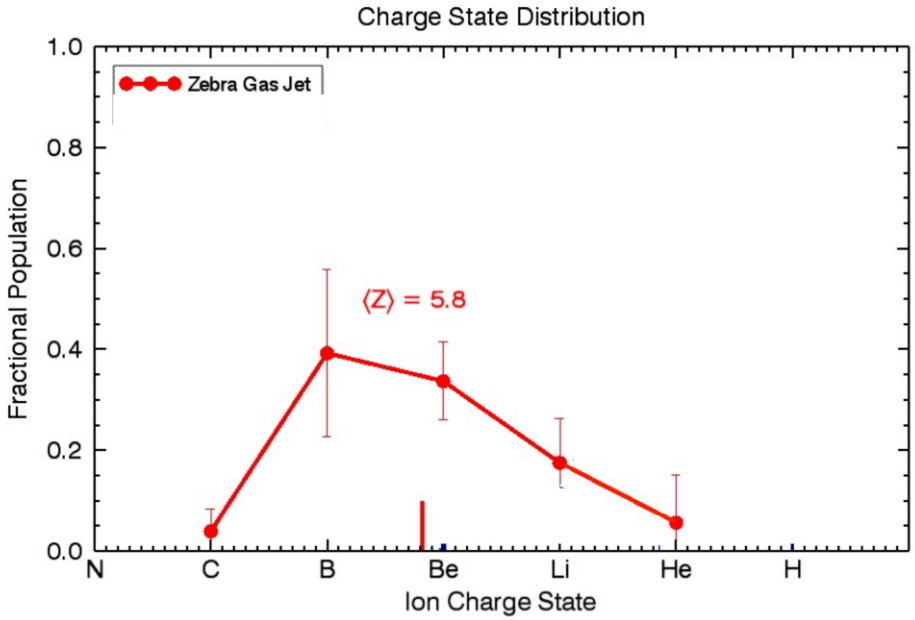

FIGURE 8.9: Fractional ion population of photoionized neon from the photoionized supersonic gas jet experiments on Zebra.

radiation drive clearly burns through the neon ions up through N-like neon. Next, by consulting Table 8.1 again, this time for He-like neon, we find an ionization potential of 1195.797 eV. Since the radiation drive barely populates the He-like neon population we can infer that the tail end of the radiation drive tops out around here.

We can dive further into the results of this spectral analysis by examining the ion areal densities. The ion areal density, $N_i L$, is found by χ^2 fitting of the transmission spectra (Fig. 8.8) which can be expressed via the equation for transmission,

$$T_\nu = e^{-\tau_\nu}, \tag{8.1}$$

where ν parameterizes spectral distribution, τ_ν is the total optical depth for spectral frequency ν. The total optical depth, τ_ν, is the sum of the present neon-ion optical depths,

$$\tau_\nu = L \cdot \Sigma_i \sigma_{\nu i} N_i, \tag{8.2}$$

Z (Element)	I	II	III	IV	V	VI	VII	VIII	IX	X
1 H	13.598									
2 He	24.587	54.416								
3 Li	5.392	75.638	122.451							
4 Be	9.322	18.211	153.893	217.713						
5 B	8.298	25.154	37.930	259.368	340.217					
6 C	11.260	24.383	47.887	64.492	392.077	489.981				
7 N	14.534	29.061	47.448	77.472	97.888	552.057	667.029			
8 O	13.618	35.116	54.934	77.412	113.896	138.116	739.315	871.387		
9 F	17.422	34.970	62.707	87.138	114.240	157.161	185.182	953.886	1103.089	
10 Ne	21.564	40.962	63.45	97.11	126.21	157.93	207.27	239.09	1195.797	1362.164

TABLE 8.1: Ionization potentials in eV for hydrogen through neon and their respective ion-like counterparts. Values retrieved from the CRC handbook[22]

where the sum is over ions i in the plasma, $\sigma_{\nu i}$ is the absorption cross-section for i^{th} ion in units of cm^2, N_i is the number density, cm^{-3}, for the i^{th} ion, and L is the length of the chord through the plasma observed via the spectrometer. The i^{th} ion areal density is given by the product of the chord length multiplied by the volumetric ion density, LN_i cm^{-2}.

8.4 Interferometry and Spectroscopy Comparison

8.4.1 Areal density comparison

Correlation can be observed between, independent diagnostics, air-wedge interferometry and x-ray absorption spectroscopy; which observe the photoionized plasma operating with entirely unrelated principles. Figure 8.10 shows a comparison of a multi-shot average of areal electron density results extracted from interferometric and spectroscopic measurements. The vertical double-headed red arrow, in Fig. 8.10, marks the areal electron density range extracted from the x-ray absorption spectroscopy measurements. The horizontal arrows show the width of the photoionized gas jet measured from the x-ray film. The black trace in Fig. 8.10 is the multi-shot average of four separate Zebra shots, totaling 7 separate interferograms. The areal electron density profiles were taken at position 3 mm from the nozzle tip avoid nozzle ablation, seen in Fig. 5.29, while remaining within the main region of interest of the supersonic photoionized gas jet. The

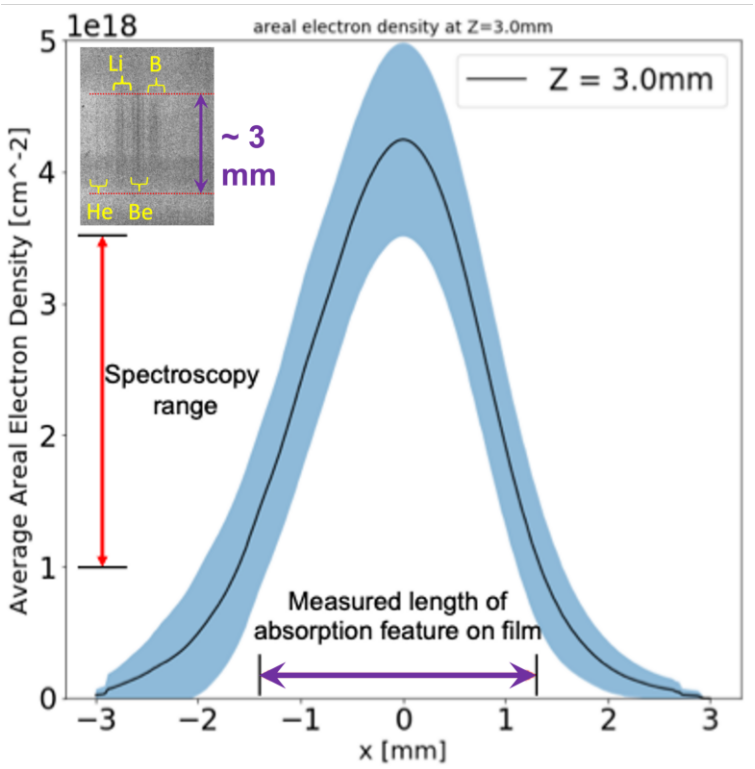

FIGURE 8.10: Comparison of multi-shot average of areal electron density extracted from interferometry and x-ray absorption spectroscopy. Averaged areal electron density result from air-wedge interferometry(black-trace) with standard deviation(blue shaded region). Averaged areal electron density from x-ray absorption spectroscopy(Vertical red arrows). Average measured length of photoionized gas jet(Horizontal red arrows). Interferometry data: (#5072, #5073, #5077, #5080) Spectroscopy data: (#5073, #5077, #5078, #5080)

shaded blue region represents the standard deviation. Areal electron density extracted from x-ray absorption spectroscopy is in the range of 1.0–3.5$\times 10^{18} cm^{-2}$, denoted by the red. These values fall within the range of areal electron density values extracted from air-wedge laser interferometry, with peak areal electron density $\sim 4.0 \times 10^{18} cm^{-2}$.

8.4.2 Average Charged State

The average charge state, $\bar{Z} = n_e/n_a$ historically has been a value only calculated from spectroscopic analysis. For what may be one of the first times, the average charge state has been calculated solely from interferometric measurements. Figure 8.11 shows

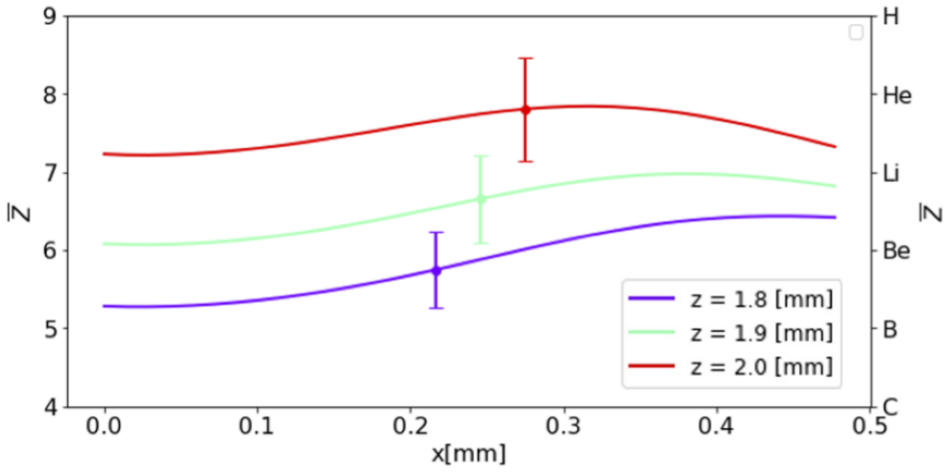

FIGURE 8.11: Spatially resolved average charge state of 800 psi photoionized neon supersonic gas jet.

spatially resolved charge states for a $0.5\ mm^2$ region of photoionized neon plasma. The values in Fig. 8.11 were produced by dividing spatially resolved measurements of electron density by spatially resolved measurements of atomic density. Thus, the average charge state traces are plotted as a function of radius for three positions along the gas jet. Such a measurement required the use of two different types of interferometers, a Mach-Zehnder interferometer for measuring the atomic density of the gas jet before the Zebra shot and a differential shearing air-wedge interferometer.

The average charge state has an increasing behavior along the gas jet axis, away from the nozzle. This increasing trend of $\bar{Z}$ is not initially obvious, however when we take into consideration that the spatial characteristics of the relevant gas jet properties and radiation flux this trend can be understood. The first part of this complex behavior to understand is the decreasing behavior of the atomic density away from the nozzle along the gas jet. Since, the atomic density decreases along the gas jet, the electron density naturally decreases as well along the axis of the gas jet. The second factor that ties this intricate relationship together is that the ionizing X-ray flux decreases due to geometric dilution. Since the end of the gas jet is further away from the pinch, the x-ray flux decreases as well along the gas jet axis. While both atomic density and electron density

decrease along the gas jet axis, the electron density decreases at a slower rate than the atomic density. This delicate balance of atomic and electron density with the x-ray flux is what leads to an increasing $\bar{Z}$ leading along the axis of the gas jet away from the nozzle. Since there is a decrease in the atomic density and thus the electron density leading away from the nozzle, collisional effects of the electrons are diminished. [50] This reduction in electron collisions creates a spatial distribution of less energetic electrons as function of distance from the nozzle. This distribution of decreasing energetic electrons gives rise to more recombination away from the nozzle and thus minimal ionizing effects. It is in these regions with low atomic density that photoionization becomes more prevalent than recombination, which leads to higher charge state values.

The results from these interferometric measurements show that the neon plasma in this spatial region is as well dominated by Li-like, Be-like, and B-like neon ions. The nature of these measurements, being average charge state measurements and spatially averaged infer that He-like C-like neon ions should be present as well. The total average charge state for this, $\sim$0.5 mm^2 region of the plasma is $\sim$6.7$\pm$0.9.

While the principles behind the interferometric measurements and the spectroscopic measurements are entirely different, the results are very much in agreement. Both analyses suggest a photoionized neon plasma dominated by B-, Be-, and Li-like neon plasma. Further, both as well suggest that C- and He-like neon ions are present. The only main difference between the two independent forms of charge state analysis is the total averaged charge state. The spectroscopic analysis results in $\bar{Z}$=5.8 while the interferometric analysis results in a value $\sim$6.7$\pm$ 0.9. Which begs the question, why are these two results different when their results up to this point are so similar? One could use the uncertainty as a way to explain this away, however, we can do better. Remember, the spectroscopic measurements are integrated over the duration of the x-ray pulse, while, the interferometry is timed to be coincident with the peak of the x-ray pulse. Viewed from this perspective, it is consistent that the interferometry would be interrogating the photoionized neon plasma at its most ionized, state, resulting in

higher average charge state values.

8.5 Summary

The successful implementation of the gas jet platform in conjunction with the plethora of diagnostics has been shown in detail. The electron density of these photoionized plasmas was calculated via Abel inversion of the phase maps extracted from the air-wedge interferograms. Peak electron density measurements of the photoionized plasmas are of the order $2 \times 10^{19} cm^{-3}$. Further, we have shown that the laser interferometry and X-ray transmission spectroscopy are consistent with each other. Laser interferometry measures electron areal density values $(1.0 - 4.0) \times 10^{18} cm^{-2}$. While, electron areal density calculated from the X-ray transmission spectroscopy are in the range $(1.0 - 3.5) \times 10^{18} cm^{-2}$.

The ionization balance was as well investigated using diagnostic operating on independent physical principles. The analysis of the data collected from these measurements were in agreement, showing a photoionized neon plasma composed of B-, Be-, and Li-like neon. As well, based on these analyses, both spectroscopy and interferometry show the presence of C- and He- like neon bounding the bulk of the neon ion populations. Furthermore, what may be an even stronger indication of the agreement between the two forms of diagnostics is the average charge states measured. The time integrated measurement from the x-ray absorption spectroscopy resulted in a total average charge state of $\bar{Z}$=5.8. Which is less than the interferometric measurement of $\bar{Z}$=6.7$\pm$0.9; a measurement that should be larger due to the very nature of this 150 ps snapshot near the peak of the x-ray flux, when the neon plasma is at its most ionized and energetic.

These initial results demonstrate measurable reproducibility while factoring in the shot to shot variability of Zebra's performance. Now that this platform has been developed, systematic data can be continued to be collected. Results from these experiments and future ones will provide a new source of data to benchmark atomic kinetics codes and

astrophysical codes. As well, these experiments will further investigation into radiative properties of photoionized plasmas.

Chapter 9

Experimental Results III: Photoionized gas cell

The photoionized gas cell experiments on Z have evolved over time and have produced very interesting results. With each new data set comes further understanding of the plasma formed within the gas cell. The techniques developed by Dan Mayes to processes and analyze the x-ray absorption spectra recorded are of the highest order, from which I am grateful to benefit. However, the phenomenological world does not give up its secrets easily.

First we will look at examples of x-ray transmission spectroscopy from some of the most recent gas cell experiments that compromise the generation III data set. We will explore the analysis of one transmission spectrum. From this we will only scratch the surface of what is possible. This example will also introduce an oddity within the transmission analysis that as of yet has no explanation.

Second, the first results of the integration of the photon Doppler velocimetry (PDV) diagnostic are presented. We will begin with developing confidence in this new diagnostic by reviewing the adverse radiation noise characterization and the null shot that was a gas cell fielded without any gas. We will see that effort to mitigate radiation noise was

highly successful. As well, the results from the null shot provide interesting insight and confidence in the measurements made with gas fill.

With the PDV system characterized we will dive into the PDV results, highlighting never before seen observations, early in time as well as around the peak of the x-ray pulse. Diving further into the results, a comparative analysis of two nominally identical shots fielded with 15 Torr neon fill pressure, will be shown. These two shots have strikingly similar evolutionary characteristics, to such a degree that we see several forms of reproducibility.

Following the analysis of the PDV experimental data, radiation hydrodynamic simulations of the experimental conditions will be presented. This is the first time that simulated electron density time histories have been compared to experimental data, a true apples to apples comparison.

The PDV results discussion will finish with a brief presentation of the first gas mixture shot observed with PDV. A gas cell with a 50:50 mix of neon and argon with 60 Torr filling pressure was fielded in the far position. In this shot, we find similar trends to that of the neon only 15 Torr shot as well as stark differences. Both the similarities and differences found further support initial cases for reproducibility.

9.1 X-ray absorption spectroscopy

Historically the main diagnostic for these experiments has been the TREX spectrometer. Typically fielded with elliptically bent KAP crystals used to observe neon K-shell line absorption in the range of 850–1250 eV(Fig. 9.2). In the following sections neon transmission spectra will be presented from several shots that compromise the latest gas cell generation. As well, results from an argon absorption feasibility test were conducted using an elliptically bent PET crystal. The initial results of which are shown and discussed.

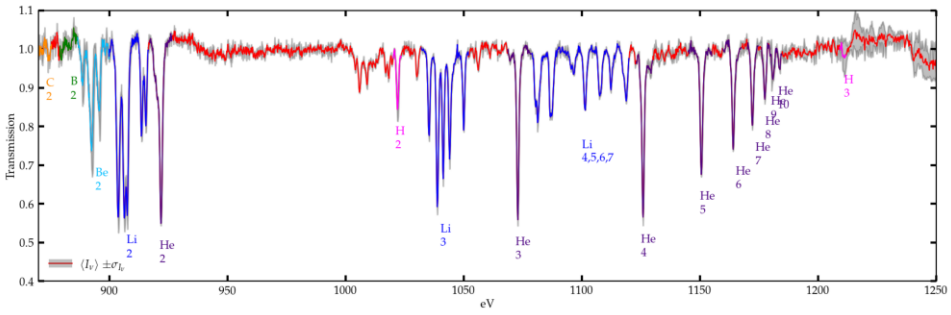

FIGURE 9.1: Averaged neon spectra of 30 Torr neon (Z3529, Z3532)

9.1.1 Generation III

The main spectroscopy objective was to further fill out the generation III dataset. The gas cell generations are defined by average machine current, style of return current canister, window material, and gas cell geometry(see Table 6.1). The datasets within these generations are parameterized by fill pressures and the incident x-ray flux irradiating the cell. Thus, there are a variety of parameter combinations that can be used to modify the ionization parameter, $\xi \propto F/n_e$. By modifying these parameters, changes in radiation flux and/or initial gas density, that the relative importance of electron- and photon-driven atomic processes are augmented. These changes will directly affect the atomic kinetics and the heating of the plasma. Figure 9.2 shows various neon spectra with 15 and 30 Torr fill pressures and one with a 60 Torr 50:50 neon/argon mixture, all fielded in the far position on the anode plate.

9.1.1.1 Neon, 15 Torr, far position

From the analysis of the transmission spectra, properties of the plasma such as the fractional ion populations and electron temperature can be determined. The initial analysis of the time integrated transmission spectra of shot Z3607, Fig. 9.3, reveals an electron temperature T_e=24.29$\pm$3.41 eV. A value that compares well with previous experiments fielding neon with 15 Torr of filling pressure in the far position. This temperature has been inferred by taking the ratio of populations from two Li-like neon configurations,

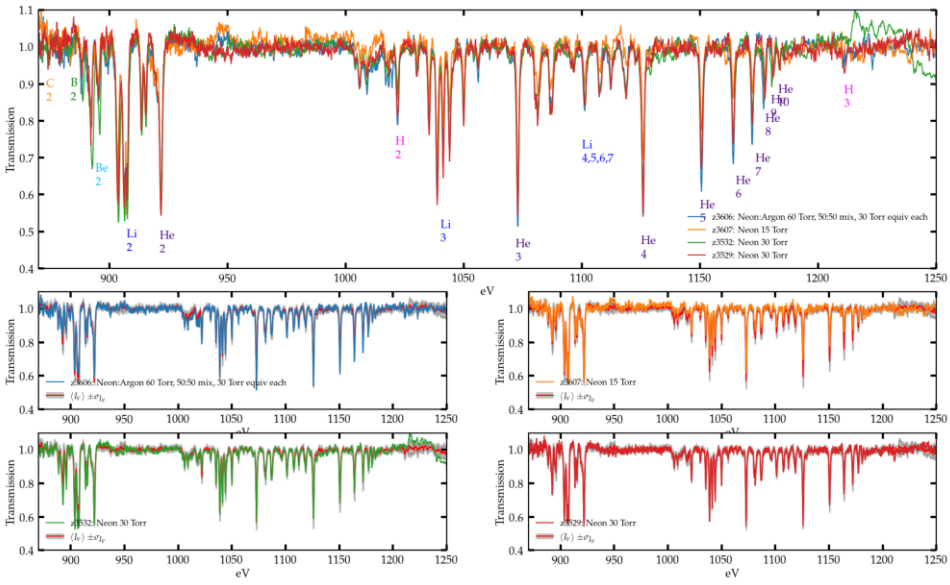

FIGURE 9.2: 30 Torr neon (z3529), 60 Torr Neon:Argon 50:50 mix equivalent to 30 Torr of neon and argon (Z3606), 15 Torr neon (Z3607)

specifically that of $1s^2 2s$ and $1s^2 2p$ [46]. The important point here is, if the relative populations of these Li-like energy levels are close to local thermodynamic equilibrium, then the ratio of their populations can be well approximated with Boltzmann factors. As shown by the Ph.D. work of Dan Mayes the temperature can be found in the following manner,[50]

$$R = \frac{N_p}{N_s} = \frac{g_p}{g_s} e^{\frac{\Delta E}{kT_e}} \Rightarrow kT_e = \frac{\Delta E}{\ln(g/R)}. \tag{9.1}$$

Here the Boltzmann factor R is equated to the ratio of the $1s^2 2s$ and $1s^2 2p$ populations, N_s and N_p respectively, the statistical weights of the configuration are $g_p = 6$ and $g_s = 2$, and the difference in energy between these two levels is $\Delta E = 16.025\, eV$.

The fractional neon-ion populations necessary for the above temperature calculation are extracted from the analysis of the transmission spectrum. This is done by calculating areal densities of each ion by fitting the spectral line shapes of the spectrum. For shot Z3607 the fractional ion population is dominated by He-like with about 48% of the neon ion population. Li-like neon is the next most abundant with population percentage about half of the He-like, 21% of the population. Be-like only amounts to 2% of the

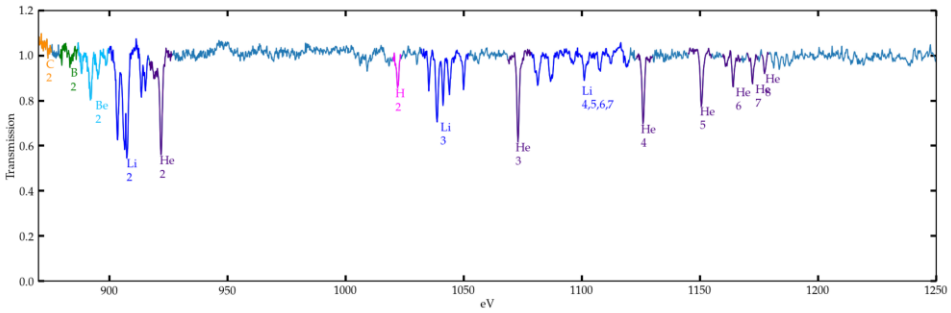

FIGURE 9.3: X-ray transmission spectrum recorded from the photoionization of a neon gas cell with 15 Torr of gas fill fielded in the far position, from shot Z3607

neon ion population. In terms of significance, H-like barely contributes to the overall population just shy of 1%. The fractional populations presented only constitute 72% of the total fractional population. This leaves us with a question, where is the remaining 28%? A question that Dan's PhD work goes into detail and has motivated the need for alternative diagnostics.

9.1.2 Argon Feasibility Test

An important, *necessary*, evolution of the photoionized gas platforms, like the gas cell and the gas jets, is the ability to support gas mixtures. Photoionized plasmas found in these astrophysical environments out in the great reaches of space are inherently multi-element plasmas. Such plasmas are of course much more complicated to interpret and thus represent an expanded frontier of laboratory photoionized plasma studies.

To this end, a feasibility test of photoionized argon was conducted. A 50:50 gas mixture of neon and argon was fielded with 60 Torr in the gas cell, in the far position on the anode plate. The fill pressure of 60 Torr was chosen such that the neon and argon gas had 30 Torr of equivalent pressure each. In this way, 30 Torr neon absorption spectra could be compared with the neon absorption spectra from the neon argon mixture shot. For this gas mixture shot as well as the null shot, TREX was configured such that side A was fitted with a PET crystal while side B used a KAP crystal, with both sides recording time

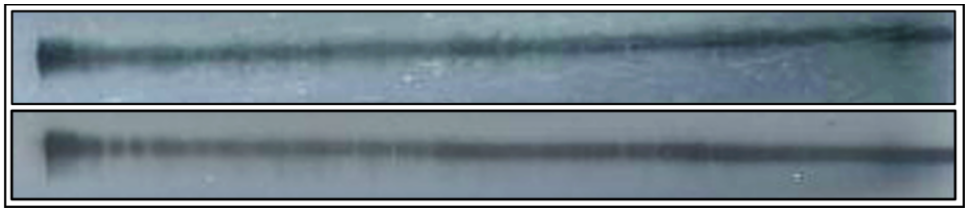

FIGURE 9.4: A comparison of the null spectrum of shot Z3605 and the Argon absorption spectrum from 3606 using a PET crystal.

integrated measurements on x-ray film. This allowed for argon K-shell line absorption spectra to be recorded while simultaneously recording neon K-shell line absorption spectra. In this scenario, even if the Z back lighter was not intense enough in the tail end of the photon-energy distribution there would still be a neon measurement that could be used to interpret the effect of the argon addition.

Figure 9.4 shows the x-ray film from the neon/argon mixture shot (Z3606) and the null shot (z3605). In comparison with the null shot, there are very clear absorption features present. As far as testing the feasibility of the Z dynamic hohlraum radiation drive to support argon K-shell absorption measurements, this result is promising.

9.2 Chordal Fiber Laser Interferometry Results

9.2.1 Diagnostic design evaluation

To better understand the behavior of the PDV diagnostic, RIET (Radiation Induced Effects Timing) noise probes were employed, as well as, a null shot, in which no gas was in the cell, was fielded. The information and experience gained from these two separate efforts was invaluable.

9.2.1.1 Radiation Noise characterization

It was important to characterize the radiation effect in the fiber optic system, because of the close proximity of the gas cell with the z-pinch radiation source, $\sim$5.9 cm. Figure 9.5 compares the beat frequency, $\bar{f}$, measurements of the plasma and that of the RIET

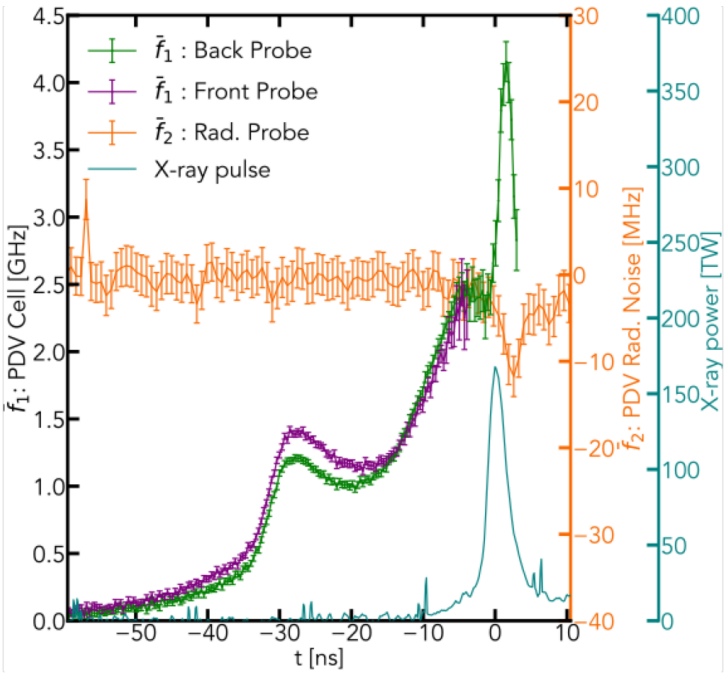

FIGURE 9.5: "Gas cell and RIET noise probe PDV measurements from shot Z3600. The front (purple trace) and back (green trace) PDV probe measurements are on the order of gigahertz. The PDV measurements made with the RIET radiation noise probes (orange trace) are on the order megahertz. The measurements of the plasma are $\sim$ 2 orders of magnitude greater than the noise measurements."-[67]

(Radiation Induced Effects Timing) noise probes, as well as, their relative timing with the x-ray pulse.

The radiation effect on the fiber optics starts to raise above the signal to noise level around $\sim$ 5 ns before the peak of the x-ray pulse. Remember, the expected radiation signature in a PDV from irradiation of the fiber optic cables produces a decreasing beat frequency. For the majority of the initial photoionization of the gas cell the radiation noise is nonexistent.

Figure 9.6 shows a comparison of the individual RIET signals from the four shots taken for the SAT21a series in May of 2021. The reproducible nature between the measurements made with the right and left RIET probes is note-worthy. Specifically, the two shots Z3606 and Z3607, have almost identical response to the x-ray flux between the right and

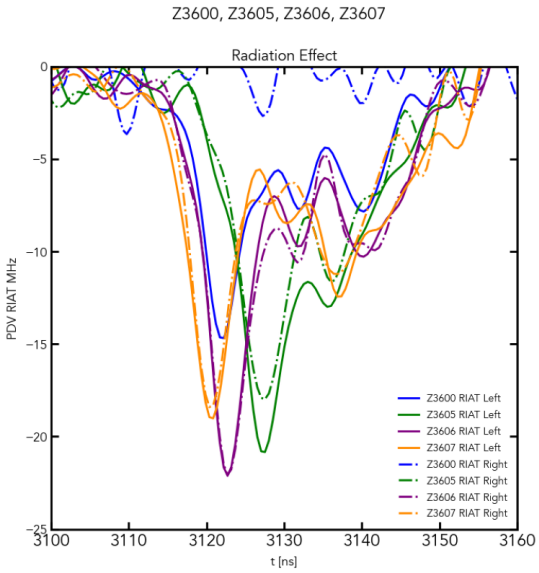

FIGURE 9.6: RIET noise measurements of the left(solid) and right(dashed) side of the gas cell from shots: Z3600(Blue), Z3605(Green), Z3606(Purple), Z3607(Gold). Note: The fiber optic cable of right RIET probe from Z3600 was partially pinched and as consequence the sensitivity was reduced. Thus, making it unable to observe the radiation signature.

left. Shot 3605 while not exactly the same looks to be fairly similar and may just be off by a scaling factor. Unfortunately for shot Z3600, the right RIET fiber was pinched during final assembly and the fiber optic was not sensitive enough to respond to the x-ray signal. Figure 9.7 shows an averaged result of the RIET data, excluding the right Z3600 RIET probe, with the minima aligned at 0 ns. Of these four shots, the peak radiation noise measurement was ∼-22.5 MHz, with the average peak value of about -15 MHz.

Further reproducibility is observed among all of the noise measurements, both in peak measurements and temporal characteristics. Looking at this information as a whole, has several important takeaways. The first being, the radiation effects induced in the fiber optics are —predictable— as the radiation noise measurements are indeed characterizable and quantifiable. Second, the shielding implemented successfully mitigated the potentially hazardous effects of the harsh radiation environment. Third, since these radiation effects are highly similar between the two sides of the gas cell, their ability to characterize the radiation effect in the fiber optics used for the plasma measurements

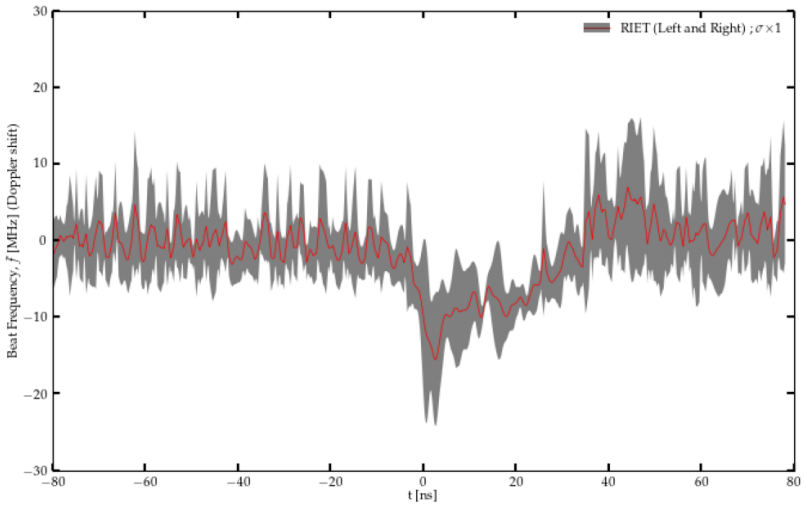

FIGURE 9.7: Average radiation signature from the RIET probe measurements from shots: Z3600, Z3605, Z3606, Z3607.

are likely to be as precise if not more. The highly reproducible nature and characterizability of the noise experienced in the fiber optics provide a strong basis for trusting the measurements made of the plasma with PDV.

The contrast is striking between the radiation noise levels and those of the beat frequency levels observed from the plasma measurements, which are on the order of GHz. Due to this large difference in beat frequency values, GHz vs MHz, the two measurements require different scales. Referring back to Fig. 9.5, the front and back plasma probes are measured along the left axis while the noise measurements are measured along the first right axis, in orange. For Z3600, the plasma beat frequency measurements are $\sim$250–450 times greater than the radiation noise experienced by the fiber optics.

9.2.1.2 Null shot characterization

A null shot was carried out on Z3605, in which there was no gas fill in the cell. This shot was important for assessing PDV characteristics without gas fill. In general, null shots represent very important measurements for any diagnostic. For a null shot of this style, the hypothesis as the following, without gas between the probes to be photoionized

there should be no increasing electron density and thus no decrease in the refractive index along the optical path of the plasma probes. As is typical, the result was less cut and dry. While, indeed, the measured beat frequency, $\bar{f}$, was much less and only started to become significant right around the x-ray peak, it was nonetheless unmistakable evidence of plasma detection. Figure 9.8 shows the beat frequency of the front and back probes.

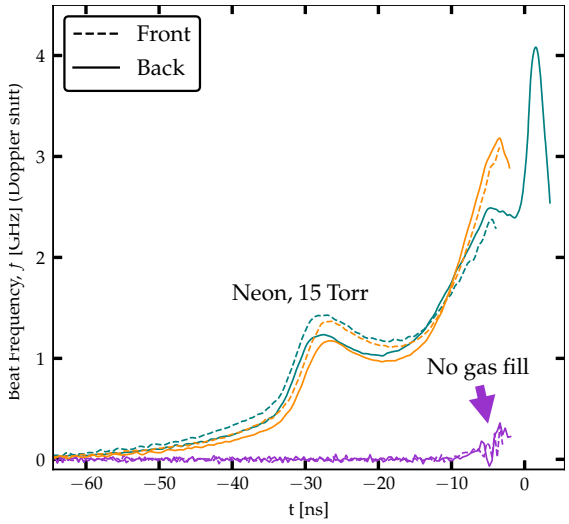

FIGURE 9.8: *"With nothing to measure me measure nothing."* A comparison of beat frequency time histories from two nominally identical 15 Torr neon shots, Z3600 (teal) and Z3607 (gold), in the far position compared to the null shot, Z3605 (purple).

The next question, obvious some might say, what is the electron density? This question is much easier asked than answered. Without having a concrete method to define the electron ablation cloud let alone the temporal evolution, performing a calculation to extract the electron number density time history is pure speculation.

9.2.2 Neon, 15 Torr, far position

Two nominally identical neon shots, Z3600 and Z3607, were fielded with a prescribed fill pressure of 15 Torr. Figure 9.9 shows the PDV shot summaries of Z3600 and Z3607. Both of these shots had very similar results for the PDV measurements from both the plasma and the RIET probes. Peak beat frequencies measured are in the range of 3 to 4 GHz,

while peak radiation noise measured by the RIET probes is on the order of -20 MHz. For both shots, the ratio of radiation noise to plasma signal during the intense x-ray burst is 2% or less. The relative uncertainties for the beat frequency measurements are on the order of a few percent and the electron density time histories have a relative uncertainty of few tenths to a few hundredths of a percent. The shot summaries presented in Fig. 9.9, show a well characterized fiber optic system, both in the precision of the plasma measurements and the high quality understanding of the radiation effect.

9.2.2.1 Preheat observation

A new temporal realm has been observed in the photoionized gas cell experiments, due to the use of PDV. Typically, the data recorded with TREX are centered around ∼2–3 ns around the peak of the x-ray pulse, ∼3–5 ns. If both sides, A and B, of TREX are used for time gated measurements, this temporal realm can be extended by another few nanoseconds. Typically, the desire is to center the gated measurements more closely around the peak of the x-ray pulse for two reasons. First and foremost, is that there is only a small amount of time to collect meaningful x-ray absorption data based on the intensity of the pinch radiation. When, the gated measurements are mistimed too early or too late, the result is either faint or no spectra. The second reason to tighten the temporal spread of the gated measurements is to improve the temporal resolution. Thus, until now, any of the initial photoionization phase of the gas cell has never been observed.

Prior to the ∼5 ns x-ray pulse, an initial period, ∼50 ns, of low photon-energy radiation serves to "pre-heat" the gas cell, as well as the surrounding —*everything*—. The run-in phase of the z-pinch drives the early photoionization in the gas cell from lower energy radiation deposition into the gas cell. Figure 9.10 shows the average charge state as a function of time. From Fig. 9.10, we can see that this initial period of ionization burns through neutral neon through F, O, N, and C-like charge states. While simulation has predicted similar charge state time histories and x-ray absorption spectroscopy has

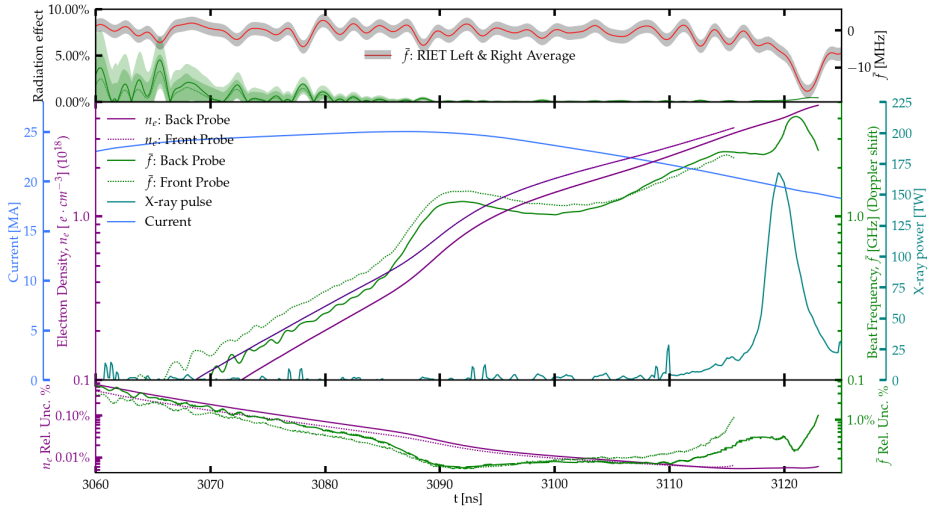

(A) Z3600 PDV processing and analysis summary plot

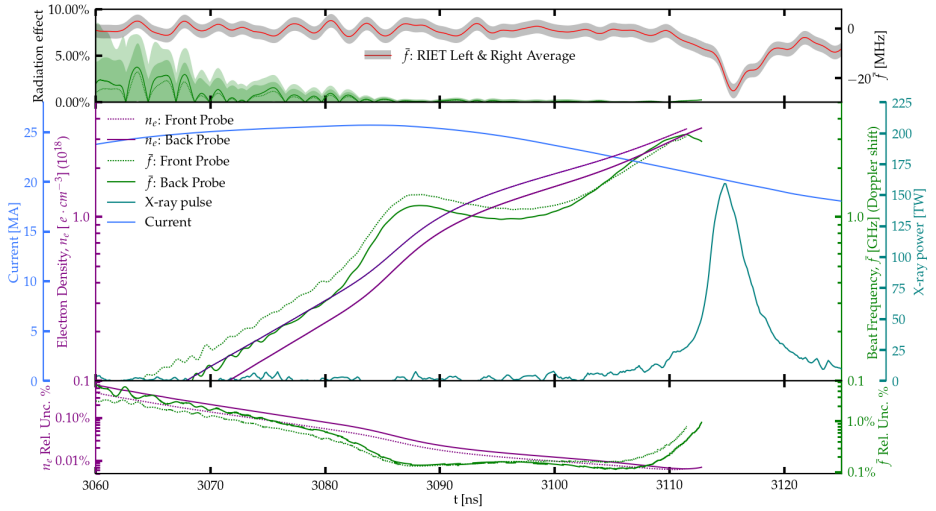

(B) Z3607 PDV processing and analysis summary plot

FIGURE 9.9: Z3600 & Z3607 PDV processing and analysis summary plot. Top panel: The averaged (left and right) RIET signal, red trace. The ratio of radiation noise, the red trace, to the PDV beat frequency measurements, green traces in the middle panel. Middle panel: Z-Machine current pulse (blue trace). X-ray pulse (teal trace). The green traces are the beat frequency measurements recorded with PDV plasma probes. The purple traces are the electron density time histories extracted from the green traces. The front probe measurements are signified by the dashed traces while the back probe measurements are signified with a solid trace. Bottom panel: The relative uncertainties for the beat frequency and the electron density time histories shown in the middle panel.

confirmed the average charge state during the peak of the x-ray pulse, this is the first direct observation of the initial pre-heat photoionization phase.

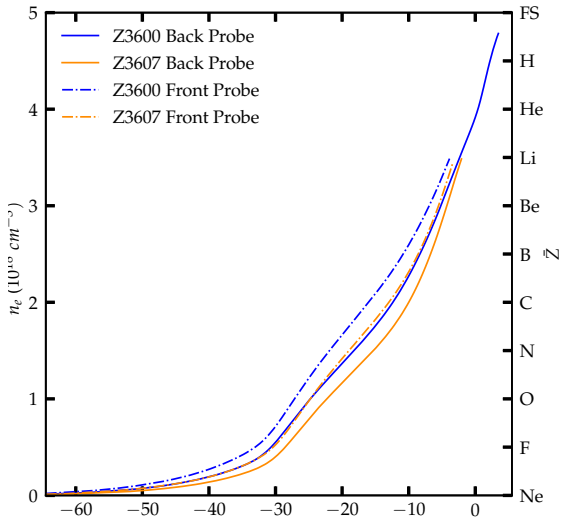

FIGURE 9.10: Average charge state time histories for photoionized neon with 15 Torr in the far position, from shots Z3600 and Z3607.

It's helpful to remember that the beat frequency represents a rate that is proportional to the rate of total ionization of the neon and neon ions. From this view, the interpretation of the first hump is an acceleration of the photoionization. This acceleration is believed to be due to an x-ray pre-pulse ∼20-25 ns before the main x-ray pulse. Investigation of the early behavior of these radiation drives on Z has been conducted. [61] Sanford et al. document observations of a pre-pulse in the x-ray drive of single and double nested cylindrical wire-arrays with and without the central CH foam target. Figure 9.11 are figures detailing the observations made by Sanford et al. as well as simulations of the pre-pulse behavior. What is seen by this work, is the existence of an extra radiation feature ∼23 ns before the main x-ray pulse, with a pulse width ∼5-7 ns in duration. Very similar in character to the pulse found in the PDV measurements with gas fill.

Interestingly, there is one main observation found in Z3600 that sets it apart from all the other PDV plasma measurements, this back probe is the only measurement that extends past the peak of the x-ray pulse. Not only does the signal persist through the peak of the

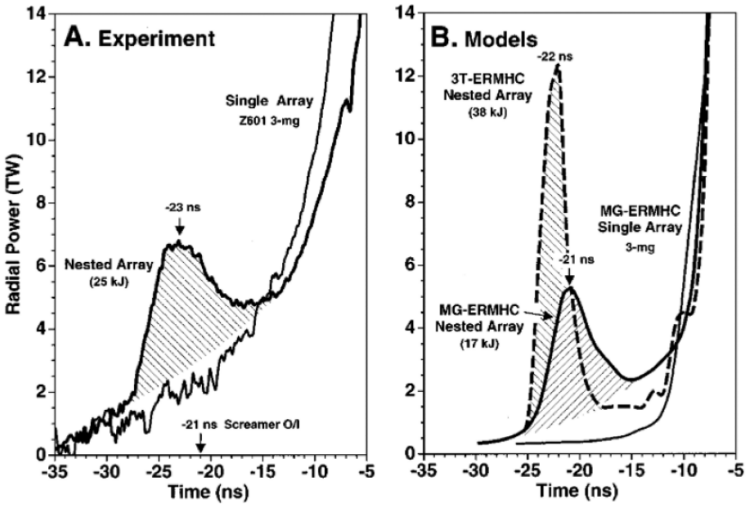

FIGURE 9.11: Sanford et al. has documented previous experimental and simulation effort to characterize the radiation flux from the single and double nested wire-arrays with dynamics hohlraums. Sanford et al. documents an early time radiation pulse, ∼20-25 ns before the x-ray pulse peak. Timing that corresponds well with the "ionization rate" hump seen in the PDV data for shots Z3600, Z3606, Z3607.
Figure reproduced from Sanford et al. [61]

x-ray pulse, there is a feature, a “hump”, at the end. The hump has a similar FWHM to that of the x-ray pulse. Similar in behavior to that of the radiation pre-pulse early in time.

9.2.2.2 Signal loss

A zeroth order guess for signal cutoff would be due to blocked transmission of the PDV laser beam because the plasma reached the critical electron density for the probe laser, $N_c(\lambda$=1550 nm)=4.6$\times 10^{20}$ cm^{-3}. Unfortunately, the electron density measurements are orders of magnitude below the critical electron density, thus, making such a hypothesis unlikely. Signal loss in PDV has been discussed in a variety of other experiments, [14, 58, 13, 28, 67] which have had a variety of mechanisms proposed.

The potential of “Beam steering”, is a possibility, which would occur if there were successfully denser plasma gradients and/or regions that would cause the PDV laser to be misaligned. Another possibility is the momentary passing of plasmatesimals, discrete

volumes of plasma that have a larger electron density within than the surrounding volume of plasma. Inverse bremsstrahlung absorption, has been proposed as a potential culprit for signal loss. [67] The electron areal electron density, aka column density, can attenuate the signal through the plasma, without achieving densities that are near the critical plasma density.

Since the measurement integrates the electron density along the optical path length, the observation becomes an amalgamation of contributing effects along the optical path length. By implementing more PDV probes and some that are orthogonal can help relieve some of these issues that result from measurements that are inherently spatially blind along one direction.

9.2.2.3 Plasma uniformity assessment

While this data came from our initial efforts to begin utilizing PDV, there are a variety of questions we can ask to further interrogate what we have observed so far. Are the front and back probes in the gas cell similar? If so, to what degree are they similar? Do nominally identical shots show similarity? Do nominally similar shots show consistency between the front and back probes? Generally, do the beat frequency and electron density time histories between the front and back channel and between similar shots any indication of uniformity in the central region of the gas cell?

A natural place to start is by comparing the front and back probes for a single cell at a time. Figure 9.12 shows a comparison of the front and back probes as well as the averaged time history and the percent difference. The first clear takeaway is that the front and back plasma probes trend to a similar value over the experiment duration. This can also be seen from the decreasing percent difference between the front and back probe measurements. The second interesting takeaway from this comparison is that for both shots, Z3600 and Z3607, the back channel starts with a slower ionization rate than the front probe and ends with a faster ionization rate, compared to the front probe. Further, the back plasma probe observes the plasma longer than the front probe.

A potential explanation for the change in ionization rates between the front and the back probe could be due to the geometry dilution effect. In the beginning the neon in the front region of the cell experiences a large flux density and becomes more ionized than in the back region. This leaves more neon ion fuel to be burned through in the back region. Thus, when the radiation flux increases leading into the main x-ray event, the ionization rates for the front and back both increase, however, the ionization rate of the back probe increases more due to the extra resources of lower ionized neon-ions available.

Back to the topic of signal loss and why there seems to be a trend with the front probe loosing signal before the back probe. Similar to the explanation of differing ionization rates, geometric dilution may play an effect here as well. The aperture closing effect due to the inner walls ablating will be stronger for the front probe than the back. Combine this with the fact that the gas in the cell will slow down the free propagation of the ablated wall plasma gives a recipe that explains the following: why aperture closing would be delayed for the gas fill cases and why the back probes seem to survive longer with gas fill compared to that of no gas fill.

Keep the same perspective, assessing the similarities and differences of the front and back plasma probe measurements, we can turn our attention to the electron density time histories extracted from the beat frequency measurements. Figure 9.13 shows the comparison of the front and back measurements of the electron density time histories for these two neon shots with 15 Torr of filling pressure. Similarly, as to the case of the beat frequency time histories, the electron density time histories trend closer to the same value over time. If the front probe were to continue on without loosing signal before the back probe, it is hard to imagine the electron density of the back probe increasing to a large value over the front probe.

Another perspective in which we can assess the internal evolution of the photoionization of the neon plasma is by comparing “like” probe with “like” probe between shots. Figure 9.14 depicts just such comparative analysis of the electron density measured

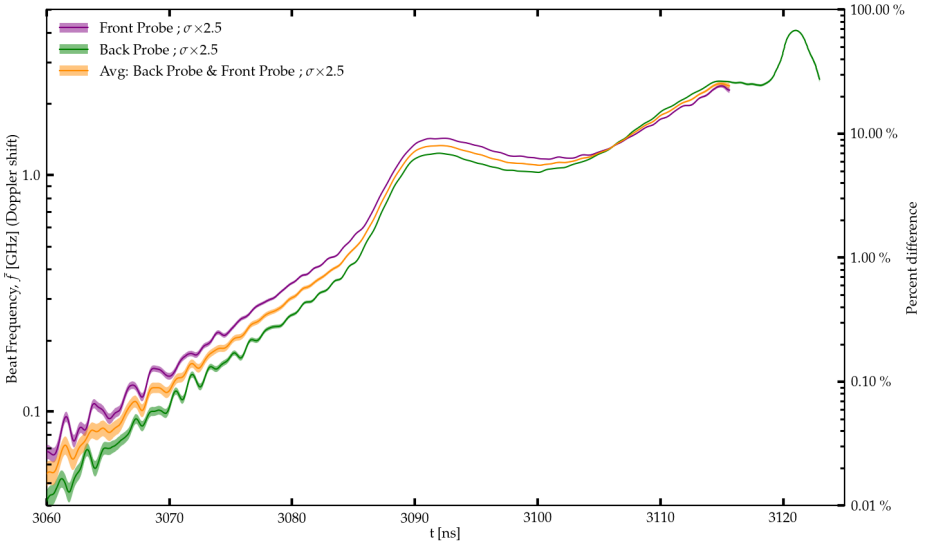

(A) Z3600 comparison of the front and back PDV plasma probe beat frequency time histories.

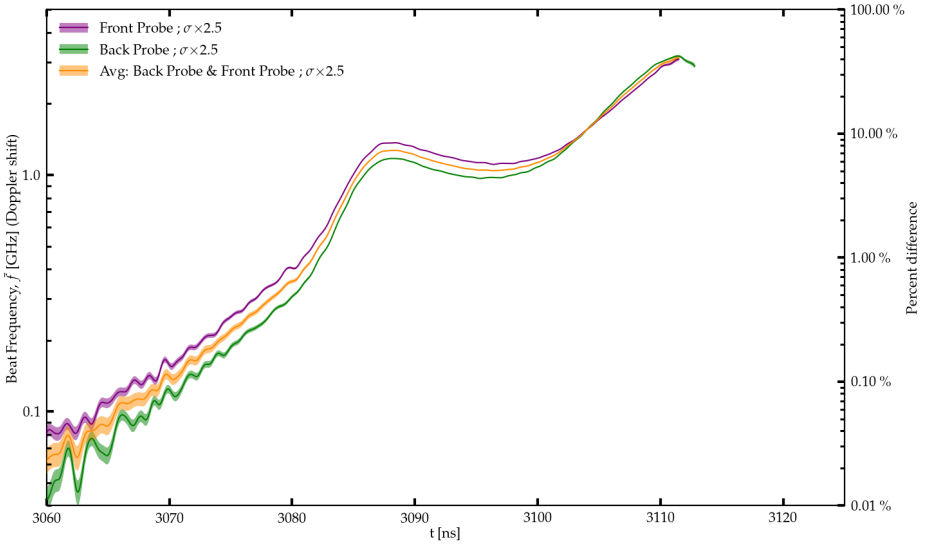

(B) Z3600 comparison of the front and back PDV plasma probe beat frequency time histories.

FIGURE 9.12: Z3600 & Z3607 Front and Back PDV plasma probe comparison of the beat frequency time histories. The front PDV plasma probe(purple) is averaged with the back PDV plasma probe(green), averaged result of the PDV plasma probes(orange trace). The percent difference of the measurements made from the front and back probes is given by the red trace. The shadowing of the various traces represents the uncertainty. σ is an artificial multiplicative constant used to increase the value of the uncertainties so that the uncertainty behavior can be observed.

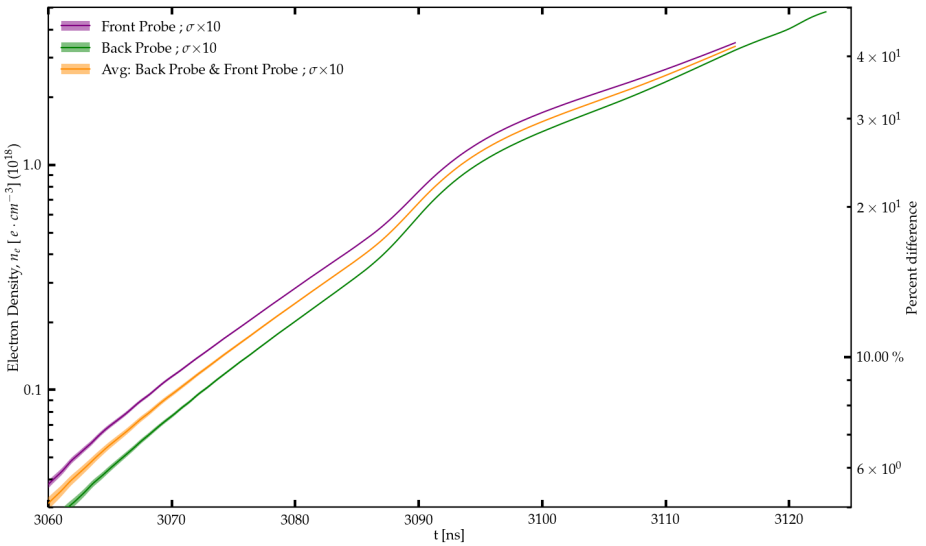

(A) Z3600 comparison of the front and back PDV plasma probe electron density time histories.

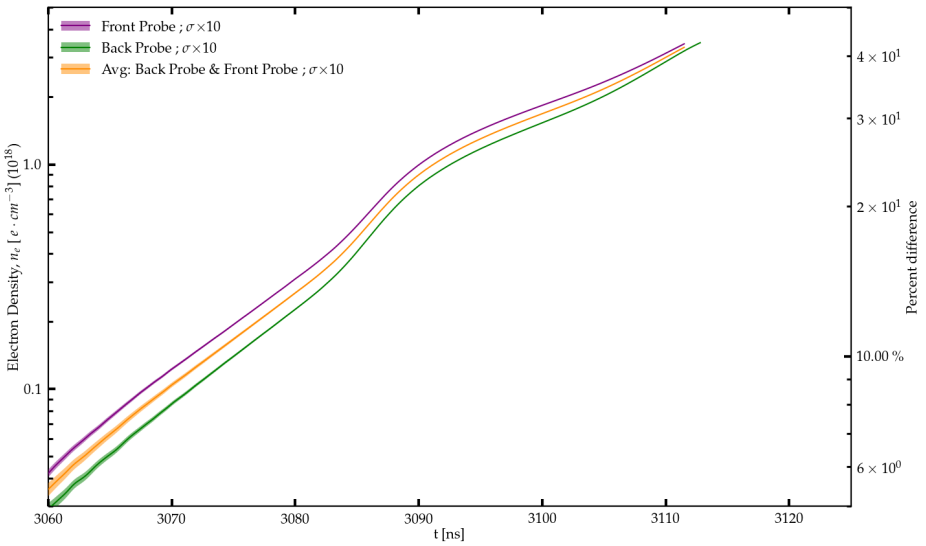

(B) Z3607 comparison of the front and back PDV plasma probe electron density time histories.

FIGURE 9.13: Z3600 & Z3607 Front and Back PDV plasma probe comparison of the electron density time histories. The front PDV plasma probe(purple) is averaged with the back PDV plasma probe(green), averaged result of the PDV plasma probes(orange trace). The percent difference of the measurements made from the front and back probes is given by the red trace. The shadowing of the various traces represents the uncertainty. σ is an artificial multiplicative constant used to increase the value of the uncertainties so that the uncertainty behavior can be observed.

from the front and back PDV plasma probes. Initially inspecting Fig. 9.14a, we find very similar electron density trends as were found in the averaged results of the front and back probes of shots z3600 and Z3607 in Fig. 9.13.

We can continue to slice up the comparative analysis, by comparing the averaged electron density time history for each shot. Figure 9.15 shows the cell probe averaged comparison for the beat frequency (Fig. 9.15a) and electron density time histories (Fig. 9.15b). A familiar scene to that of the front and back probe comparisons unfolds in Fig. 9.15a. However, in this scenario, should this be familiar? To be specific, the behavior that has popped up again is that the electron density evolution that starts with slow ionization rates "seem" to have increased ionization rates later in time. To reiterate, shot Z3607 (pink) has a slower ionization rate to that of Z3600 in the beginning. Once however, the main x-ray pulse begins, a jump in the ionization rate is observed, just like it was for the front and back probe comparison. While both ionization rates increase, it is the ionization rate with lower rate initially that ends up with the larger ionization rate in the end.

Indeed, there are differences between the front and back probes of a single shot as well as between nominally identical shots, however these differences are more of a testament to the sensitivity of PDV than to hydrodynamic perturbations. In fact, what we find, from this initial effort, is that the central region of the gas cell appears to evolve in quasi-uniform manner with trends that suggest the uniformity increases over time.

From what has been presented thus far, PDV appears to be a well suited diagnostic for the photoionized gas cell platform. Noise in the fiber optics has been mitigated. The null shot has shown largely that without gas in the cell there is essentially no response in the PDV system. Further, the comparison between two nominally similar cases has revealed reproducible trends in plasma evolution behavior between “like” probes and cell averages. These outlined successes have nailed all of the original goals for the introduction of the PDV system.

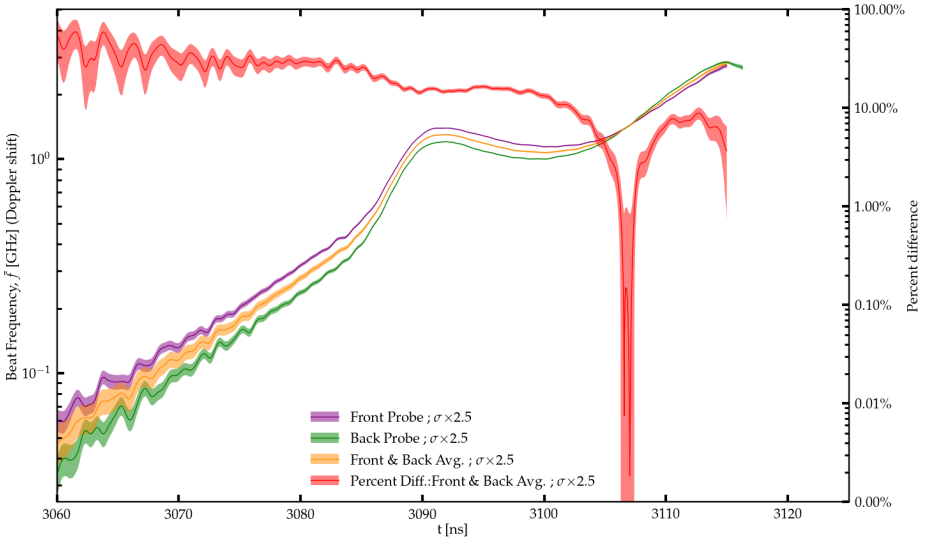

(A) Beat frequency averages from the Front and Back PDV plasma probes from shots Z3600 and Z3607.

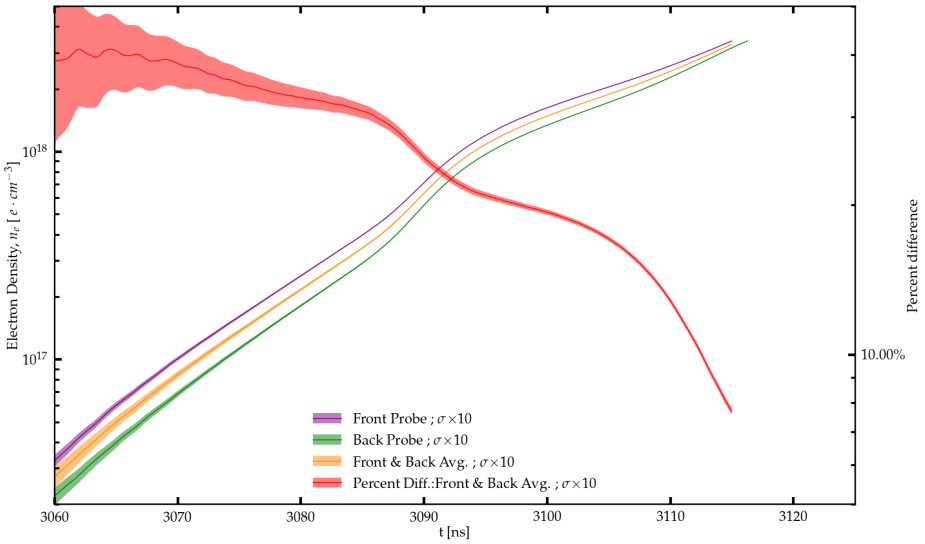

(B) Electron density averages from the Front and Back PDV plasma probes from shots Z3600 and Z3607.

FIGURE 9.14: Averaged PDV plasma probe results of front and back from shots Z3600 and Z3607.

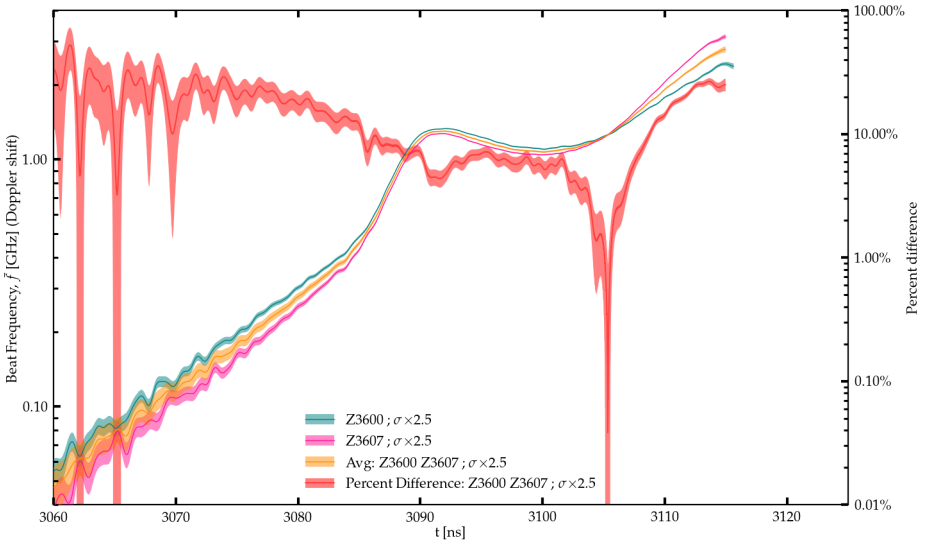

(A) Average beat frequency time history averaged from nominally similar shots Z3600 and Z3607.

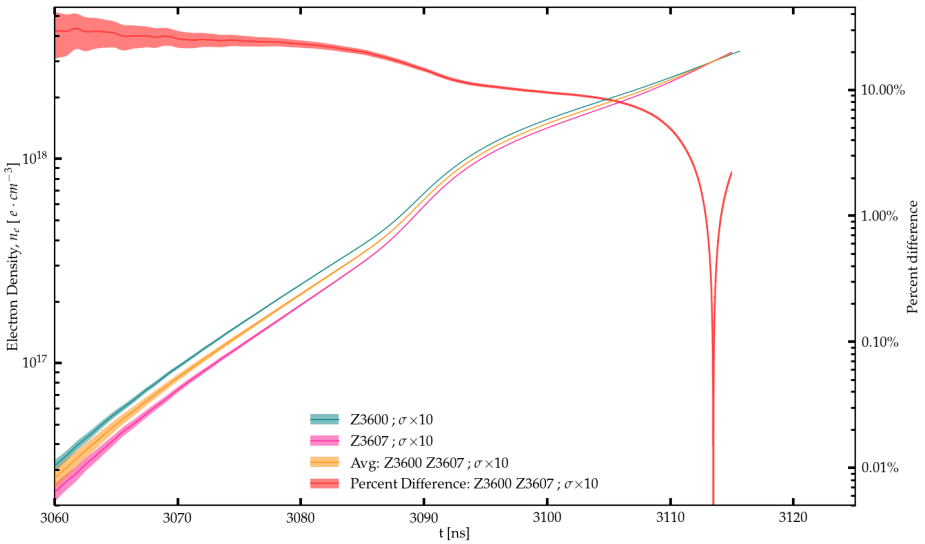

(B) Average electron density time history averaged from nominally similar shots Z3600 and Z3607.

FIGURE 9.15: Averaged result of the cell averages of shots Z3600 and Z3607.

9.2.2.4 Helios-CR simulations

One dimensional radiation hydrodynamic simulations were conducted with Helios-CR[42] for a gas cell with 15 Torr of neon fill pressure in the far position on the anode plate of the Z-machine. As a reminder the position on the anode plate is the method used to adjust the x-ray flux that irradiates the gas cell, thus modifying the ionization parameter by reducing the numerator. The x-ray flux at the front window of the cell in the far position is about 6.5×10^{11} W/cm^2, about half of what the front window the gas cell experiences in the close position.

Two simulations were conducted for this experimental set-up using two different estimates for the x-ray flux that drives the simulation. The first simulation uses the expected x-ray flux that irradiates the front window of the gas cell. While, the second simulation uses an estimate for x-ray flux irradiating the rear window to drive the simulation. The estimate for the rear window x-ray flux is a geometrically diluted form of the x-ray flux irradiating the front window. The idea being that these two forms of the x-ray flux represent upper and lower bounds for the x-ray flux that drives the photoionization in the gas cell for the simulations.

Figure 9.16 shows the electron density time histories that have been averaged over the hydrodynamically unperturbed region of the interior of the gas cell. As well, the plot show the averaged result of these two simulations along with the percent difference. As expected there is an observable difference between the front and rear simulations, with the rear simulation lagging in electron density by a $\sim$2-5 ns. Ultimately this difference between the simulations is minor, with both simulated electron density time histories exhibiting similar characteristics.

Figure 9.17 shows the beat frequency time histories calculated from the two simulations as well the averaged beat frequency and percent difference between them. Similarly to Fig. 9.16, both simulations demonstrate consistent behavior with the rear simulation lagging behind the front. An important nuance though, is found towards the end

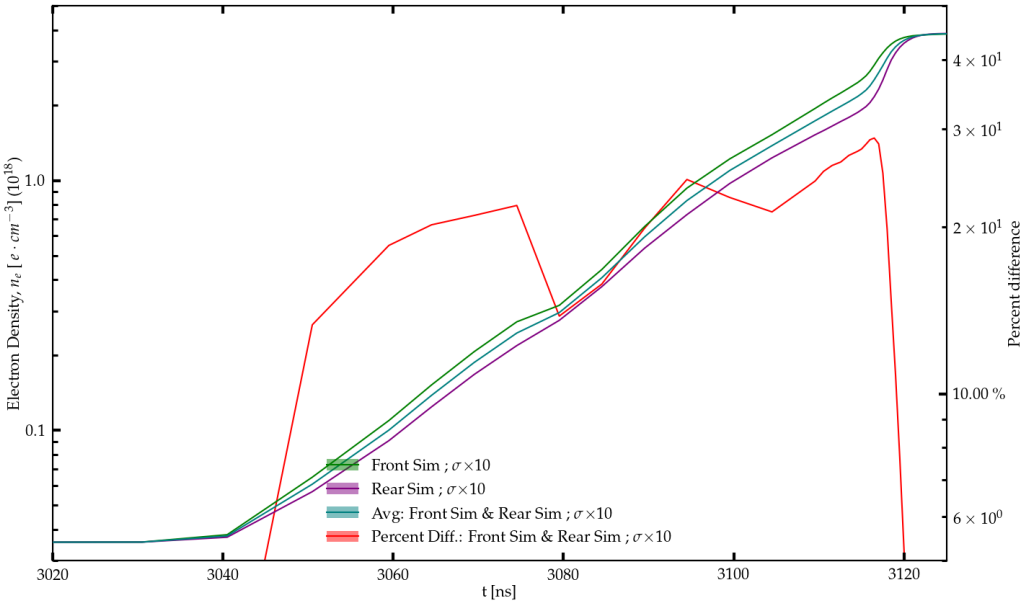

FIGURE 9.16: Comparison of two simulated electron number density time histories, for the case of a neon gas cell with 15 Torr of fill pressure in the far position. The green trace is the simulation driven with x-ray flux that is expected to impinge on the front window of the gas cell. The purple trace is the expected flux that impinges on the back window. The blue trace is the average of the two simulations and the red trace is the percent difference between the two simulations.

of the simulation near the peak of the x-ray pulse, ~10-15 ns before 3120 ns. The rear simulation beat frequency is slightly diverging from the front simulation and subsequently increases superseding the front simulation. An interesting characteristic that is similar to what has been seen in the data.

9.2.2.5 Comparison with simulation

A goal that was intended for the future was the comparison of electron density time histories with simulated electron density time histories. Due to the crisp quality data recorded, such efforts to compare with simulation are realizable.

Figure 9.18 shows a plot comparing the experimental and simulated beat frequencies for a gas cell with neon fill, with 15 Torr filling pressure in the far position on the anode plate. Upon inspection, the early time behavior of the simulation and experiment are

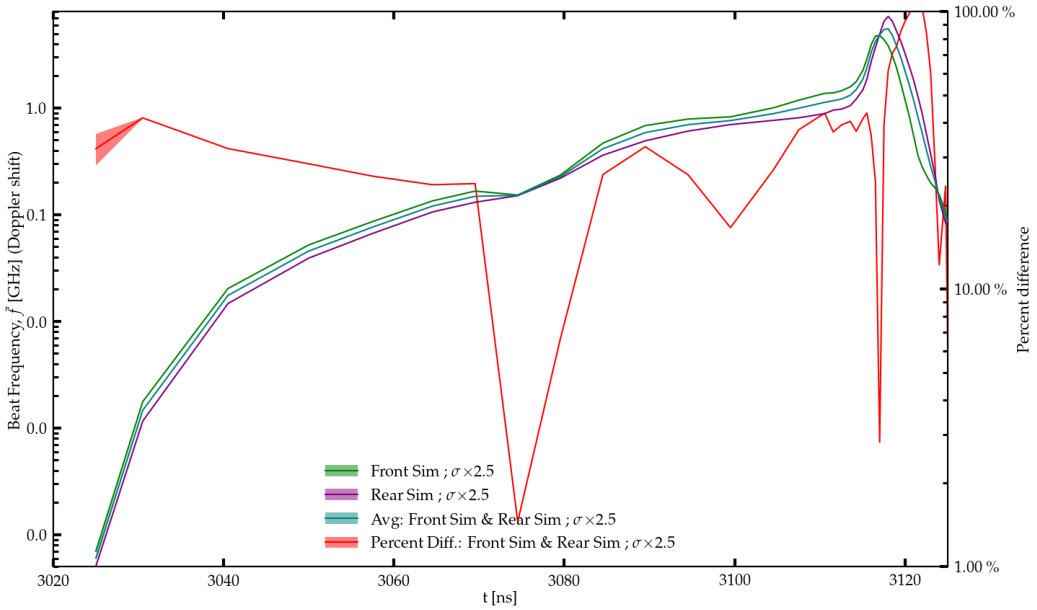

FIGURE 9.17: Comparison of two simulated beat frequency time histories, for the case of a neon gas cell with 15 Torr of fill pressure in the far position. The green trace is the simulation driven with x-ray flux that is expected to impinge on the front window of the gas cell. The purple trace is the expected flux that impinges on the back window. The blue trace is the average of the two simulations and the red trace is the percent difference between the two simulations.

very different. The electron density time histories kicks on about 20 ns before that of the experiment. However, the differences in behavior are diminished in the 20-30 ns before the main x-ray pulse starts. In this region, the simulations match fairly well with the rate of ionization observed in the experiment. It is in the $\sim$5 ns right before the peak of the x-ray pulse that the we see differences in behavior show up again. The simulations differ from experiment in that both show a greater rate of ionization right before the pulse, which is not observed in the experiment. As well, the back probe of Z3600 as was discussed earlier extends further with a larger electron density than the simulation.

Turning our focus now to Fig. 9.19 we find overall similar behavior as is expected based on the electron density comparison. However, there are several obvious discrepancies, the experimental data is much more dynamic than that of the simulation. The experiment shows a fluctuation in the ionization rate that is absent from the simulation. The

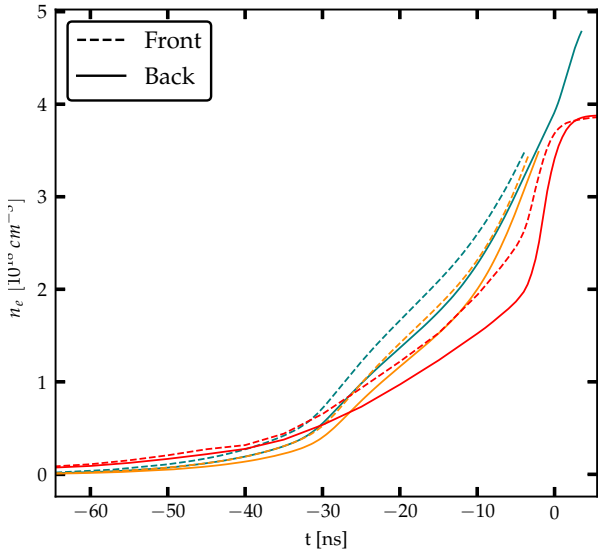

FIGURE 9.18: A comparison of electron number density time histories for the two 15 Torr neon gas cell shots in the far position with corresponding simulated electron number density time histories shown in Fig. 9.16

ionization rate over all is typically faster than the simulation. As well, The experiment has several moments in which the ionization rate starts to decrease, shortly after the first bump around 3090 ns and right before the bump around the peak of the x-ray pulse. Going further in discrepancies between the two, the front and back probes trend towards similar values over time while the simulation shows divergence between the front and rear.

A point of commonality though found between the experiments and the simulations in this effect of the slower ionization rate overtaking the faster ionization rate, demonstrated in Fig. 9.17. This interesting behavior has two different ways in which it can be compared to experiment.

The first and most direct comparison is made by comparing the behavior between Fig. 9.15a with Fig. 9.17. In the experiments, Z3607 has a slightly weaker x-ray flux than that of Z3600. Yet, in the comparison of these shots it is the average result of Z3607 that has an ionization rate that supersedes Z3600. Similarly, in the simulations, it is the simulation driven with a reduced flux that has an ionization rate that ends up

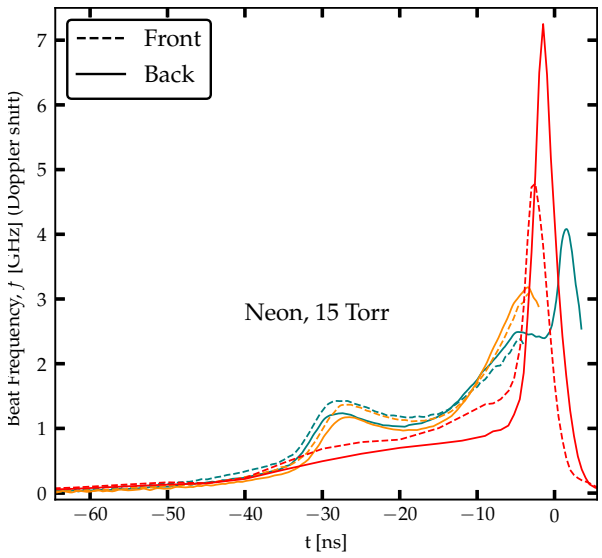

FIGURE 9.19: A comparison of beat frequency time histories for the two 15 Torr neon gas cell shots in the far position with corresponding simulated beat frequency time histories shown in Fig. 9.17

superseding the ionization rate of the simulation with a larger x-ray flux.

Alternatively, we can make a similar comparison with the behavior of the front and back probes of Figs. 9.12 and 9.14a. This comparison however is not as direct as the previous one. Yet, this behavior is similar nonetheless. The x-ray flux density is large in the front portion of the gas cell than it is in the back due to geometry dilution. This difference in x-ray flux whether between different shots or due to geometry dilution creates a situation in which the gas that is more heavily ionized in the beginning of the shot ultimately runs out of atoms and ions to ionize further, leaving the less heavily ionized gas to be more readily ionized and thus the ionization rate increases towards the end.

In an attempt to understand this difference better, the fractional ion population evolution was overlaid on the plots comparing the beat frequencies from experiment and simulation. The main hump at the end of the simulated beat frequency history looks to be due to the rapid ionization through C-, B-, Be-, Li-, and He-like neon ions. Leading up to this hump at the end is the evolution through neutral neon and F-, O-, and N-like

neon ions. This evolution starts gradual and increases up until the point of the hump. Focusing back on the beat frequency history from the experiments, there is an initial hump not seen in the simulation. Since the main hump at the end of the simulation is due to a rapid ionization of the plasma, maybe the initial hump in the experimental data is as well due to a period of rapid ionization.

To investigate this discrepancy further between the model and the experiment, the average charge state time histories from the experiment and the simulation were compared. This was done by comparing the point in time each whole integer average charge, i.e. each new neon ion, was reached. This was done for both Z3600 and Z3607 and what was found was the one-dimensional Helios-CR simulation achieves the first two ionization stages before the experimental data does. After the first two charge states the behavior inverts, that is, the simulation predicts the timing of reaching the next charge states to be after they have been reached in the experiment data. This behavior is shown in Fig. 9.20, where positive delay values indicated the simulation predicted the charge state was reached ahead of the experiment and negative values indicate the simulation prediction of reaching the charge state is delayed.

There are several important observations that come from this comparison of the experimental data with simulations. The discrepancies of the early time behavior point towards inaccuracies of the radiation drive used to drive the simulations. This is made very clear with the missing ionization hump seen in the experimental data that is most likely due to the x-ray pre-pulse that has been previously documented. [61].

Even though there are discrepancies early in time, the simulation produces similar results that compare well with experiment. The first of which is the ionization rate in the $\sim$20 ns prior to the peak of the x-ray pulse. The rates in the simulation compare well with the experiment. This is a likely indication that the central region of the gas cell is unaffected by the propagating shocks up to the point of signal loss. Since, these simulations are taken from the quasi–hydro-unperturbed region between the shocks.

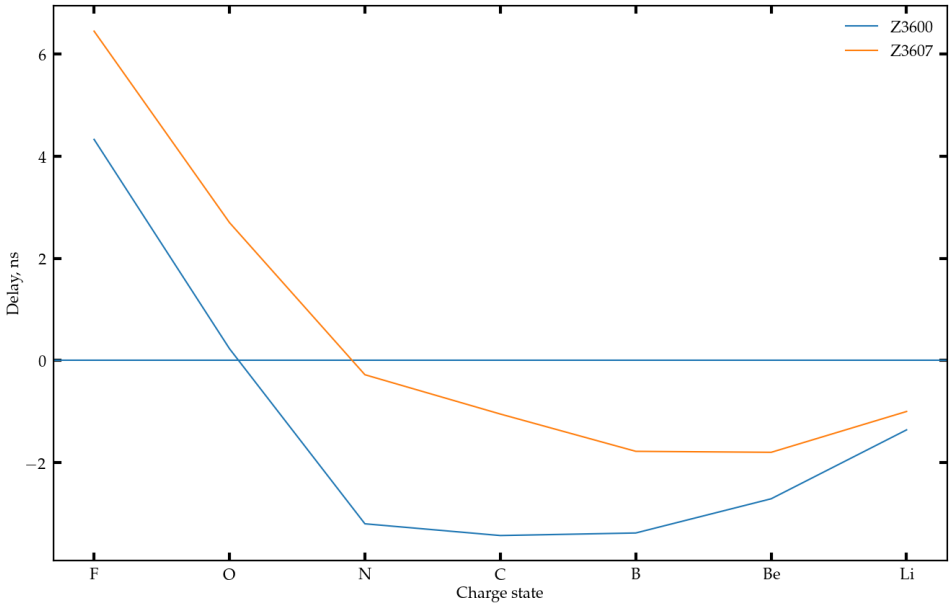

FIGURE 9.20: Timing discrepancies of evolutionary behavior the photoionized plasma in the gas cell between experiment and simulation. Positive delay values indicate the simulation reaches the charge state before the experiment. Negative delay values correspond to the simulation reaching charge states after the experiment.

Another interesting comparison between the experiment and the simulation is the ionization behavior due to differing levels of flux. This is seen in two different ways, either cells that are driven with two different levels of flux or the difference in flux between the front and the back. The simulations reproduce similar behavior, another indication that simulations are capturing the nuances of the atomic kinetics occurring in the photoionized plasma experiment.

9.2.3 Neon & Argon 50:50 Mixture 60 Torr far position

One exploratory shot, Z3606, was taken in which a 50:50 gas mixture of neon and argon was used and fielded with 60 Torr of gas fill. 60 Torr was chosen as this equates to 30 Torr of neon and 30 Torr of argon. While the purpose of this shot was not specific to PDV in any way, it allowed for more experience utilizing PDV expecting greater electron densities. Figure 9.21 shows the PDV data summary for the neon/argon mix

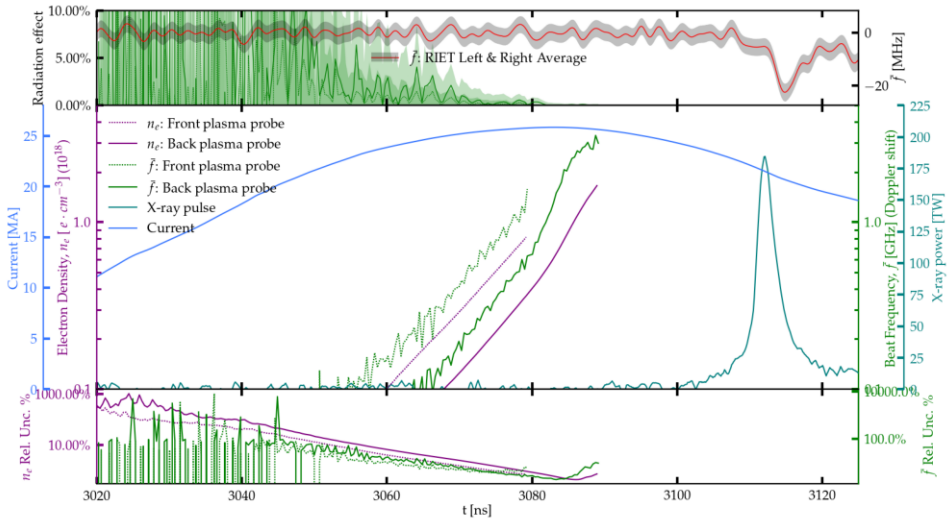

FIGURE 9.21: Z3606 PDV processing and analysis summary plot. Top panel: The averaged (left and right) RIET signal(red trace). The ratio of radiation noise, the red trace, to the PDV beat frequency measurements, green traces in the middle panel. Middle panel: Z-Machine current pulse (blue trace). X-ray pulse (teal trace). The green traces are the beat frequency measurements recorded with PDV plasma probes. The purple traces are the electron density time histories extracted from the green traces. The front probe measurements are signified by the dashed traces while the back probe measurements are signified with a solid trace. Bottom panel: The relative uncertainties for the beat frequency and the electron density time histories shown in the middle panel.

shot. While the beat frequencies and electron density traces do not reach the peak levels as achieved in the neon only shots, the PDV plasma probes pick up the increase in electron density much earlier than in the lower pressure neon only shots. While there are these differences in peak electron density and the start of photoionization measurement, there are several similarities shared with the neon only cases. The first being, the back PDV plasma probe has a signal that lasts longer than the front PDV plasma probe. Second, the back PDV probe beat frequency time history shows a familiar acceleration of ionization around 3080 ns. While this back probe trace does get cutoff, this characteristic hump is akin to the beat frequency behavior observed in the neon only shots.

9.3 Summary

The results of this chapter have documented two important advancements of the photoionized gas cell platform on the Z-machine, as well as for the Z-facility itself.

The first being, the successful integration of the chordal laser Interferometry diagnostic known as photon Doppler velocimetry (PDV). This upgrade of the platform provided the first measurements of electron density time histories from within the gas cell. Measurements that allowed the intricacies and nuances of the pre-ionization stage to be observed for the first time. As well as, providing a means to assess the uniformity of the photoionized neon plasma. An important achievement as the interior region has been predicted to be quasi-hydrounperturbed by simulation. An important factor, as the analysis and understanding of the platform to date is predicated on this fact. Depending on what we learn from this diagnostic going forward may change the interpretation of spectroscopic observations.

Further, these achievements are not only valuable for the platform, they extend beyond more generally to the Z-facility. The fielding of PDV with gas cell represents the first time that PDV has been operated in close proximity to the intense x-ray flux of the Z-machine. The results shown here demonstrate how to mitigate adverse radiation effects for high quality measurements. In tandem, these results as well provide a method for future experiments to characterize the radiation effect that is experienced within the fiber optic system. Allowing for quantitative measurements that characterize the radiation effect.

The second advancement for the gas cell platform, and by extension for Z, was the argon K-shell line absorption measurements. The feasibility test has shown that the tail end of the spectral distribution of the radiation drive, produced by the z-pinch dynamic hohlraum, is capable of supporting argon K-shell line absorption measurements. This provides another option for gas mixtures that can be fielded within the gas cell.

Chapter 10

Conclusion

Utilizing Zebra and the Z-machine, three adventures in scientific exploration took place with the goal of advancing our understanding of photoionized plasmas and the radiation sources that drive them, found in highly energetic astrophysical phenomena throughout the universe. This detailed account of experimental adventures exemplify the important aspects of laboratory astrophysics and the crucial role laboratory experiments and data provide in the greater scheme of scientific advancement.

A unique feature of the laboratory journeys presented has been the interplay of the two laboratory platforms for studying photoionized plasma here on Earth. Some of the first photoionized plasma experiments happened on the Z-machine, as there are few places that can provide radiation sources that are astrophysically relevant. The photoionized gas cell platform has provided a much-needed source of high quality laboratory data. Due to experimental constraints with the gas cell platform, such as diagnostic flexibility and experiment time, the need for alternative platforms on university-scale machines, $\sim$1MA, was clear. As a way to alleviate some of the experimental burden on the photoionized gas cell experiments, the photoionized supersonic gas jet platform was conceived for the Zebra pulsed-power driver.

10.1 Zebra

The adventures with Zebra were three-fold: Development of the photoionized supersonic gas jet platform(Sec. 5), obtaining meaningful and complementary results to that of established platforms (Sec. 8), and spectral characterization of Zebra's radiation drive (Sec. 4).

10.1.1 Supersonic photoionized gas jets

The supersonic photoionized gas jet platform was designed to unlock the capability of university-scale pulsed-power machines, like the 1MA pulsed-power driver Zebra, to achieve astrophysically relevant photoionized plasmas. The radiation drive requirements are reduced significantly by using supersonic gas jets as the ionization medium for two reasons. The first being, there is no intermediate medium between the gas jet and the radiation source. Other experiments such as the photoionized gas cell platform require Mylar windows to contain the gas within the cell up until shot time. Experiments that follow the expanding foil archetype require plastic tamping to promote even expansion. For the supersonic gas jet platform, the gas jet is able to leverage the full radiation flux produced from the Z-pinch. The second advantage afforded by utilizing gas jets as an ionization target medium is that the gas jet can be produced much closer to the x-ray source, compared to the gas cell platform the gas jet is an order of magnitude closer to the z-pinch. These two benefits afforded by the utilization of gas jets allow for a more thorough and efficient use of the available radiation flux. Providing comparable complementary photoionized plasma conditions between the 27MA and the 1MA drivers.

The gas species studied were neon, nitrogen, and argon, with the primary elemental species studied being neon, as well, neon/hydrogen gas mixtures were studied. The backing pressure range for the gas jets was in the range of 100-1000 psi. This range in pressures equates to a range of atomic densities of the gas jets to be 10^{18}–10^{19} cm^{-3}.

Nozzle design and characterization was an important aspect, necessary for building our understanding of the gas jet behavior. Two different nozzle designs(Sec.5.4) were used over the series of experiments from 2018-2021. Gas jet characterization was performed via Mach-Zehnder interferometry. An adjacent laser lab, room 102, was used to perform iterative parameter surveys of the gas jet performance. Unfortunately, each nozzle used in the experiments with Zebra are too close to the z-pinch and are obliterated. Thus, Mach-Zehnder interferometry was used to characterize each gas jet in the Zebra chamber before the Zebra shot.

The experimental execution and articulation of the photoionized gas jet experiments benefited from a powerful synergy that arose from the combination of the supersonic gas jet platform and the operational robustness and diagnostic flexibility of Zebra. Since the gas jet does not require any form of containment for positioning, this allows multiple diagnostics perspectives of the gas jet. When coupled with a diagnostic heavy and flexible experimental apparatus like Zebra, a plethora of high quality and enlightening views are made possible which can be used to interrogate the photoionization of the gas jet. To this end, of the many diagnostics employed, the primary diagnostics were X-ray absorption spectroscopy using a KAP crystal spectrometer, dual-color air-wedge shearing interferometry at operating wavelengths of 532 and 266 nm.

The laser interferometry employed provided a means for two-dimensional spatially resolved atomic and electron density maps of the neutral and photoionized gas jets, respectively.

The KAP crystal spectrometer recorded neon k-shell x-ray absorption spectra of the photoionized gas jets. Initial analysis of this spectroscopy show the photoionized neon gas jets to be primarily dominated by B-, Be-, and Li-like neon ions. On occasion C- and He-like neon ion absorption features have been observed.

Agreement between two diagnostics, laser interferometry and spectroscopy, which

operate on completely separate principles show correspondence between their measurements. Areal electron densities calculated from the interferometry analysis is in the range 0–5$\times 10^{18}$ cm^{-}2. The areal electron density calculated from the analysis of the x-ray absorption spectroscopy range from 1-3.5$\times 10^{18}$ cm^{-2}. As well, we find correspondence between the x-ray absorption features recorded on the film and the FWHM of the areal electron density profiles.

In what may be a first, spatially resolved average charge state measurements were performed from laser interferometric techniques. Further, the average charge measurements made from interferometry and x-ray absorption spectroscopy were made and compared. The spectroscopy analysis revealed an average charge state $\bar{Z}$ $\sim$5.8, with the bulk of the fractional ion population centered around B- and Be-like neon. The average ionization state able to be measured with interferometry 6.7$\pm$0.9. Since, the laser diagnostics are 150 ps snapshots in time and are timed to be as close to the x-ray peak as possible, it is expected that these measurements observe larger values than the integrated measurements made with the KAP spectrometer.

The work shown here is the culmination of many experimental campaigns; much of this effort, however, has been to evolve the platform to a steady and robust working state. A mature experimental platform is a necessity so that high-precision measurements can be made routinely without hidden experimental issues.

Future goals for the supersonic gas jet platform are numerous. Improving the ability to use the Mach-Zehnder interferometer for atomic density characterization in the Zebra chamber would be highly beneficial. Such an improvement would allow for average charge state maps to be produced regularly for each shot. This improvement can be achieved in two ways. The first is to improve the beam quality of the diagnostics laser. The second would be to mitigate the ablation that happens near the top of the nozzle which ends up obscuring the best regions to compare between the atomic and electron density maps. Another goal would be to increase the platform's ability to work with

lower density gas jets. A more desirable, astrophysically relevant, atomic density range would be of the order 10^{16}–10^{17} cm^{-3}.

10.1.2 Spectral characterization of Zebra's radiation drive

The radiation drive is of the utmost importance for the photoionized plasmas observed in space and in the laboratory. For this reason, understanding the radiation drive that Zebra is capable of is crucial and represents a large missing piece of the puzzle for the photoionization studies conducted with the supersonic gas jet platform on Zebra.

The missing piece being, modeling and simulation effort to compare with experiment. Without a well characterized radiation drive, like that of Z and/or the celestial radiation drives we aim to emulate, modeling of the experiment is speculative at best. For this reason, the spectral characterization of Zebra's radiation drive has begun, with two separate campaigns completed.

The characterization of the spectral distribution was performed with a grazing incidence diffraction grating spectrograph. This spectrograph was retrofitted from an Acton arc gms 1.5 m McPherson monochromator. When fitted with a 600 line per millimeter grating, the spectrograph has spectral range of $\sim$40-700 Å.

The initial results from these campaigns are of unprecedented quality and detail, unexpected for initial operation of an in house retrofitted spectrograph, thanks to the expert craft of Dr. Bach, Dr. Ivanov, and Alexey Astanovitskiy. After an exhaustive literature review, it appears that it may be the first time that Al L-shell spectra has been observed in this wide wavelength range.

The spectral characterization work is still very much in the early stages of development. Of the many tasks and items to continue working on, the most important is developing a precise wavelength axis and perfecting the characterization of the various components of the spectrograph, i.e. the grating response, MCP/phosphor response, and CCD response.

The wavelength axis calibration has multiple avenues that are being pursued. The first and primary method that should be realized is to use a continuous radiation source with known lines to hone the alignment and define the spectral wavelength range. A secondary option, is to develop the wavelength axis from the line identification of the plethora of emission features found in the aluminum spectra. With correctly identified emission features over the 40–700 Årange, the aluminum spectra can act as a fingerprint for other spectrums that are largely due to thermal emission rather than atomic emission. The secondary avenue is to use the geometry of the spectrograph combined with the use of genetic algorithms to search the parameter space for aligning experimental spectra features between different shots covering the same or portions of the same spectral range.

10.2 Z-Machine

Not only was the experience on the Z-machine an adventure, getting to and fro was in it self an adventure.

10.2.1 Chordal interferometry

Integrating a new diagnostic into the photoionized gas cell platform was quite the experience and sorely needed. The gas cell has historically utilized only two diagnostics, up until the proverbial "torch" was handed off to myself. The pressure transducer allowed for atomic density measurements up till the time Z shot. The TREX spectrometer provided x-ray absorption spectroscopy measurements that can reveal the charge state, fractional population, electron temperature, and areal electron and ion densities. TREX is capable of both time integrated and time gated x-ray absorption measurements.

Yet, neither of these diagnostics were capable of measuring conditions directly in the cell during the shot. Such measurements are of importance as they could be compared with measurements made with the other diagnostics being used and, as well, they could

be used to test and validate simulations. Chordal laser interferometry, PDV, provided just such a method to perform direct measurements of the state of the plasma in the central region of the cell.

A variety of firsts were accomplished with this implementation of PDV with the gas cell. This work represents the first time that PDV has been used in close proximity of the Z-pinch on the Z-machine. The successful operation of PDV allowed the first ever electron density time histories measured from within the gas cell. The measurements naturally revealed observation of the pre-ionization phase of the gas cell.

This success has motivated the use of PDV with the gas cell platform in upcoming experiments. Future implementations will include more PDV probes to provide better spatial resolution as well as to interrogate regions that are expected to be affected by the inward propagating shocks. Further, horizontal vertical PDV probes maybe included in the future as another perspective to measure horizontal density gradients within the cell.

10.2.2 X-ray absorption spectroscopy

The x-ray absorption spectroscopy conducted helped to progress two separate objectives for the gas cell the platform. The main objective was to further fill out the generation III dataset. The datasets are parameterized by fill pressures and x-ray flux irradiating the cell. Thus, there are a variety of parameter combinations that can be used to modify ionization parameter. By modifying these parameters, changes in radiation flux and/or density, the relative importance of electron- and photon-driven atomic processes changes. These changes directly affect the atomic kinetics and the heating of the plasma.

The second main goal for the x-ray absorption spectroscopy measurements was to test the feasibility of recording photoionized K-shell line absorption argon x-ray absorption measurements. This feasibility test is important as astrophysical environments are inherently multi-element systems, which present a much more complicated system to

interpret than single element plasmas. Thus, progressing the platform to the point of studying multi-element plasmas is important.

Initial results from the processing the x-ray absorption measurements show nominal behavior to the exceptional work done previously by Dan Mayes. Future work will entail processing the full set of the generation III spectra. As well as, the Gen-III x-ray transmission spectra will be analyzed providing areal ion densities, charge state distributions, level populations, and temperature of the plasma, of which will be compared with coincident observations made with PDV.

10.3 Summary

The adventures documented in these chapters have explored two experimental platforms that provide a method to produce astrophysically relevant photoionized plasmas in the laboratory. The supersonic gas jet platform on Zebra and the gas cell platform on Z allow for photoionized plasmas with a wide range of parameters to be explored. By the very nature of these two machines, the data produced are complementary; yet both platforms provide unique perspectives in accessible by the other. The photoionization studies performed on Zebra cover lower ionization stages, while the photoionization on Z allow investigation of more highly charged photoionized plasmas.

Appendix A

Presentations and Publications

A.1 Publications

- K. J. Swanson et al. Development and integration of photonic Doppler velocimetry as a diagnostic for radiation driven experiments on the Z-machine. In: Review of Scientific Instruments 93.4 (Apr. 2022), p. 043502. DOI: 10.1063/5.0084638.
- (Prepared for submission)K.J. Swanson, V.V. Ivanov, R.C. Mancini, D.C. Mayes, A.L. Astanovitskiy, O. Dmitriev, E. Diaz-Gallardo, N.L. Wong, and N.A. Huerta, Study of Photoionized Plasmas with a University Scale 1MA Pulsed-Power Generator

A.2 Presentations

- **2022**
- HTPD 2022 Invited Talk - "Multi-point time-resolved chordal laser interferometry for complementary plasma density measurements"
- SSAP 2022 Talk: "Time resolved electron density PDV measurements from the photoionzed gas cell on Z"
- **2021**

- APS DPP 2021 Talk:"Interrogation of Laboratory Photoionized Plasmas Using Photon Doppler Velocimetry and X-ray Absorption Spectroscopy on the Z-machine"
- Wootton Center Review 2021 Talk: "Interrogation of laboratory produced photoionized plasmas on Z and Zebra"
- **2020**
- Z-net 2020 Poster: "Laboratory Photoionized Plasmas Produced with the 1MA Zebra Pulsed-Power Generator"
- **2019**
- APS DPP 2019 Talk: "Utilizing Gas Jets as a Photoionization Medium for Laboratory Photoionized Plasmas"
- Z Fundamental Science Workshop 2019 Poster: "Laboratory Photoionized Neon Plasmas At Zebra and Z"
- AAS 2019 Invited Talk: "Supersonic Gas Jets as an Interaction Medium for Laboratory Photoionized Plasmas"
- OLUG 2019 Poster: "Two-color Interferometry of Photoionized Supersonic Gas Jets"
- SSAP 2019 Poster: "Two-color Interferometry of Photoionized Supersonic Gas Jets"
- **2018**
- APS DPP 2018 Talk: "Photoionization of Super Sonic Gas Jet Targets Utilizing the 1MA Zebra Generator"
- ZFSW 2018 Poster: "Laser Interferometry Of Photoionized Supersonic Gas Jet Targets"
- AAS LAD 2018 Poster: "Interferometric analysis of laboratory photoionized plasmas utilizing supersonic gas jet targets."

- OLUG 2018 poster: "Laser Interferometry Of Photoionized Plasma Experiments Using Gas Jets"
- **2017**
- APS DPP 2017 Talk: "Study of photoionization of supersonic gas jets at the pulsed power generator"
- Dense Z-pinch 2017 Conference Poster: "Characterization of Supersonic Gas Jets Driven by a Broadband X-Ray Flux"
- AAS LAD Poster 2017 "Laser interferometry of radiation driven gas jets"

Bibliography

[1] J. E. Bailey et al. "A higher-than-predicted measurement of iron opacity at solar interior temperatures". In: *Nature* 517.7532 (Jan. 2014), pp. 56–59. DOI: 10.1038/nature14048.

[2] J. E. Bailey et al. "Neon photoionization experiments driven by Z-pinch radiation". In: *Journal of Quantitative Spectroscopy and Radiative Transfer* 71.2-6 (Jan. 2001), pp. 157–168. DOI: 10.1016/s0022-4073(01)00065-6.

[3] M. A. Bautista and T. R. Kallman. "The XSTAR Atomic Database". In: *The Astrophysical Journal Supplement Series* 134.1 (Jan. 2001), pp. 139–149. DOI: 10.1086/320363.

[4] A. Behjat, G. J. Tallents, and D. Neely. "The characterization of a high-density gas jet". In: *Journal of Physics D: Applied Physics* 30.20 (Jan. 1997), pp. 2872–2879. DOI: 10.1088/0022-3727/30/20/014.

[5] A. Bideau-Mehu et al. "Measurement of refractive indices of neon, argon, krypton and xenon in the 253.7140.4 nm wavelength range. Dispersion relations and estimated oscillator strengths of the resonance lines". In: *Journal of Quantitative Spectroscopy and Radiative Transfer* 25.5 (Jan. 1981), pp. 395–402. DOI: 10.1016/0022-4073(81)90057-1.

[6] Benoît Brichard et al. "Gamma radiation-induced refractive index change in Ge- and N-doped silica". In: *Journal of Applied Physics* 103.5 (Jan. 2008), p. 054905. DOI: 10.1063/1.2885116.

[7] A. S. Chuvatin et al. “Operation of a load current multiplier on a nanosecond mega-ampere pulse forming line generator”. In: *Physical Review Special Topics - Accelerators and Beams* 13.1 (Jan. 2010), na. DOI: 10.1103/physrevstab.13.010401.

[8] Blender Online Community. *Blender - a 3D modelling and rendering package*. Blender Foundation. Stichting Blender Foundation, Amsterdam, 2018. URL: http://www.blender.org.

[9] Robert Cowan. *The theory of atomic structure and spectra*. Berkeley: University of California Press, 1981. ISBN: 9780520038219.

[10] S. C. Jones D. H. Dolan. “THRIVE: a data reduction program for three-phase PDV/PDI and VISAR measurements”. In: *SANDIA Report* (2008).

[11] J. Denavit and D. W. Phillion. “Laser ionization and heating of gas targets for longscalelength instability experiments”. In: *Physics of Plasmas* 1.6 (Jan. 1994), pp. 1971–1984. DOI: 10.1063/1.870653.

[12] D. H. Dolan. “Accuracy and precision in photonic Doppler velocimetry”. In: *Review of Scientific Instruments* 81.5 (Jan. 2010), p. 053905. DOI: 10.1063/1.3429257.

[13] D. H. Dolan. “Extreme measurements with Photonic Doppler Velocimetry (PDV)”. In: *Review of Scientific Instruments* 91.5 (Jan. 2020), p. 051501. DOI: 10.1063/5.0004363.

[14] D. H. Dolan et al. “Plasma and radiation detection via fiber interferometry”. In: *Journal of Applied Physics* 123.3 (Jan. 2018), p. 034502. DOI: 10.1063/1.5008489.

[15] A. C. Fabian et al. “Broad line emission from iron K- and L-shell transitions in the active galaxy 1H 0707-495”. In: *Nature* 459.7246 (Jan. 2009), pp. 540–542. DOI: 10.1038/nature08007.

[16] G. J. Ferland et al. “The 2017 Release of Cloudy”. In: (May 30, 2017). arXiv: 1705.10877v2 [astro-ph.GA].

[17] A. V. Garbaruk et al. “Shock waves in gas-jet target of a laser-produced-plasma short-wave-radiation source with two-pulse plasma excitation”. In: *Technical Physics Letters* 40.11 (Jan. 2014), pp. 980–983. DOI: 10.1134/s1063785014110042.

[18] Ulf Griesmann and John H. Burnett. "Refractivity of nitrogen gas in the vacuum ultraviolet". In: *Optics Letters* 24.23 (Jan. 1999), p. 1699. DOI: 10.1364/ol.24.001699.

[19] M. F. Gu. "The flexible atomic code". In: *Canadian Journal of Physics* 86.5 (Jan. 2008), pp. 675–689. DOI: 10.1139/p07-197.

[20] M. G. Haines et al. "The past, present, and future of Z pinches". In: *Physics of Plasmas* 7.5 (Jan. 2000), pp. 1672–1680. DOI: 10.1063/1.874047.

[21] I. M. Hall et al. "Absorption spectroscopy of a laboratory photoionized plasma experiment at Z". In: *Physics of Plasmas* 21.3 (Jan. 2014), p. 031203. DOI: 10.1063/1.4865226.

[22] William Haynes. *CRC handbook of chemistry and physics : a ready-reference book of chemical and physical data*. Boca Raton, Florida: CRC Press, 2014. ISBN: 9781482208689.

[23] Robert Heinlein. *Stranger in a strange land*. New York: G.P. Putnam's Sons, 1961. ISBN: 9780441790340.

[24] J. L. Henares et al. "Development of gas jet targets for laser-plasma experiments at near-critical density". In: *Review of Scientific Instruments* 90.6 (Jan. 2019), p. 063302. DOI: 10.1063/1.5093613.

[25] M. H. Hess et al. "Design and testing of a magnetically driven implosion peak current diagnostic". In: *Physics of Plasmas* 25.4 (Jan. 2018), p. 042702. DOI: 10.1063/1.5024374.

[26] Jonathan Holburg, Matthias Müller, and Klaus Mann. "Improved gas-jet based extreme ultraviolet, soft X-ray laser plasma source". In: *Optics Express* 29.5 (Jan. 2021), p. 6620. DOI: 10.1364/oe.418075.

[27] Tomonao Hosokai et al. "Observation of strong correlation between quasimonoenergetic electron beam generation by laser wakefield and laser guiding inside a preplasma cavity". In: *Physical Review E* 73.3 (Jan. 2006), na. DOI: 10.1103/physreve.73.036407.

[28] T. M. Hutchinson et al. “Photonic Doppler velocimetry of ohmically exploded aluminum surfaces”. In: *Physics of Plasmas* 27.5 (Jan. 2020), p. 052705. DOI: 10.1063/1.5140477.

[29] V. V. Ivanov et al. “Dynamics of Mass Transport and Magnetic Fields in Low-Wire-Number-ArrayZPinches”. In: *Physical Review Letters* 97.12 (Jan. 2006), na. DOI: 10.1103/physrevlett.97.125001.

[30] V. V. Ivanov et al. “Implosion dynamics and x-ray generation in small-diameter wire-arrayZpinches”. In: *Physical Review E* 79.5 (Jan. 2009). DOI: 10.1103/physreve.79.056404.

[31] V. V. Ivanov et al. “Study of magnetic fields and current in the Z pinch at stagnation”. In: *Physics of Plasmas* 22.9 (Jan. 2015), p. 092710. DOI: 10.1063/1.4931079.

[32] V. V. Ivanov et al. “Study of the Internal Structure and Small-Scale Instabilities in the DenseZPinch”. In: *Physical Review Letters* 107.16 (Jan. 2011), na. DOI: 10.1103/physrevlett.107.165002.

[33] Vladimir V. Ivanov et al. “UV Laser-Probing Diagnostics for the Dense Z Pinch”. In: *IEEE Transactions on Plasma Science* 42.5 (Jan. 2014), pp. 1153–1162. DOI: 10.1109/tps.2014.2314420.

[34] S. H. Barraclough J. A. Pollock. “Note on a Hollow Lighting Conductor Crushed by the Discharge.” In: *Journal and proceedings of the Royal Society of NewSouth Wales* (1905).

[35] George. H. Jacoby, Gary. J. Ferland, and Kirk T. Korista. “The Planetary Nebula A39: An Observational Benchmark for Numerical Modeling of Photoionized Plasmas”. In: *The Astrophysical Journal* 560.1 (Jan. 2001), pp. 272–286. DOI: 10.1086/322489.

[36] Ali Kinkhabwala et al. “XMMNewtonReflection Grating Spectrometer Observations of Discrete Soft XRay Emission Features from NGC 1068”. In: *The Astrophysical Journal* 575.2 (Jan. 2002), pp. 732–746. DOI: 10.1086/341482.

[37] J. P. Knauer et al. “Response model for Kodak Biomax-MS film to x rays”. In: *Review of Scientific Instruments* 77.10 (Jan. 2006), 10F331. DOI: 10.1063/1.2220046.

[38] P. W. Lake et al. “Twin-elliptical-crystal time- and space-resolved soft x-ray spectrometer”. In: *Review of Scientific Instruments* 77.10 (Jan. 2006), 10F315. DOI: 10.1063/1.2227444.

[39] Y. M. Li and R. Fedosejevs. “Density measurements of a high-density pulsed gas jet for laser-plasma interaction studies”. In: *Measurement Science and Technology* 5.10 (Jan. 1994), pp. 1197–1201. DOI: 10.1088/0957-0233/5/10/002.

[40] G. P. Loisel et al. “Benchmark Experiment for Photoionized Plasma Emission from Accretion-Powered X-Ray Sources”. In: *Physical Review Letters* 119.7 (Jan. 2017). DOI: 10.1103/physrevlett.119.075001.

[41] J. J. MacFarlane, I. E. Golovkin, and P.R. Woodruff. “SIMULATION OF THE IONIZATION DYNAMICS OF ALUMINUM IRRADIATED BY INTENSE SHORT-PULSE LASERS”. In: IFSA. 2003.

[42] J.J. MacFarlane, I.E. Golovkin, and P.R. Woodruff. “HELIOS-CR A 1-D radiation-magnetohydrodynamics code with inline atomic kinetics modeling”. In: *Journal of Quantitative Spectroscopy and Radiative Transfer* 99.1-3 (Jan. 2006), pp. 381–397. DOI: 10.1016/j.jqsrt.2005.05.031.

[43] V. Malka, J. Faure, and F. Amiranoff. “Characterization of plasmas produced by lasergas jet interaction”. In: *Physics of Plasmas* 8.7 (Jan. 2001), pp. 3467–3472. DOI: 10.1063/1.1379587.

[44] V. Malka et al. “Characterization of neutral density profile in a wide range of pressure of cylindrical pulsed gas jets”. In: *Review of Scientific Instruments* 71.6 (Jan. 2000), pp. 2329–2333. DOI: 10.1063/1.1150619.

[45] R. C. Mancini et al. “Accretion disk dynamics, photoionized plasmas, and stellar opacities”. In: *Physics of Plasmas* 16.4 (Jan. 2009), p. 041001. DOI: 10.1063/1.3101819.

[46] R. C. Mancini et al. "X-ray heating and electron temperature of laboratory photoionized plasmas". In: *Physical Review E* 101.5 (Jan. 2020), p. 051201. ISSN: 2470-0045. DOI: 10.1103/physreve.101.051201.

[47] F. J. Marshall et al. "Absolute calibration of Kodak Biomax-MS film response to x rays in the 1.5- to 8-keV energy range". In: *Review of Scientific Instruments* 77.10 (Jan. 2006), 10F308. DOI: 10.1063/1.2221698.

[48] D. C. Mayes et al. "Neon Photoionized Plasma Experimentsat Z and Zebra". In: (Nov. 2018).

[49] D. C. Mayes et al. "Observation of ionization trends in a laboratory photoionized plasma experiment at Z". In: *Physical Review E* 104.3 (Jan. 2021), p. 035202. DOI: 10.1103/physreve.104.035202.

[50] Daniel C. Mayes. "Observation and Characterization of Trends in the Ionization of the Warm Absorber Photoionized Plasma Experiment at Z". PhD thesis. University of Nevada Reno, 2020.

[51] J. M. Miller et al. "The Accretion Disk Wind in the Black Hole GRO J1655-40". In: *The Astrophysical Journal* 680.2 (Jan. 2008), pp. 1359–1377. DOI: 10.1086/588521.

[52] N. Murray et al. "Accretion Disk Winds from Active Galactic Nuclei". In: *The Astrophysical Journal* 451 (Jan. 1995), p. 498. DOI: 10.1086/176238.

[53] D. L. Musinski et al. "Gas jet targets for laser plasma interaction studies". In: *Plasma Physics* 24.7 (Jan. 1982), pp. 731–742. DOI: 10.1088/0032-1028/24/7/002.

[54] Donald E. Osterbrock and Gary J. Ferland. *Astrophysics of Gaseous Nebulae and Active Galactic Nuclei*. UNIV SCIENCE BOOKS, Nov. 2005. 480 pp. ISBN: 1891389343. URL: https://www.ebook.de/de/product/4018574/donald_e_osterbrock_gary_j_ferland_astrophysics_of_gaseous_nebulae_and_active_galactic_nuclei.html.

[55] C. Pinto et al. "Thermal stability of winds driven by radiation pressure in super-Eddington accretion discs". In: *Monthly Notices of the Royal Astronomical Society* 491.4 (Jan. 2020), pp. 5702–5716. DOI: 10.1093/mnras/stz3392.

[56] A. Porwitzky et al. "Direct measurements of anode/cathode gap plasma in cylindrically imploding loads on the Z machine". In: *Physics of Plasmas* 25.6 (Jan. 2018), p. 063110. DOI: 10.1063/1.5026225.

[57] Andrew Porwitzky and Justin Brown. "Uncertainties in cylindrical anode current inferences on pulsed power drivers". In: *Physics of Plasmas* 25.6 (Jan. 2018), p. 063102. DOI: 10.1063/1.5026983.

[58] Andrew Porwitzky et al. "Large time-varying inductance load for studying power flow on the Z machine". In: *Physical Review Accelerators and Beams* 22.9 (Jan. 2019), p. 090401. DOI: 10.1103/physrevaccelbeams.22.090401.

[59] N. Richard et al. "Coupled Theoretical and Experimental Studies for the Radiation Hardening of Silica-Based Optical Fibers". In: *IEEE Transactions on Nuclear Science* 61.4 (Jan. 2014), pp. 1819–1825. DOI: 10.1109/tns.2014.2321480.

[60] G. A. Rochau et al. "ZAPP: The Z Astrophysical Plasma Properties collaboration". In: *Physics of Plasmas* 21.5 (Jan. 2014), p. 056308. DOI: 10.1063/1.4875330.

[61] T. W. L. Sanford et al. "Dynamics and characteristics of a 215-eV dynamic-hohlraum x-ray source on Z". In: *Physics of Plasmas* 9.8 (Jan. 2002), pp. 3573–3594. DOI: 10.1063/1.1489676.

[62] Ryan P. Schoenfeld. "Observations from a Long Duration X-Ray Source for Laboratory Astrophysics". English. Copyright - Database copyright ProQuest LLC; ProQuest does not claim copyright in the individual underlying works; Last updated - 2021-05-11. MA thesis. 2020, p. 102. ISBN: 9798557069892. URL: https://unr.idm.oclc.org/login?url=https://www.proquest.com/dissertations-theses/observations-long-duration-x-ray-source/docview/2480344201/se-2?accountid=452.

[63] Kimberly Ann Schultz. *The Experimental Study of Characterized Noble Gas Puffs Irradiated by Ultra-Short Laser Pulses Compared with X-Pinches as an X-Ray Source*. eng. ProQuest Dissertations Publishing, 2017. ISBN: 0355632195.

[64] Howard A. Scott. "Cretina radiative transfer capability for laboratory plasmas". In: *Journal of Quantitative Spectroscopy and Radiative Transfer* 71.2-6 (Jan. 2001), pp. 689–701. DOI: 10.1016/s0022-4073(01)00109-1.

[65] S. Semushin and V. Malka. "High density gas jet nozzle design for laser target production". In: *Review of Scientific Instruments* 72.7 (Jan. 2001), pp. 2961–2965. DOI: 10.1063/1.1380393.

[66] J. A. Simpson. *The Oxford English Dictionary*. Oxford Oxford New York: Clarendon Press Oxford University Press, 1989. ISBN: 9780198611868.

[67] K. J. Swanson et al. "Development and integration of photonic Doppler velocimetry as a diagnostic for radiation driven experiments on the Z-machine". In: *Review of Scientific Instruments* 93.4 (Apr. 2022), p. 043502. DOI: 10.1063/5.0084638.

[68] Vidmantas Tomkus et al. "Laser wakefield accelerated electron beams and betatron radiation from multijet gas targets". In: *Scientific Reports* 10.1 (Jan. 2020), na. DOI: 10.1038/s41598-020-73805-7.

[69] P. W. Wachulak et al. "Extreme ultraviolet tomography of multi-jet gas puff target for high-order harmonic generation". In: *Applied Physics B* 117.1 (Jan. 2014), pp. 253–263. DOI: 10.1007/s00340-014-5829-7.

[70] Przemyslaw W. Wachulak. "Contributed Review: The novel gas puff targets for laser-matter interaction experiments". In: *Review of Scientific Instruments* 87.9 (Jan. 2016), p. 091501. DOI: 10.1063/1.4962012.

[71] O. Willi et al. "Particle and x-ray generation by irradiation of gaseous and solid targets with a 100TW laser pulse". In: *Plasma Physics and Controlled Fusion* 51.12 (Jan. 2009), p. 124049. DOI: 10.1088/0741-3335/51/12/124049.

[72] A Wilson. *ESA Achievements*. 3rd ed. Asian Development Bank, Jan. 2011.

[73] Y. Zhang et al. "Sustained Neutron Production from a Sheared-Flow Stabilized Z Pinch". In: *Physical Review Letters* 122.13 (Jan. 2019), na. DOI: 10.1103/physrevlett.122.135001.